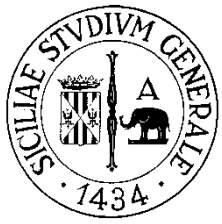

UNIVERSITY OF CATANIA

DEPARTMENT OF CHEMICAL SCIENCES

INTERNATIONAL PhD IN CHEMICAL SCIENCES – XXXI CYCLE

GABRIELE VALORA

Applications of CW and pulsed EPR spectroscopy for the characterization of copper(II) complex stereochemistry and of β-peptide secondary structure

PhD Thesis

Tutor:
Prof. Raffaele Pietro Bonomo
Co-Tutor:
Prof. Marina Bennati

PhD Coordinator:
Prof. Salvatore Sortino

Summary

Electron Paramagnetic Resonance (EPR) is a spectroscopic technique, based on the magnetic resonance principles, that allows the characterization of systems containing unpaired electrons to achieve information on their chemical environment with high resolution. Considering the peculiar class of samples that can be investigated, nowadays, EPR spectroscopy finds applications in several areas of science.

The first part of the thesis offers an overview of the main theoretical key concepts required to understand the set-up and the outcomes of an EPR experiment. Moreover, in chapters 2 and 3,the EPR methodologies adopted in this thesis are presented starting from the first developed continuous-wave (CW) approach up to the more advanced pulsed EPR methods. These latter enable the detection of specific magnetic interactions among the electron spin with other electron or nuclear spins placed in close proximity, allowing to explore the surrounding of the paramagnetic centre at atomic resolution.

Thanks to the modern Site-Directed Spin Labelling (SDSL) approaches, it is possible to introduce spin labels into defined positions of a natural diamagnetic system making it detectable by EPR. This method has further extended the applications towards samples which are naturally EPR silent. Chapter 4 briefly illustrates the main SDSL strategies and the features of the most common nitroxide spin labels adopted in structural biology for the EPR investigation of proteins and nucleic acids.

In the second part of the thesis CW-EPR spectroscopy is employing to characterize the geometries adopted in aqueous solution by some copper(II) complexes with important biological ligands. The study of biochemical processes, in fact, cannot be performed neglecting the inorganic biometals dissolved in biological fluids. These metal ions are involved in the cell biochemistry coordinated by several biomolecules forming metal complexes which are the real “players” with specific biological activities. The functions of these systems are strictly related with the arrangement of the ligands around the metal centre and with the overall geometry of the complex.

In particular, in this part of the thesis, the stereochemistry of binary and ternary Cu(II) complexes with arginine and glutamic acids, which are two abundant amino acids in brain, are investigated by CW-EPR spectroscopy.

Another important class of copper(II) complexes is that one of *cassiopeinas*, which are emerging as important antitumor agents. Among these compounds, in the last years, many efforts were made to characterize ternary copper(II) complexes with 1,10-phenantroline and different amino acids. Also in this case CW-EPR spectroscopy is employed to investigate the peculiar geometries of these systems in aqueous solution. The experimental results presented in this part of the thesis enable to develop a more detailed picture of these copper(II) species in solution in order to better clarify their structure-function relationships for further biochemical considerations about their role. Additionally, voltammetric measurements are performed on the same systems to support the spectroscopic data.

In the third part of the thesis, the results of a project developed in the Electron Spin Resonance research group at the Max Planck Institute for Biophysical Chemistry (Göttingen – Germany), under the supervision of Professor MARINA BENNATI, is presented.

It is well-known that the structural characterization of membrane proteins in their natural environment is a challenging task. EPR spectroscopy in combination with SDSL approaches is emerging as a powerful biophysical tool to reveal biomolecular structural information at atomic resolution. In particular, Pulsed Electron Double Resonance (PELDOR) spectroscopy, called also Double Electron Electron Resonance (DEER), is a pulsed EPR method which enables to detect distances between two paramagnetic centres in a biological system in order to characterize its structure. Measuring the dipolar coupling between two unpaired electrons, PELDOR allows to probe their intramolecular distances with high resolution and reliability.

In this project, CW-EPR and PELDOR/DEER spectroscopy are employed for the structural characterization of a transmembrane peptide in solution and in a lipid environment. An additional pulsed EPR method, called 3-pulse ESEEM, enables to have indications about the proper incorporation of the spin labelled peptides into a lipid bilayer. The samples are prepared introducing two semi-rigid TOPP nitroxide spin labels into the peptide's backbone in order to make it detectable by EPR. The experimental results of this part of the thesis demonstrate the great potential of EPR spectroscopy in structural biology to characterize biomolecular structures and encourage the employment of TOPP spin label as useful tool for the EPR investigation of peptides' foldamers in solution and in lipid bilayer.

TABLE OF CONTENTS

I. PART

INTRODUCTION TO EPR SPECTROSCOPY

1. EPR spectroscopy

Electron Paramagnetic Resonance (EPR) is a spectroscopic technique that allows to study systems which have an angular spin momentum $\vec{S} \neq 0$ due to the presence of one or more unpaired electrons.

An EPR experiment is based on the interaction between an electromagnetic radiation, normally in the range of microwave (GHz), and the paramagnetic sample which is placed into an external magnetic field $\vec{B}_0$. In this condition, the two spin states of the unpaired electron do not have the same energy and the microwave absorption occurs if the frequency of the incident radiation covers the energy gap between them, according to the resonance condition $\Delta E = h\nu$.

The first EPR signal was observed during the Second World War in 1944 by the Russian physicist ZAVOISKY who studied aqueous and non-aqueous solution of manganese salts irradiated by different electromagnetic waves in the presence of a variable magnetic field.[1] In less than one century an impressive progress was made so that EPR spectroscopy finds nowadays wide range of applications in many branches of science.

Several EPR methods and EPR spectrometers have been developed in order to investigate a large number of samples (liquid solutions, solids, single crystals, powders…) in a broad range of temperatures (from few Kelvin degrees up to room temperature) at different magnetic fields and frequencies according to the magnetic properties that must be detected.

The systems that can be characterized by EPR are: complexes containing paramagnetic metal ions, organic radicals, point defects in solids, electron transfer mechanisms, photoinduced triplet states of a molecule and so on. In the last decades, EPR spectroscopy also extended to the investigation of diamagnetic systems if they are properly engineered with spin labels through the modern site-directed spin labeling (SDSL) technique introduced by ALTENBACH and co-workers in 1990.[2] This methodology will be presented in chapter 4 and an example of EPR characterization of biomolecules modified with spin labels will be given in part III of this thesis.

In the next paragraphs, the theoretical key concepts of the EPR phenomenon are presented. Further details can be found in the books of WERTZ and BRUSTOLON.[3,4]

1.1 Theoretical background and the Spin Hamiltonian

The electron is a charged quantum particle which has an intrinsic angular momentum $\vec{S}$, called spin, due to the rotational motion around its own axis. The vector $\vec{S}$ has three components along the *x*, *y* and *z* axis in the Cartesian frame: S_x, S_y and S_z; the magnitude of the angular spin momentum $|\vec{S}|$ is quantized according to equation (1).

$$|\vec{S}| = \sqrt{S(S+1)} \tag{1}$$

$S = \frac{1}{2}$ is the quantic number of the angular spin momentum.

Moving from a classical to a quantum mechanics description, the spin angular momentum $\vec{S}$ is described by the operators $\hat{S}_x$, $\hat{S}_y$ and $\hat{S}_z$. The three operators do not commute to each other but each of them commute with the $|\vec{S}|^2$. Thus, for the Heisenberg uncertainty principle, it is possible to know exactly and at the same time the magnitude $|\vec{S}|$ and only one projection of the vector $\vec{S}$, which is conventionally the component S_z, written in equation (2).

$$S_z = m_s \hbar \tag{2}$$

$m_s = \pm\frac{1}{2}$ is the quantic number of the *z*-component of the angular spin momentum. Consequently the spin angular momentum $\vec{S}$ can assume only two orientations along *z* axis at the same energy: $\alpha = +\frac{1}{2}$ and $\beta = -\frac{1}{2}$. The components in the perpendicular plane to the *z* axis are not defined.

Like any other charged moving particles, a magnetic moment $\vec{\mu}_e$ is associated with the electron spin angular momentum $\vec{S}$ according to equation (3):

$$\vec{\mu}_e = \gamma_e \vec{S} \tag{3}$$

$\gamma_e$is the electron gyromagnetic ratio, related with the charge ($-e$) and the mass (m_e) of the electron. These two parameters, together with the reduced Planck constant (ħ), are included in the Bohr magneton ($\beta_e = 9.27 \times 10^{-24}\, JT^{-1}$), as shown in equation (4).

$$\gamma_e = g_e \frac{-e\hbar}{2m_e} = -g_e \beta_e \tag{4}$$

g_e is the Landé factor, or simply the *g*-factor. It is a proportional constant that for free electrons is equal to 2.0023. Considering that the electron is negatively charged, $\vec{\mu}_e$ and $\vec{S}$ are two collinear vectors with opposite directions. Taking into account the equations (1) and (2) it is easy to derive the relationships (5) and (6).

$$|\vec{\mu}_e| = -g_e\beta_e\sqrt{S(S+1)} \tag{5}$$

$$\mu_z = \gamma_e S_z = -g_e\beta_e m_s \tag{6}$$

Similarly to $\vec{S}$, the magnetic moment $\vec{\mu}_e$ can assume only two possible orientations α and β at the same energy (degenerate) along *z* axis (figure 1.1). If the electron is placed into a static magnetic field $\vec{B}_0$, whose direction conventionally defines the *z* axis of the laboratory frame, the magnetic interaction between $\vec{B}_0$ and $\vec{\mu}_e$ removes the degeneration of the two spin states and the magnetic dipoles will be oriented parallel (high energy level) or antiparallel (low energy level) to $\vec{B}_0$. This effect is called *electron Zeeman interaction*, illustrated in figure 1.1, and the energy of each spin-state depends on the intensity of $\vec{B}_0$ according to equation (7).

$$E = -\mu_z \cdot \vec{B}_0 = g_e\beta_e m_s B_0 \tag{7}$$

It is possible to induce a transition from β-state to α-state applying an electromagnetic radiation with a proper frequency that satisfies the resonance condition: $\Delta E = E_\alpha - E_\beta = h\nu = g_e\beta_e B_0$ (figure 1.1). This condition is reached employing a microwave radiation (GHz frequency).

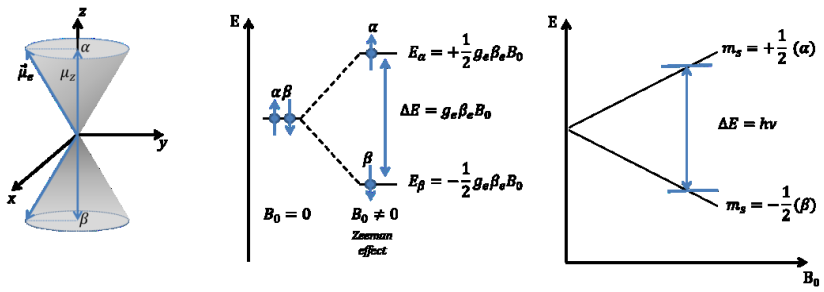

Figure.1.1. On the left, the orientations of $\vec{\mu}_e$ along the z-axis is shown. When $\vec{B}_0$ is applied the magnetic interaction with $\vec{\mu}_e$ determines the Zeeman effect with a splitting of the two spin states (centre). Irradiating the sample with a microwave an electron spin transition can be induced (right) if the resonance condition is satisfied.

This quantum mechanics description is valid for an isolated electron. In the case of atoms or molecules, the electron performs an additional rotational motion around the nucleus, described by an orbital angular momentum $\vec{l}$ that generates the magnetic moment $\vec{\mu}_l$. The quantum mechanics treatment of these two momenta is similar to that one of $\vec{S}$ and $\vec{\mu}_e$ illustrated above. The angular magnetic momentum $\vec{\mu}_l$ gives an additional contribution to the electron magnetic moment $\vec{\mu}_e$; furthermore, the spin and the orbital motions are not independent but the spin and orbital momenta are coupled to each other through a spin-orbit coupling. This effect introduces an orbital contribution in the electron spin term resulting in a deviation of the *g*-factor from the free electron value, as shown in equation (8).

$$g = g_e + \Delta g \tag{8}$$

The entity of this deviation Δg depends on the magnitude of the spin-orbit coupling which is a function of the symmetry of the system. Molecules have low symmetry and the angular momentum $\vec{l}$ is quenched so the magnetism of the electron depends essentially on the electron spin $\vec{S}$. This explains why several organic radicals show *g*-factor values close to 2.0023. On the contrary, paramagnetic metal ions present a much more bigger spin-orbit coupling constant that implies larger deviations on the *g*-factor.[5] This effect will be described in more details in chapter 6 where the main features of CW-EPR spectra of paramagnetic Cu(II) complexes will be illustrated.

The spin-orbit coupling is anisotropic because it depends on the orbitals that are involved in this interaction. In the case of a complex containing a transition metal ion, the ligand field removes the degeneration of *d* orbitals selectively according to the arrangements of the ligands around the metal centre in the molecular frame. As a result, the *g* values are anisotropic and depict the “fingerprint” of the paramagnetic metal ion under investigation, giving a lot of information on its oxidation state and its coordination environment.

The *g*-factor is described by a tensor, a 3x3 matrix reported in a Cartesian frame (*X, Y, Z*) in equation (9).

$$g = \begin{bmatrix} g_{XX} & g_{XY} & g_{XZ} \\ g_{YX} & g_{YY} & g_{YZ} \\ g_{ZX} & g_{ZY} & g_{ZZ} \end{bmatrix} \tag{9}$$

Choosing specific rotation angles it is possible to find a set of Cartesian axis *x*, *y*, *z* so that this matrix is diagonalized meaning that all terms out of the diagonal are equal to zero, equation (10).

$$g = \begin{bmatrix} g_{xx} & 0 & 0 \\ 0 & g_{yy} & 0 \\ 0 & 0 & g_{zz} \end{bmatrix} \tag{10}$$

According to the symmetry of the system, we can distinguish three cases:

- *Cubic symmetry* if the system presents the same *g* value along the three axis $g = g_{xx} = g_{yy} = g_{zz}$.
- *Axial symmetry* where only two principal *g* values can be identified: $g_{xx} = g_{yy} = g_{\perp}$ if the magnetic field is perpendicular to the axis of symmetry; $g_{zz} = g_{\parallel}$ if $\vec{B}_0$ is parallel to it. The *g* value is achieved by equation (11).

$$g = \frac{1}{3}(g_{\parallel} + 2g_{\perp}) \tag{11}$$

- *Orthorhombic symmetry* if the system presents $g_{xx} \neq g_{yy} \neq g_{zz}$ the *g* value can be extracted by the equation (12):

$$g = \frac{1}{3}(g_{xx} + g_{yy} + g_{zz}) \tag{12}$$

The *g*-anisotropy can be measured experimentally by rotating a single crystal and recording an EPR spectrum for each orientation.

In the case of a powder sample or a sample in frozen solution, we have an ensemble of microcrystals randomly oriented in the space, yielding normally to a superimposition of several EPR lines, each one corresponding to the individual orientation.

In liquid solution the fast Brownian motions determine a continuous spin re-orientation that averages out the *g* anisotropy.

In solid-state the EPR spectrum becomes more complicated in comparison with the liquid-phase and the calculations of the *g* components must take into account the symmetry of the solid and the angle ϑ and φ that the magnetic field $\vec{B}_0$ forms with respect to the *g*-tensor principal axis in a polar coordinate system.

The complete Hamiltonian that describes all magnetic interactions in a paramagnetic molecule placed into a static magnetic field $\vec{B}_0$ is written in equation (13). Each contribution is discussed in the next sections.

$$\hat{H}_0 = \hat{H}_{EZ} + \hat{H}_{NZ} + \hat{H}_{HF} + \hat{H}_{NQ} + \hat{H}_{EX} + \hat{H}_{DD} \quad (13)$$

1.1.1 Electron and Nuclear Zeeman interactions

The first term of the Hamiltonian written in equation (13) represents the electron Zeeman interaction ($\hat{H}_{EZ} = \vec{B}_0 g \hat{S}$) already discussed in the previous section. The eigenvalues of $\hat{H}_{EZ}$ correspond to the energy levels of the spin states.

If the molecule contains nuclei with a nuclear moment $\vec{I} \neq 0$, in analogy with the electron, a nuclear magnetic moment is generated, equation (14).

$$\vec{\mu}_N = g_N \beta_N \vec{I} \quad (14)$$

$\beta_N = \frac{e\hbar}{2m_p} = 5.05 \times 10^{-27}$ is the nuclear magneton which includes the charge (e) and the mass (m_p) of the nucleus. Taking into account that the nucleus is positive charged, the vectors $\vec{\mu}_N$ and $\vec{I}$ are collinear and oriented in the same direction. The interaction between the nuclear magnetic moment $\vec{\mu}_N$ and the magnetic field $\vec{B}_0$ yields a *nuclear Zeeman effect* described by the Hamiltonian $\hat{H}_{NZ} = \vec{B}_0 g_N \hat{I}$. The eigenvalues of $\hat{H}_{NZ}$ correspond to the energy levels of nuclear states.

Considering that the mass of electron is almost three orders of magnitudes smaller than that one of a nucleus, β_e is much bigger than β_N.

1.1.2 Hyperfine and superhyperfine interactions

If the paramagnetic system contains nuclei with a nuclear moment $\vec{I} \neq 0$ the electron spin experiences an additional magnetic field coming from the interaction, called *hyperfine interaction*, with the nuclear magnetic moment $\vec{\mu}_N$. Although the external magnetic field is much bigger, the proximity electron-nuclei favours this kind of interaction whose effect is a splitting of the EPR line in several components according to the value of the quantic

number *I* of the nuclear magnetic moment. For the nucleus, *2I+1* orientations are possible, thus, a splitting of *2I+1* EPR lines are visible. If there are more than one equivalent nuclei $I = \sum I_i$; the intensity and multiplicity of the EPR signal are defined by the Tartaglia's triangle. The distance between two adjacent EPR lines is defined as *hyperfine coupling constant* (*A*).

In part III of this thesis, the EPR characterization of biomolecules modified with nitroxide spin labels is discussed. Nitroxides are organic radicals widely used for the EPR characterization of biological systems with a general form $R^1 - NO^{\cdot} - R^2$. ^{14}N is the most abundant isotope of N and it is a magnetically active nucleus with a magnetic nuclear quantum number *I=1*. The hyperfine interaction between the unpaired electron (*S=½*) of nitroxide radical with the nuclear magnetic moment of ^{14}N determines a split of the EPR line in three components because three EPR transitions are possible for each different nuclear spin-state according to the selection rules: $\Delta M_S = \pm 1$ and $\Delta M_I = 0$. (figure 1.2).

A quantum mechanics description of the hyperfine interaction is given in the Hamiltonian of equation (15).

$$\hat{H}_{HF} = \hat{H}_{Fermi} + \hat{H}_{dipole} = \hat{S}A\hat{I} = a_{iso}\hat{I}\hat{S} + \hat{S}T\hat{I} \qquad (15)$$

A is the *hyperfine coupling constant* and it is a tensor, like the *g*-factor, which is made up of two components: $A = a_{iso} + T$.

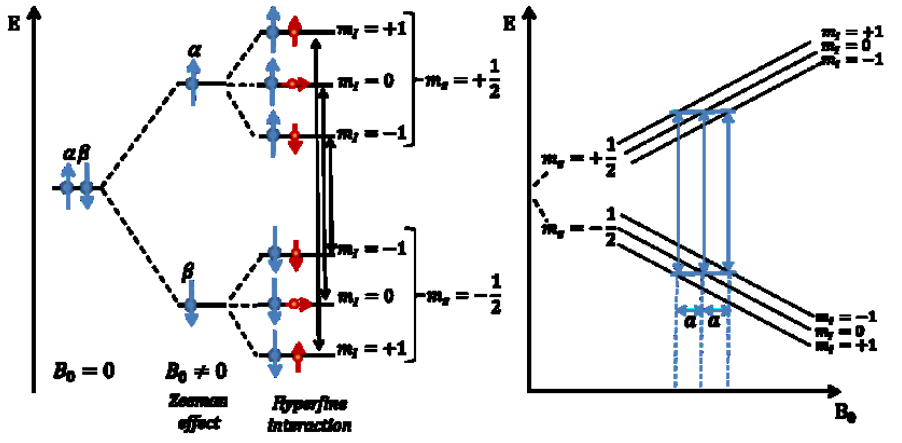

Figure 1.2. Hyperfine interaction between the electron spin (*S=½*) and the nuclear spin of ^{14}N (*I=1*): energy levels and permitted EPR transitions; *a* is the hyperfine coupling constant.

a_{iso} is an isotropic contribution due to a *Fermi contact interaction*, related to the probability $|\Psi(0)|^2$ to find the electron on the nucleus, equation (16). Quantum mechanics does not exclude that the spin density at the nucleus is equal to zero.

$$a_{iso} = \frac{8}{3}\pi g \beta_e g_N \beta_N |\Psi(0)|^2 \tag{16}$$

The second hyperfine term is anisotropic and it is described by the tensor T. This contribution occurs when the electron and the magnetic moments ($\vec{\mu}_e$ and $\vec{\mu}_N$) are dipolar coupled through the space. The energy of this interaction is classically described by equation (17), where μ_0 is the vacuum permeability.

$$E = \frac{\mu_0}{4\pi}\left[\frac{\vec{\mu}_e \cdot \vec{\mu}_N}{|\vec{r}|^3} - \frac{3(\vec{\mu}_e \cdot \vec{r})(\vec{\mu}_N \cdot \vec{r})}{|\vec{r}|^5}\right] \tag{17}$$

The Hamiltonian $\hat{H}_{dipole}$ is explicitly written in equation (18) and it is a function of the distance $|\vec{r}|$ between the two interacting magnetic dipoles. The eigenvalues of this Hamiltonian give the dipolar interaction energy.

$$\hat{H}_{dipole} = \hat{S}T\hat{I} = -g\beta_e g_N \beta_N \left[\frac{\hat{S} \cdot \hat{I}}{|\vec{r}|^3} - \frac{3(\hat{S} \cdot r)(\hat{I} \cdot r)}{|\vec{r}|^5}\right] \tag{18}$$

$\hat{H}_{Fermi} \gg \hat{H}_{dipole}$ therefore if the system presents a spherical symmetry or if the EPR experiments are performed in liquid solution the anisotropic contribution is average out and just the isotropic term contributes to the EPR spectrum.

However, only *s* orbitals have a non-zero probability to have the electron at the position of the nucleus: in the case of an hydrogen atom (^{1}H), which contains only one electron in a *s* orbital, a_{iso} is equal to 508 G. All other orbitals (*p*, *d* or *f*) have nodes at the nucleus; nevertheless, EPR spectra in liquid solution of metal complexes or of organic radicals still show an isotropic hyperfine interaction. This isotropic contribution comes out through another mechanism called *spin polarization*: the spin-state of the unpaired electron has an influence on the spin-state of close by pair electrons involved in bonding formation through a quantum mechanics Coulomb repulsion. In particular, if the unpaired electron is in a “spin-up” state, the electron of the close by pair bonding that is nearer to it has a

larger probability to be in a “spin-down” state than the farther one which will assume, for the Pauli’s principle, a “spin-up” state.

EPR spectra of metal complexes containing transition metal ions can be further complicated by the presence of ligands containing magnetically active coordinating atoms. In this case, an additional magnetic interaction, called *superhyperfine interaction*, occurs and each EPR line is further split in *2I+1* lines where *I* is the nuclear magnetic quantic number of the donating atom. The superhyperfine coupling constant A^L is much smaller than the hyperfine coupling constant *A* and it is made up , as well, of isotropic and anisotropic components according to the molecular orbitals of the complex.

The features of these EPR spectra and the magnetic parameters give a lot of information about the coordination environment and the geometry of paramagnetic metal complexes. Part II of this thesis will show several examples of Cu(II) complexes ($^{Cu}I=3/2$) that contain an unpaired electron ($S=½$) due to the electronic configuration d^9 of Cu(II) ions with N-donor ($^{N}I=1$) ligands.

1.1.3 Nuclear Quadrupole interaction and Exchange interaction

The nuclear quadrupole interaction is typical of nuclei with $I>½$ whose quadrupole moment interacts strongly with the electric field of the surrounding electrons. The Hamiltonian that describes this interaction is written in equation (19) where Q is the quadrupole tensor.

$$\widehat{H}_{NQ} = \hat{I}Q\hat{I} \tag{19}$$

In the case of biradicals or multispin systems, a slight overlap between the wavefunctions of two or more unpaired electrons can occur if they are close by through the space. This interaction, called *exchange interaction*, is a quantum mechanics phenomenon resulting from the interchanging of spin-states of two electrons due to the combination of their wavefunctions. This effect is described by the Hamiltonian of equation (20).

$$\widehat{H}_{EX} = \hat{S}_A J \hat{S}_B \tag{20}$$

$\hat{S}_A$ and $\hat{S}_B$ are the operators of the spin angular momenta of the two electrons and J is a tensor that describes the exchange interaction.

For interspin distances longer than 1 nm, the exchange term can be neglected in the general Hamiltonian of equation (13).

The effects described in this section will not be further discussed because they are not a topic of this thesis.

1.1.4 Dipolar electron-electron interaction

If the paramagnetic system contains two unpaired electrons A and B separated by a distance $\vec{r}_{AB}$, similarly to the hyperfine interaction, the associated magnetic moments $\vec{\mu}_A$ and $\vec{\mu}_B$ can be dipolar coupled through the space. The energy of this interaction is given in equation (21). It is analogous with that one already observed in equation (17) with the exception that the magnetic moment of the second coupled electron takes the place of the nuclear magnetic moment.

$$E = \frac{\mu_0}{4\pi}\left[\frac{\vec{\mu}_A \cdot \vec{\mu}_B}{|\vec{r}|^3} - \frac{3(\vec{\mu}_A \cdot \vec{r})(\vec{\mu}_B \cdot \vec{r})}{|\vec{r}|^5}\right] \tag{21}$$

The corresponding Hamiltonian, similar to that one of equation (18), is given in equation (22), where D is the *dipolar coupling constant* written extensively in equation (23).

$$\widehat{H}_{DD} = \widehat{H}_{DD} = \hat{S}_A D \hat{S}_B = -g_A g_B \beta_e^2 \left[\frac{\hat{S}_A \cdot \hat{S}_B}{|\vec{r}|^3} - \frac{3(\hat{S}_A \cdot r)(\hat{S}_B \cdot r)}{|\vec{r}|^5}\right] \tag{22}$$

$$D = \frac{\mu_0 \beta_e^2 g_A g_B}{4\pi\hbar} = 2\pi \cdot 52.18 \left[\frac{MHz}{nm^3}\right] \tag{23}$$

Normally, the electron-electron interactions are a small contribution compared with the electron Zeeman effects to the general Hamiltonian of equation (13). In these conditions, the dipolar coupling through the space between two unpaired electrons can be expressed by the angular dipolar frequency ω_{dd} shown in equation (24).

$$\omega_{dd} = \frac{D}{|\vec{r}_{AB}|^3}(1 - 3cos^2\vartheta) \left[\frac{rad}{s}\right] \tag{24}$$

The frequency expressed in MHz is given in equation (25).

$$\nu_{dd} = \frac{\omega_{dd}}{2\pi} = \frac{52.18}{|\vec{r}_{AB}|^3}(1 - 3cos^2\vartheta)\ [MHz] \qquad (25)$$

According to equations (24) and (25), the dipolar frequency is a function of the distance $|\vec{r}_{AB}|$ between the two electrons A and B and of the angle ϑ that the vector $\vec{r}_{AB}$ forms with the magnetic field $\vec{B}_0$, as shown in figure 1.3. In liquid solution the paramagnetic sample can move freely and, so, ω_{dd} is averaged to zero. If the sample is frozen, it shows a random distribution of all different orientations, as mentioned previously, giving the characteristic *Pake pattern*, shown in figure 1.3. This graph is made up of two subspectra resulting from the two spin states α and β of the coupled electrons.

For $\vartheta = 0°$ $(\vec{r}_{AB}||\vec{B}_0)$ $\qquad \omega_{dd} = -2\frac{D}{r_{AB}^3}$

In this case, there is only one possible orientation of $\vec{r}_{AB}$ parallel to $\vec{B}_0$.

For $\vartheta = 90°$ $(\vec{r}_{AB}\perp\vec{B}_0)$ $\qquad \omega_{dd} = \frac{D}{r_{AB}^3}$

Many orientations of $\vec{r}_{AB}$ on the perpendicular plane to $\vec{B}_0$ are possible. This explains the different intensities in the Pake doublet illustrated in figure 1.3.[6] At $\vartheta = 54{,}7°$, called "magic angle", the dipolar coupling vanishes.

The separation between the two maxima of the Pake pattern represents the value of the dipolar frequency in the case of $\vec{r}_{AB}\perp\vec{B}_0$ and this splitting is used to measure experimentally ω_{dd}.

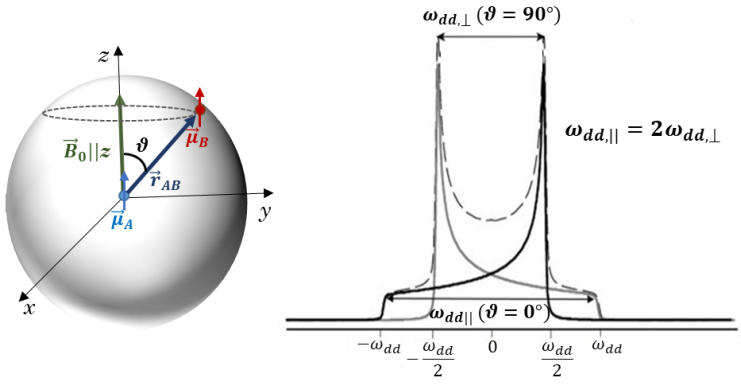

Figure 1.3. On the left, the orientations of vector $\vec{r}_{AB}$ are illustrated. On the right, the Pake doublet shows how the values of ω_{dd} change with ϑ in a powder sample.

Considering the equations (24) and (25), it is easy to extract information on the inter-spin distance, equation (26).

$$r = \sqrt[3]{\frac{52.18}{\nu_{dd}}} = \sqrt[3]{\frac{2\pi \cdot 52.18}{\omega_{dd}}} \quad [nm] \tag{26}$$

Specific pulse sequences, that will be illustrated in chapter §3, were developed to probe the distances between two unpaired electrons to get structural information at atomic resolutions on biomolecular systems properly modified with spin labels. Part III of this thesis gives an example of this field of application of EPR spectroscopy.

2. Continuous-wave and pulse EPR spectroscopy

The first EPR spectrometers that were developed enabled to irradiate the paramagnetic sample with a constant microwave at a fixed frequency and to carry out a field sweep up to the resonance condition is matched. This first EPR approach is called *continuous-wave* (CW) *mode*.

In the modern EPR spectrometers the spin system is excited by a series of microwave pulses at high power keeping constant the magnetic field strength; then, the induced signal is measured when the pulses are switched off. This new methodology followed the progress of pulsed NMR spectroscopy and the pioneers in this field were MIMS[7] of Bell laboratories, BROWN of McDonnell-Douglas Research Laboratories and TSVETKOV[8] of Novosibirsk University. These scientists have developed the first technological and theoretical principles of *pulse EPR spectroscopy* from the beginning of 1970th.

Many EPR applications still adopt CW-EPR approach because it presents an higher sensitivity compared with the more advanced pulse methods;[9] moreover, pulse EPR requires additional sophisticated components to perform the experiment. On the other hand, pulse EPR spectroscopy allows to select the magnetic interaction of interest applying specific pulse sequences that generates a signal containing only the desired information. Therefore, till now, these two techniques are two complementary methodologies to achieve a significant picture of the spin system under investigation.

In this thesis, both CW and pulsed EPR methods are employed for the characterization of Cu(II) complexes with different ligands of biological relevance (part II) and for the structural investigation of transmembrane peptides in solution and in lipid bilayer (part III).

In the last decades, both CW and pulse EPR experiments were carried out in EPR spectrometers at high fields and high frequencies: each EPR experimental setup is described by a letter as shown in figure 2.1. Moreover, double frequencies experiments were designed in order to deeply investigate various magnetic interactions.[10]

According to equations (7) and (15) the resolution of *g*-tensor is field-dependent while the resolution of *A*-tensor is field independent.

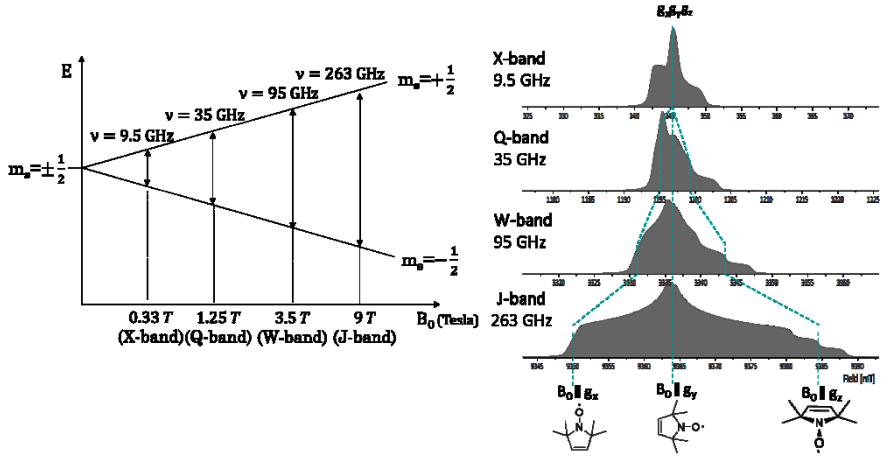

Figure 2.1. On the left, the field strengths and microwave frequencies of the 4 most employed EPR bands (X, Q, W and J) are shown. On the right, the ESE signals of a nitroxide radical are illustrated to highlight the enlargement of *g*-tensor resolution at different fields and frequencies.

As discussed in the paragraph §1.1, transition metal ions have a strong spin-orbit coupling, so the components of *g*-tensor are already well resolved at low fields and low frequencies. Thus, EPR experiments at X-band and Q-band frequencies are generally performed for the characterization of complexes containing paramagnetic *d*-metal centres.[11,12]

In the case of organic radicals, the low symmetry of the system implies that the features of *g*-tensor can be resolved only moving to higher fields and higher frequencies.[13] Figure 2.1 illustrates the swept-field electron spin echo (ESE) signal, that will be described in the paragraph §3.2, of a nitroxide radical: at X-band frequencies the three components of *g*-tensor are indistinguishable and the shape of the EPR signal is dominated only by hyperfine anisotropy. *A*-tensor and *g*-tensor are collinear in nitroxide radicals and their anisotropies show a comparable amplitude at Q-band frequencies; furthermore, at W-band or J-band the *g*-tensor is totally resolved and it is possible to excite different portions of the EPR spectrum which correspond to different orientations of the *g*-tensor with respect to $\vec{B}_0$.[14] According to the information that we want to achieve the most suitable EPR spectrometer is employed.

In the next paragraph the main instrumental components of a CW-EPR spectrometer and the most important experimental parameters are briefly illustrated. Then, the additional components required to generate pulses in a pulsed EPR spectrometer are described.

2.1 EPR spectrometer

Different EPR spectrometers are commercially available and the development of additional equipment to improve the potential of these machines is still proceeding in several laboratories.

A simplified scheme of a CW-EPR spectrometer is shown in figure 2.2. The paramagnetic sample is placed between two electromagnets in a resonator where takes place the interaction with the microwave. The electromagnets allow to vary the static magnetic field $\vec{B}_0$ by run a current through some coils. This creates a large amount of heat and so a continuous flow of water around the magnet prevents the overheating.

The klystron or the most modern Gunn diode are monochromatic sources that generate a continuous microwave. This radiation is sent to the sample through a wave-guide whose sizes are strictly related to the wavelength λ in order to amplify the incident electromagnetic wave. The power of the microwave (of the order of mW) can be varied by an attenuator placed before the resonator to control precisely the amount of radiation that the sample will experience.

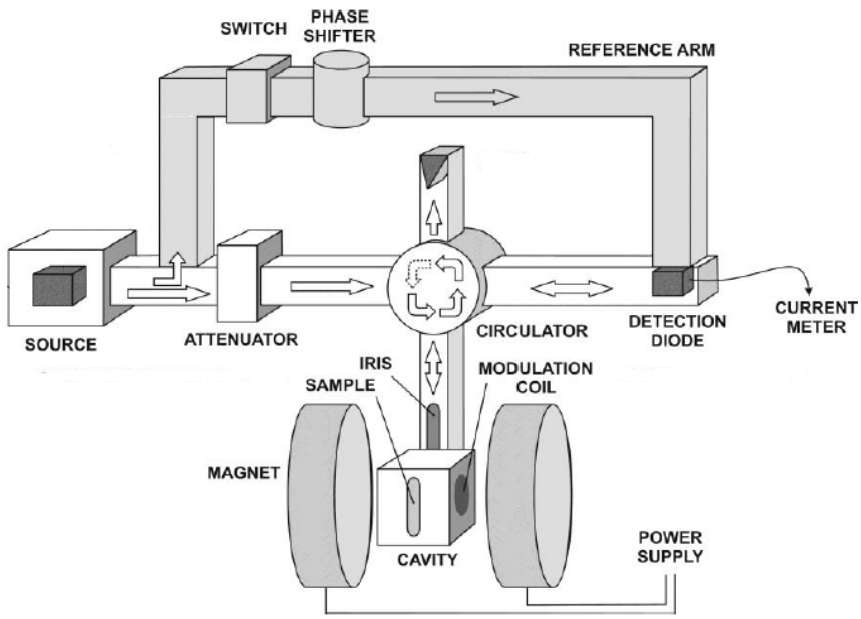

Figure 2.2. Scheme of a CW-EPR spectrometer adapted from[15].

The sample is located in the center of the resonant cavity with a rectangular or cylindrical shape ensuring the maximum absorption of magnetic component from the microwave and minimum absorption of its electric component whose energy is dissipated on the walls of the cavity producing heat.

Resonant cavities are characterized by a quality factor (*Q*), which indicates how efficiently they are able to store microwave energy. As shown in figure 2.3, the quality factor is a function of ν_{res}, the resonant frequency of the cavity, and $\Delta\nu$, the half width at half height of the resonance peak. The higher is the *Q* factor value, the higher will be the sensitivity of the measurement.

An EPR spectrometer has generally a reflection set-up: once the radiation interacts with the sample, it is reflected back to the detector that compares the power of incident and reflected radiations. A circulator, depicted in figure 2.2, drives selectively the incident microwave only from the klystron to the resonator and the reflected microwave only from the resonator to the detector avoiding that it comes back to the microwave source damaging it. When we are off resonance the microwave is completely reflected by the cavity; on the contrary, when we are in resonance a decrease in the amount of microwave radiation that is being reflected out of the resonator is recorded yielding to the EPR signal.

The detector is a diode which transforms the microwave power in an electric current proportional to the power of radiation. To achieve an accurate quantitative measurement of the absorbed microwave energy, the diode must work in a linear range.

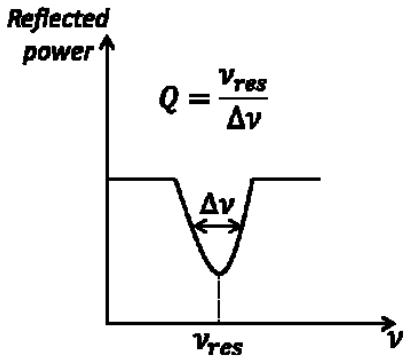

Figure 2.3. The quality factor.

The reference arm supplies the detector with an extra microwave power, coming directly from the source, to ensure a steady level of current. Additionally, it bias eventually a phase shifter to make sure that the two signals arriving to the detector from the reference arm and from the resonator are in phase when they combine.

The microwave enters into the cavity through a variable opening called iris, whose size regulates and couples the amount of incident radiation which goes inside the cavity with that one reflected back from the cavity. The resonator is critically coupled when all the power that enters into it is not reflected out.

In order to increase the signal to noise ratio, CW-EPR spectrometers make use of phase-sensitive detection achieved by a field modulator, which is applied through specific modulation coils. The field modulator creates a small oscillating magnetic field around the sample in addition to $\vec{B}_0$. This oscillating magnetic field has an amplitude which is smaller than that one of the resonance peak (normally around 100 KHz) and defines the range of electromagnetic energy that reaches the detector, increasing the resolution of the EPR measurement. Considering that the field experienced by the spin system is modulated at 100 KHz, the output which gets to the resonator will be oscillating as well and it is sensitive to the slope of the absorption peak. A lock-in amplifier, connected to the detector, will amplify only the signals modulated at this frequency, the others (noise and electrical interferences) will be suppressed. As a consequence of the modulation process, CW-EPR spectra show up as a derivative line shape relative to energy absorption peak (figure 2.4). This field modulation procedure is not performed in pulse EPR methods.

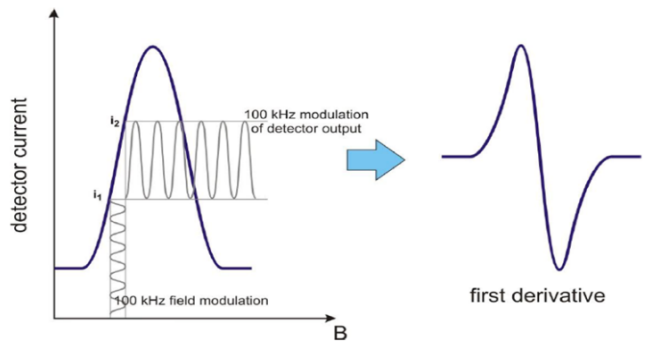

Figure 2.4. First derivative EPR signal. Figure adapted from[16].

The amplitude of field modulation is an important parameter that must be fixed accurately: if it is larger than the linewidth of the EPR line, the signal broadens and becomes distorted.

The time constant is another parameter which is used to filter out more of the noise by slowing down the time response of the spectrometer.

2.1.1 Pulse-forming unit (PFU)

As previously introduced, pulsed EPR spectroscopy requires the generation of short (timescale of ns) and high-power pulses which are created through some additional components. Basically, once the continuous microwave is generated from the source, it is driven to a pulse-forming unit (PFU) that makes the desired pulse sequence from segments of the continuous radiation (figure 2.5). This sequence is sent to an amplifier followed by an additional attenuator that allows to regulate the power of pulses which are directed to the sample. This attenuator is connected to the circulator so that the pulses can be driven inside the resonator. Each pulse excites the whole spin system that, in this way, experiences an additional magnetic field $\vec{B}_1$ for a small time interval t_p (pulse length). In order to preserve the detector from the high power of reflected pulses, a diode switcher blocks the pulses until the so called *ringing*, which appear after pulse excitation, has decayed (defense pulse).

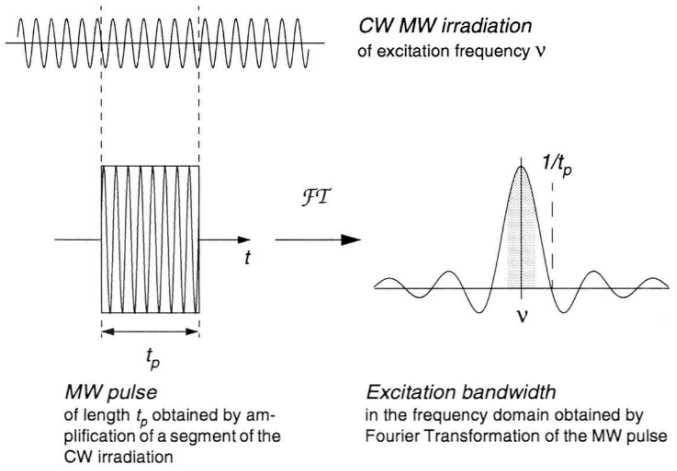

Figure 2.5. Generation of pulses with a rectangular pulse profile from a continuous microwave radiation. Figure adapted from[17].

This set-up allows to generate rectangular pulses whose excitation profile corresponds to a *sinc* function (*sin(x)/x*) when the pulses are Fourier transformed (figure 2.5). The first zero-crossing point away from the central frequency ν is given at $1/t_p$ and it is possible to consider a uniform excitation profile in the range of frequencies $\nu \pm \frac{1}{2t_p}$.

Nowadays, the development of arbitrary waveform generators (AWGs) allow to create shaped pulses modulating their amplitude, phase and frequencies within the pulse length t_p to improve the performance of pulse EPR experiments.[18]

3. Pulse sequences

Considering that real EPR samples consist of a large number of spins, in order to describe which are the effects of the interaction between the applied pulses and the unpaired electrons, it is useful to introduce a macroscopic model of the spin system. A vector model is briefly illustrated in the next paragraph; more details can be found in the books of WERTZ and BRUSTOLON.[3,4]

3.1 The vector model

Taking into account a packet of electron spins, it is possible to define a total magnetization vector $\vec{M}$ from the sum of the individual magnetic moments $\vec{\mu}_i$ (equation 27).

$$\vec{M} = \sum_i \vec{\mu}_i \tag{27}$$

If this ensemble of electron spins is placed into an external magnetic field $\vec{B}_0$, which is conventionally assumed to be directed along the *z* axis, the magnetization vector $\vec{M}$ undergoes a precession motion along the direction of $\vec{B}_0$ at the Larmor frequency (ω_L) written in equation (28).

$$\omega_L = \frac{g\beta_e}{\hbar}\left|\vec{B}_0\right| \tag{28}$$

In these conditions, a net magnetization $+M_z$ will be detected due to the excess of β spin states over the α spin states while the perpendicular components M_x and M_y are averaged out to zero. We define $M_0 = +M_z$ this initial thermal equilibrium of the spin packet into the external magnetic field $\vec{B}_0$.

Moving from a static laboratory frame to a rotating laboratory frame at the same value of Larmor frequency the precessing magnetization vector $\vec{M}$ appears stationary.

When a pulse $\vec{B}_1$ perpendicular to $\vec{B}_0$ ($\vec{B}_1 \ll \vec{B}_0$) is applied for a time interval t_p, rotating at the Larmor frequency ω_L, the spin system experiences it as stationary as well. Thus, the thermal equilibrium M_0 is perturbed because the magnetization vector undergoes an additional procession motion along the direction of $\vec{B}_1$ at an angular frequency

$\omega_1 = \frac{g\beta_e}{\hbar}\left|\vec{B}_1\right|$ with $(\omega_1 \ll \omega_L)$. The sum of the two precession motions results in a flipping of magnetization vector $\vec{M}$ from the *+z* axis towards the *xy* plane during the time interval t_p. Then, the vector $\vec{M}$ forms an angle ϑ with the *z* axis and the M_{xy} components become different from zero starting to precess as well on the *xy* plane (figure 3.1). The tilt angle ϑ is a function of the intensity of $\vec{B}_1$ and of the pulse length t_p, according to equation (29).

$$\vartheta = \gamma_e\left|\vec{B}_1\right|t_p \tag{29}$$

Choosing these two parameters it is possible to define the value of tilt angle ϑ that normally gives the name to the pulse applied. π and $\frac{\pi}{2}$ pulses are the most used in the pulse sequences: a π pulse flips the magnetization vector from *+z* axis to *–z*; a $\frac{\pi}{2}$ pulse moves $\vec{M}$ from *+z* axis to the *xy* plane.

Once the pulse is switched off, the magnetization vector experiences only the static magnetic field $\vec{B}_0$ therefore it tends to come back to the original thermal equilibrium. If a static detector is placed on the *y* axis it is possible to detect, immediately after the pulse, the shrinking of M_x and M_y components that will come back to zero with a *sin* or *cos* function at the resonance frequency of the spin packet.

Considering that this signal is “induced” by the application of a pulse, that it is recorded while the pulse is switched off and that it has an exponential decay, it is called *free induction decay* or FID.

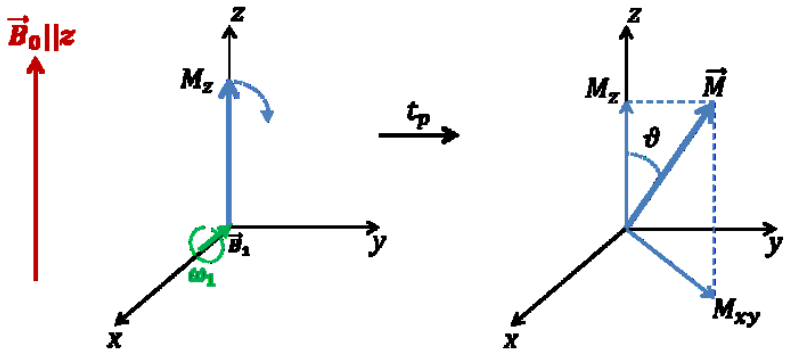

Figure 3.1. Scheme of the vector model.

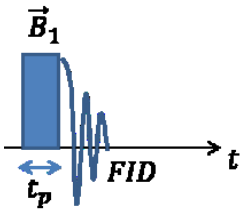

Figure 3.2. A pulse is always followed by a FID.

A FID signal is shown in figure 3.2.

The thermal equilibrium is restored through two different mechanisms: longitudinal relaxation and transverse relaxation.

The first one is related to the interaction between the spin system with the lattice in the surrounding that has the effect to recover the component M_z to M_0. This process is described by the relaxation time T_1 according to equation (30).

$$M_z(t) = M_0\left(1 - e^{-t/T_1}\right) \tag{30}$$

The transverse relaxation is related to spin-spin interactions which yield to a loss of coherence of the spin system on the *xy* plane. It occurs because the magnetic moments are influenced by local fluctuating magnetic fields of the other spins in their chemical environment; consequently, they start to precess with slight difference frequencies from the original Larmor frequency (ω_L) value. This determines a dephasing on the *xy* plane with an exponential decay (FID) up to the two components M_x and M_y come back to zero. This process depends on the relaxation time T_2. The exponential decay of a FID is related not only to a spin-spin interaction but many other processes contribute to it such as spin diffusion, instantaneous diffusion or spectral diffusion. Therefore, the relaxation time which includes all these terms that are involved in the dephasing of the spin packet in the *xy* plane is called *phase memory time* (T_M). The exponential decay of M_x and M_y components is written in equation (31)

$$M_{xy}(t) = M_0\, e^{-t/T_M} \tag{31}$$

T_1 and T_M are temperature-dependent: lower temperatures slow down both relaxation processes.

A representation of the two relaxation mechanisms is depicted in figure 3.3. How it is possible to observe $T_1 > T_M$. The values of these relaxation times are two important parameters to set-up an EPR experiment.

In CW-EPR spectra, T_1 and T_M have an influence on the lineshape and on the linewidth of the signal. In particular, small T_1 values enlarge the linewidth because the spin-lattice relaxation is related to the inverse of the EPR transition probabilities. A fast longitudinal relaxation means a fast electronic transition with a consequent EPR line broadening. On the contrary, if T_1 is really long it means that it is difficult to restore the thermal equilibrium and after the irradiation there is no difference anymore in the population of the two spin states (*saturation*). In general, it is useful to have a quite high T_1 value without reaching the saturation condition. T_M gives an additional contribution to the line broadening because the spin-spin interaction might change the energy levels of the spin states and this effect has an influence on the peak-peak distance.[3]

About pulse EPR spectroscopy, in order to increase the signal to noise ratio of an EPR spectrum, more than one scan are acquired. The time interval between one acquisition and the next one is strictly associated with the length of T_1 because it must be ensured that the spin system comes back to the initial thermal equilibrium before to restart the EPR experiment. Normally, a *short repetition time* $SRT \approx 5T_1$ is chosen. The phase memory time influences the time interval between the application of two pulses.

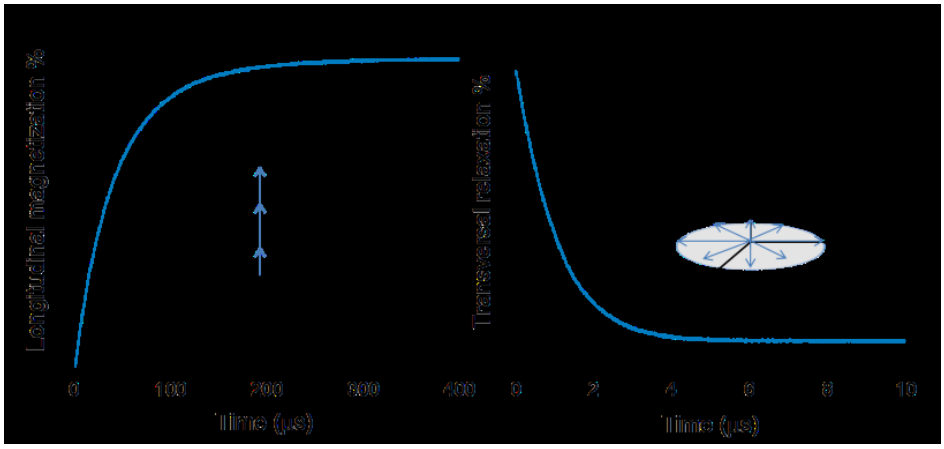

Figure 3.3. Experimental graphs of longitudinal (left) and transversal (right) relaxation mechanisms of BDPA radical 0.1% in polystyrene (PS) at room temperature.

Theoretically, the detection of the FID from a one-pulse EPR experiment might give information about the phase memory time and the resonance frequency of the spin system under investigation. If a series of spin ensembles with different Larmor Frequencies is present, the resulting FID is composed by the sum of the FIDs of each spin packet. This signal can be deconvoluted into its components through a Fourier transformation that yields the single Larmor frequencies of the spin packets.

The main issue of this approach is the so called *dead time* following the microwave pulse because the detector cannot record the EPR signal at the time when the pulse is switched off because the high power of pulse has to be dissipated to avoid detector damages. It means that some spin packets might leave no detectable signal beyond the dead time. For this reason several pulse sequences with two or more pulses were developed to probe specific magnetic interactions. In the next paragraph, the basic Hahn echo sequence is introduced.

3.2 The Electron Spin Echo signal

Applying two pulses separated by a time interval τ, called *evolution time*, two FIDs are generated after each pulse; additionally, a third EPR signal, called *electron spin echo* (ESE), appears after 2τ. This signal was discovered in 1950 by HAHN who applied two $\frac{\pi}{2}$ pulses separated by a certain evolution time.[19] Then, the pulse sequence was further improved by CARR (New Jersey) and PURCELL (Harward University) who suggested to substitute the second $\frac{\pi}{2}$ pulse with a π pulse.[20]

This pulse sequence 90 – τ – 180 – τ – echo, shown in figure 3.4, is called *Hahn echo sequence* and it is the basis for the detection of an EPR signal in all pulsed EPR techniques.

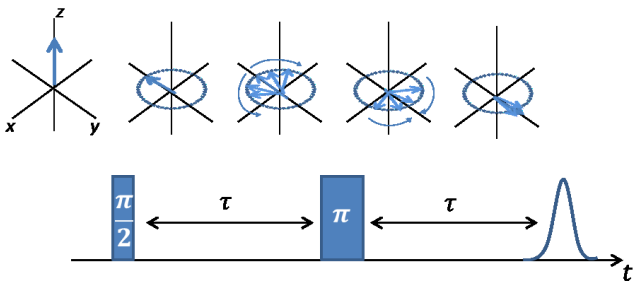

Figure 3.4. Hahn echo pulse sequence.

In order to understand the origin of the spin echo signal it is useful to refer to the vector model illustrated in the previous paragraph. The first $\frac{\pi}{2}$ pulse applied along the *x* axis flips the magnetization vector from the *+z* axis to the *y* axis. During the evolution time τ the spin packets dephase on the *xy* plane due to the local magnetic field inhomogeneities; thus, they precess with slight different frequencies and speeds. The second π pulse (called refocusing pulse) flips all these precessing spins of 180° degrees along the *x* axis on the *xy* plane while each of them keep moving with the same speed in the same rotation direction. Therefore, the spins will be progressively refocused on the *y* axis yielding at the time $t = 2\tau$ a spin echo signal. After that the spins will defocus once more. This EPR signal reproduces the magnetization of the FID following the first pulse but 180° phase shifted. Therefore, it is like an "echo" of the first FID without the drawback of the dead time and it is called *electron spin echo*. The longer is the evolution time τ the lower will be the spin echo intensity due to the T_M decay.

3.3 Pulsed EPR methods adopted in this thesis

In this paragraph the pulse EPR sequences employed in part III of this thesis are briefly illustrated. All of them enable the detection of a specific magnetic interaction occurring in the sample.

3.3.1 PELDOR/DEER pulse-sequence

PELDOR (Pulsed Electron Double Resonance), called also DEER (Double Electron Electron Resonance), is emerging as a powerful double-frequency EPR technique to detect inter spin distances between two paramagnetic centres in a biological system in order to investigate its structure. Measuring the dipolar coupling between the two unpaired electrons (section §1.1.4), PELDOR/DEER spectroscopy allows to probe their intramolecular distances with high resolution and reliability. This technique is fundamental to confirm crystallographic data of a biomolecule or to propose a model of a biomolecular system when there are no structural information. Several detailed reviews about this biophysical methodology have been written in the last years.[6,21–23]

As discussed in the section §1.1.4 the dipolar coupling term, $\widehat{H}_{DD}$, is hidden by stronger magnetic interactions in the general Hamiltonian of equation (14); therefore, in order to extract the distance information, it is

necessary to isolate this contribution applying specific pulse sequences. The first 3-pulse sequence to probe an interspin distance was suggested by MILOV in 1984,[24] figure 3.5.

Basically, the two interacting spins (A and B) have their own Larmor frequencies ν_A and ν_B due to their specific chemical environment.

A Hahn echo sequence with a long evolution time τ is applied at the frequency ν_A, chosen as detection frequency; at the same time a π pulse sweeps at the frequency ν_B (pumping frequency) between the $\frac{\pi}{2}$ pulse and the refocusing π pulse fixed at ν_A. Considering that the two electrons are dipolar coupled with a frequency ν_{dd} (equation 25), the flipping of B spins inverts the local field experienced by A spins affecting the resonance frequency of A spin. In this way, the intensity of the echo signal will be modulated at the dipolar frequency ν_{dd}. A PELDOR/DEER experiment consists of monitoring the intensity of the echo signal during the sweeping time of π pulse at ν_B. This 3-pulse sequence suffers from the dead time because the pumping pulse cannot be applied at the position of $\frac{\pi}{2}$ pulse. The two pulses in fact must not overlap. To overcome this issue an additional π pulse was placed after the Hahn echo sequence at ν_A so that the pumping pulse moves between the two π pulses generating a refocused echo.[25,26]

Recently, 5-pulse and 7-pulse PELDOR/DEER sequences were further proposed to detect long-range interspin distances and to improve the sensitivity and the intensity of PELDOR/DEER signal adopting shaped pulses.[27,28] However, today the 4-pulse PELDOR/DEER sequence is still largely adopted for characterization of several biomolecular structures.[22]

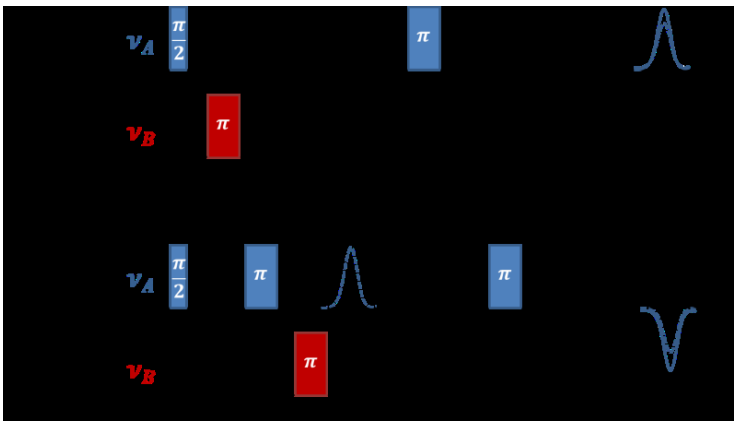

Figure 3.5. 3-pulse and 4-pulse PELDOR/DEER sequences.

EPR distance measurements in biological systems are performed in frozen solution yielding to an ensemble of biomolecules randomly oriented. Each spin contributes to the EPR spectrum with its own Larmor frequency leading to an inhomogeneous broadening of the EPR spectrum (figure 3.6).

To record a PELDOR/DEER trace the pumping and detection pulses must excite separately $\vec{\mu}_A$ and $\vec{\mu}_B$; therefore, a sufficient separation $\Delta\nu$ between the Larmor frequencies ν_A and ν_B is required ($\Delta\nu \gg \nu_{dd}$). PELDOR/DEER experiment fails for distances under 1.5 nm due to the high ν_{dd} value. Additionally, the excitation bandwidth of the pulses must cover completely the splitting of the dipolar coupling in order to excite all possible orientations of the two spins; therefore hard and short pulses are employed. Figure 3.6 shows an experimental field-swept Electron Spin Echo (ESE) signal of a biomolecule modified with two nitroxide spin labels at Q-band frequencies highlighting the pulse positions.

CW-EPR experiments allow to detect short distances under 1.5 nm because the strong dipolar coupling affects the lineshape of the EPR spectrum.[29–31] On the other side, a modulation is actually detectable for distances up to 9 nm.[32] The main challenge to overcome the upper distance limit is the length of the evolution time τ_2 that cannot exceed the phase memory time.

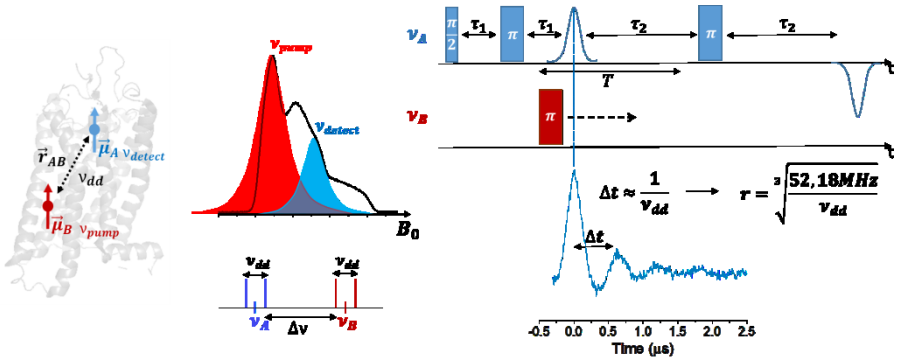

Figure 3.6. On the left a scheme of a biomolecule containing two interacting electron spins. On the centre, an experimental nitroxide swept-field ESE signal is shown with the pulse positions. On the right the 4-pulse PELDOR/DEER sequence is illustrated with an experimental PELDOR/DEER trace. The modulation of the refocused echo intensity allows to extract information on the interspin distance.

Many expedients were employed to make T_m longer in order to increase τ_2 and to probe long-range distances. One contribution to the phase relaxation is the nuclear spin diffusion due to the coupling between the electron spin with the protons of solvents and of the biomolecule. Deuterium shows a smaller magnetic moment compared with protons ensuring a reduction of this effect.[33] Therefore, PELDOR/DEER experiments are normally performed in deuterated solvents like D_2O,[34] if possible in deuterated biomolecules[35] or in both deuterated solvents and deuterated biomolecule with high gain in terms of sensitivity.[36] Furthermore, low temperatures play a critical role to increase the relaxation times; thus, generally the experiments are carried out between 10K and 60K, using liquid helium as cooling medium.[23] At this temperature, a cryoprotectant agent is added to prevent ice crystals formation and possible aggregation of the biomolecules. Both processes can lead to a reduction of T_m; so, a glassy agent like glycerol or perduterated glycerol (d_8-glycerol) maintains the sample in a glassy state during the freezing procedure.[37]

An experimental PELDOR/DEER trace presents a first intense modulation which corresponds to the intensity of the undetected spin echo, *zero-time* (figure 3.6); then, there are one or more modulations which are the sum of two dipolar contributions: an intramolecular term, due to the coupling between spin labels that belong to the same biomolecule, and an intermolecular term due to the coupling among spin labels of different biomolecules, equation (32).

$$V(t) = V_{intra}(t) \cdot V_{inter}(t) \tag{32}$$

$V_{intra}(t)$ is the term of our interest and can be described by the expression written in equation (33).[21,38]

$$V_{intra}(t) = V_0\left[1 - \lambda + \lambda\left(cos(\omega_{dd}t)\right)\right] \tag{33}$$

V_0 is the intensity of the refocused echo signal at t=0, when the pumping π pulse is not applied; λ is the *modulation depth*, related with the fraction of B spins coupled with A spins that are flipped by the π pulse at ν_B.

In order to reduce the intermolecular contribution, $V_{inter}(t)$, the concentration of samples are low, normally around 50μM.[23] However, after the acquisition of a PELDOR/DEER trace it is necessary to remove the residual intermolecular background contribution from the experimental data. For the analysis of the experimental PELDOR/DEER trace the well-

known DeerAnalysis program, developed from JESCHKE and co-workers, was employed in this thesis.[39] This program assume that the distances within the biomolecule are shorter than the intermolecular distances. It implies that the first part of PELDOR/DEER trace is dominated from the desired information while the last part of the trace is dominated from the intermolecular term that can be fitted with an exponential decay. Defining the beginning of a background correction function at some point of the experimental data, the first part of PELDOR/DEER trace is fitted by extrapolation, as shown in figure 3.7. After that, a background corrected PELDOR/DEER trace is obtained and it is possible to extract the modulation depth parameter (λ) from the reduction of the refocused echo intensity. Applying the Fourier transformation to the corrected experimental data it is possible to figure out the Pake pattern and to extract the distance distribution from the splitting between the two maxima (figure 3.7).[39] The outcomes of the analysis are strongly dependent from the quality of the experimental setup adopted, the signal to noise ratio and the length of the evolution time *T* that should allow to acquire at least 1.5 complete modulations to obtain reliable distances.[39]

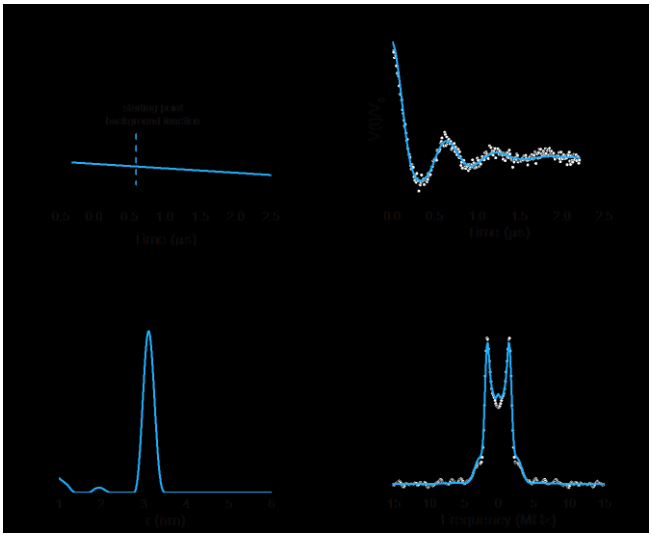

Figure 3.7. (a.) The black curve is one experimental PELDOR/DEER trace made up of both intermolecular and intramolecular terms. The cyan line is the exponential decay which fits the intermolecular contribution. (b) The background corrected trace is shown with the fit of the background correction model (cyan line). (c) Applying the Fourier transformation, the Pake Pattern is obtained and it is possible to calculate the dipolar frequency ν_{dd} in order to (d) extract the distance distribution.

The calculation of the distance distribution $P(r)$ from the dipolar evolution function $V(t)$ is a challenging step because small distortions in the dipolar function $V(t)$ can have large effects in the distance distribution function $P(r)$. Therefore, it is necessary to find a good compromise between the resolution of $P(r)$ and the influence of the experimental noise that may generate some artefacts.[39]

Many mathematical algorithms were suggested to solve this problem and nowadays the most used is the Tikhonov regularization procedure.[40] In this statistical approach, the best distance distribution $P(r)$ is found by the minimization of this function (equation 34):

$$G_\alpha(P) = \rho(\alpha) + \eta(\alpha) = \|S(t) - V(t)\|^2 + \alpha \left\| \frac{d^2}{dr^2} P(r) \right\|^2 \quad (34)$$

for a given regularization parameter α.

The equation (34) is made up of two terms: the first one, $\rho(\alpha) = \|S(t) - V(t)\|^2$, is the mean square deviation between the simulated $S(t)$ and the experimental dipolar function $V(t)$, defining the resolution of the experiment. The second one, $\eta(\alpha) = \alpha \left\| \frac{d^2}{dr^2} P(r) \right\|^2$ is the second-derivative of $P(r)$ weighted by the regularization parameter α. It represents the smoothness of the function at different α values. The larger is α the larger is the smoothness, the less is the resolution. The best regularization parameter is extracted plotting $log\eta(\alpha)$ vs. $log\rho(\alpha)$ that yields to a L-curve plot like that one in figure 3.8. The best compromise between resolution and smoothness of the $P(r)$ function is reached choosing an α value close to the turning point (red point in figure 3.8).[39]

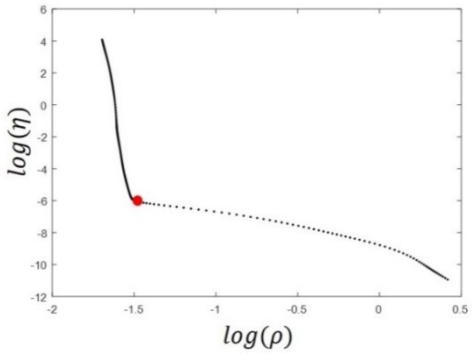

Figure 3.8. L-curve plot.

3.3.2 *Electron Spin Echo Envelope Modulation (ESEEM)*

It was already discussed in paragraph §3.2 that the intensity of the ESE signal depends on the value of the evolution time τ between the $\frac{\pi}{2}$ and π pulses (*electron spin echo envelope*). Therefore, it is possible to measure the exponential decay T_M-dependent of an ESE signal recording its intensity while the time interval between the two pulses of a Hahn echo sequence is gradually increased, as shown in figure 3.9.[41]

Another approach to detect the echo exponential decay consists of splitting the π pulse of the Hahn echo sequence in two $\frac{\pi}{2}$ pulses, separated by the time interval T. In this way, the 3-pulse sequence $90 - \tau - 90 - T - 90 - \tau -$ echo, shown in figure 3.9, is generated.[4] The combination of the third pulse with the first and the second $\frac{\pi}{2}$ pulses produce a series of unwanted primary echo signals; additionally, the effect of all three $\frac{\pi}{2}$ pulses on the magnetization vector produces the so called *stimulated echo* after a time $2\tau + T$.[19] The exponential decay of the stimulated echo is T_1-dependent and it is typically measured as a function of the time interval T keeping constant τ.[42]

In both 2-pulse and 3-pulse sequence the echo decay amplitude might be periodically varied due to weak hyperfine interactions of the electron spin with close magnetically active nuclei. This effect is called *Electron Spin Echo Envelope Modulation* (ESEEM) and was discovered by ROWAN, HAHN and MIMS in 1965.[43] The 2-pulse sequence suffers from the dead time because the high microwave power must dissipate before starting echo detection. The 3-pulse ESEEM sequence, called also *stimulated echo sequence*, is largely adopted to detect these weak electron-nuclear magnetic interactions in EPR samples.[44]

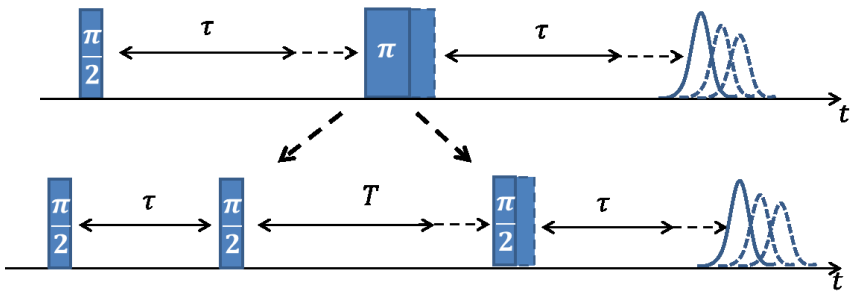

Figure 3.9. 2-pulse and 3-pulse ESEEM sequences.

The ESEEM effect is visible when the selection rules for an EPR transition ($\Delta M_S = \pm 1$ and $\Delta M_I = 0$), discussed in the section §1.1.2, breakdown and the "forbidden" transitions ($\Delta M_I \neq 0$) have a certain probability to take place. This occurs when the hyperfine coupling is anisotropic or in the case of quadrupolar interactions that produce a mutual influence of electron and nuclear spins in the effective local magnetic field experienced by both particles under the action of microwave pulses.[4,42] As a result, the electron spin echo decay is modulated at the Larmor frequency of nuclei which are hyperfine coupled and, after Fourier transformation of the time trace, it is possible to identify the nuclear frequencies contributing to the ESEEM modulation. To improve the quality of Fourier transformed data zero-points are added at the end of the experimental data.

The amplitude of this modulation is τ-dependent and suffers from *blind spots* that may appear in the EPR spectrum. It means that for particular τ values some nuclear frequencies (ω_n) may be suppressed according to equation (34).

$$\omega_n = \frac{2\pi n}{\tau} \quad n = (0, 1, 2, \dots) \tag{34}$$

This phenomenon can lead to a misinterpretation of the experimental data. Thus, normally , the 3-pulse ESEEM experiment is repeated at different τ values and a phase cycling procedure avoids that the unwanted echoes overlaps the desired stimulated echo.[4]

In part III of this thesis some 3-pulse ESEEM experiments will be shown to prove if the transmembrane peptide under investigation is properly incorporated into a lipid bilayer prepared with deuterated phospholipids.

4. Site-Directed Spin Labeling

Some biomolecules can be characterized by EPR spectroscopy because they naturally contain paramagnetic centres, such as metalloproteins containing transition metal ions or enzymes which catalyse biochemical reaction together with organic radicals as cofactors. However, the majority of natural biological systems are diamagnetic. In 1989, W. L. HUBBELL. and co-workers developed the site-directed spin labeling (SDSL) approach which allows to introduce a spin label in defined sites of a biomolecule.[2,45]

This methodology in combination with EPR spectroscopy has become a fundamental tool in structural biology to achieve structural information at atomic resolution on biomolecular structures.[46]

Some details about the spin labeling strategies and the most used nitroxide spin labels will be presented in the next paragraphs. Further details can be found in recent reviews.[47,48]

4.1 Spin Labeling Strategies

HUBBELL studied the bacteriorhodopsin, a transmembrane protein that does not contain any paramagnetic centre. In order to make it detectable by EPR, they conjugated the nitroxide spin label MTSSL (1-Oxyl-2,2,5,5-tetramethylpyrroline-3-methyl)methanethiosulfonate) to the protein backbone through disulphide bonds, according to the scheme of figure 4.1. The primary sequence of bacteriorhodopsin lacks cysteines; therefore some amino acids were replaced by cysteines through site-directed mutagenesis to have a selective linker for the spin label. Introducing one or more nitroxides at different positions it was possible to explore different regions of the protein extracting clear information about its secondary and tertiary structure using CW-EPR spectroscopy.[2]

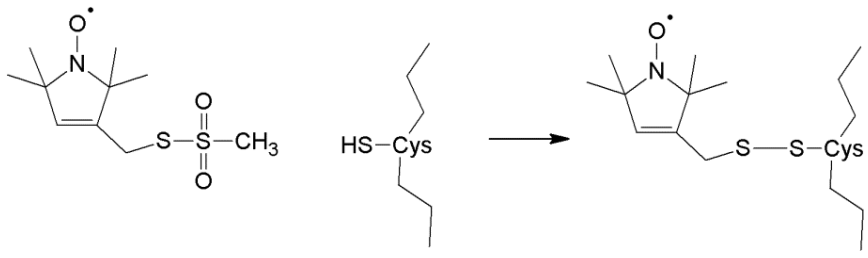

Figure 4.1. Scheme of MTSSL conjugation reaction with a cysteine.

Furthermore, many studies were performed to evaluate the effects of the introduction of nitroxides in the protein structure. It was observed that the information obtained from the EPR spectra reflect the native structure with neglecting perturbations due to the presence of spin labels.[45]

Since then, the post-synthetic chemical conjugation of cysteines with a nitroxide radical is one of the most employed approach to attach a spin label into a protein backbone.[49]

If a protein contains several cysteines the conjugation with a nitroxide spin label becomes non selective. Therefore the replacement of one or more native cysteines is required with the risk to alter the biomolecular structure. For this reason some unnatural amino acids, that will be illustrated in the next paragraph, were synthesized with the goal to replace selectively the residues that must be spin labelled through specific reactions which involved other functional groups (*orthogonal labeling strategy*).[50] Additionally, non-canonical amino acids, containing a nitroxide spin label in in their side chains, were developed so that they can be incorporated into an oligopeptide sequence directly during the solid-phase synthesis.[51]

EPR spectroscopy is also adopted for the characterization of spin labelled oligonucleotide sequences. Similarly to the protein, nitroxides can be incorporated during the solid-phase synthesis or through post-synthetic strategies. Nucleic acids offer several reactive sites that might be potentially modified by the conjugation with nitroxide radicals. The main issue is the selectivity of this procedure: considering that a nucleic acid is made up of a sequence of only four nucleotides it is necessary to “drive” the nitroxide towards some preferential labeling sites. Several convertible nucleosides are commercially available making it possible to introduce post-synthetically a spin label in defined positions by chemical or enzymatic approaches.[52,53] This is the most common procedure to obtain nucleic acids modified with nitroxide spin labels.

More recently, several molecular biology procedures allow to introduce biomolecules, previously engineered with nitroxide radicals, in a cell to characterize their structure in cellular environment by EPR.[54,55] Moreover, genetic encoding strategies of unnatural amino acid carrying a nitroxide radical were developed for the biosynthesis of spin labelled proteins.[56] These new methodologies have paved the way towards *in-cell* EPR spectroscopy. However, despite several advances, the direct detection of a nitroxide EPR signal in cell still remains challenging. One of the main issue is

the life-time of the radical in the reductive cellular environment. Many synthetic efforts were made to increase the stability of spin labels in these conditions using bulky substituents around the $NO^{\cdot}$ radical.[57]

4.2 Nitroxide spin labels

In the last decades, a huge variety of spin labels have been proposed for the EPR structural characterization of biomolecules. Different chelating tags for paramagnetic transition metal ions, like Gd(III),[58,59] Cu(II)[60] and Mn(III)[61] are commonly used so as carbon-centred radicals like trityl radicals.[62] However nitroxides are today the most important spin label class employed in SDSL approach.[48,63]

Nitroxide spin labels present the general form $R^1 - NO^{\cdot} - R^2$. The unpaired electron is placed in the antibonding π^*_{N-O} molecular orbital resulted from the overlap between the two p_z orbitals of Nitrogen and Oxygen. The energy of the π^*_{N-O} is closer to the nitrogen $2p_z$ atomic orbital and the spin density is delocalized along this $N - O$ bond.[49]

The chemical structure of a nitroxide spin label is based on five- (pyrrolidines and pyrrolines) and six- (piperidines and piperazines) membered rings or on systems made up of two condensed rings (isoindolines). These heterocycles are normally *gem*-substituted by alkyl substituents to increase the stability of the radical shielding sterically the $NO^{\cdot}$ group. Bulky substituents have also the effect to elongate the relaxation time T_m, figure 4.2. Longer T_m enables to perform PELDOR/DEER experiments at higher temperatures allowing to cool down using the cheaper liquid Nitrogen instead of liquid helium. In 2016, a comparative study of BAGRYANSKAYA and co-workers[57] has demonstrated the capability of spirocyclohexyl substituents to achieve more precise PELDOR/DEER distance measurements in a range of temperature of 100 - 180 K in comparison with the more common *gem*-ethyl groups.

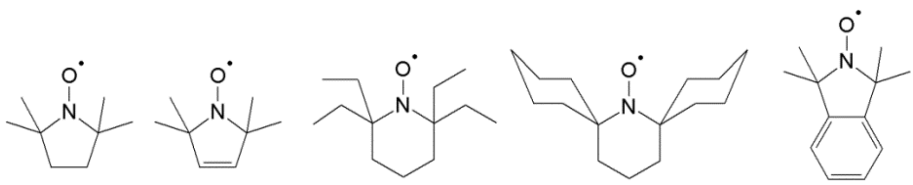

Figure 4.2. Examples of nitroxide spin labels adopted in SDSL.

EATON and co-workers[64] were able to perform a PELDOR/DEER experiment at room temperature on a doubly labelled T4 lysozyme adopting a nitroxide radical shielded by two *gem*- spirocyclohexyl groups.

In general, the advantages of this class of spin labels are the small sizes which do not strongly affect the biomolecular structure; moreover, the heterocyclic scaffold makes nitroxide "tunable" offering a variety of orthogonal labeling strategies.[63] One key point to choose the proper SDSL strategy is the rigidity of the spin label integrated into the macromolecular structure: many synthetic efforts were made to reduce the dynamic of the radical that can lead to a misinterpretation of the experimental data in terms of structural information.[65] MTSSL is the nitroxide most used for CW and pulse EPR characterization of proteins due to its technical ease of incorporation and its minimal impact on the secondary structure. However, the long linker between the backbone and the $NO^{\cdot}$ moiety, consisting of four single bonds, offers a large conformational space for the spin density. Therefore, several analysis of PELDOR/DEER interspin distances in different biomolecules was supported by rotamer libraries and Molecular Dynamic (MD) simulations.[66,67] In order to decrease the flexibility of MTSSL spin label, in the last years different linkers with less rotable bonds were proposed yielding to narrower and more accurate PELDOR/DEER distance measurements in proteins.[68,69] Moreover, spin labels that can be conjugated through other functional groups to amino residues different from cysteines were developed.[70] Alternatively, unnatural amino acids can be genetically encoded to create specific labeling sites into the backbone of the protein or already carrying a nitroxide spin label. This approach has the advantage to avoid the use of a linker to connect the nitroxide to the backbone. Figure 4.3 shows some of these residues.

In 2009, FLEISSNER and co-workers[50] suggested to introduce into the protein backbone an acetylphenylalanine as selective labeling residue thanks to its carbonyl group that can be used for a post-synthetic conjugation with an hydroxylamine nitroxide radical to achieve a spin labelled amino acid, called K1 and shown in figure 4.3.

The spin label TOAC (2,2,6,6,-tetramethyl-N-oxyl-4-amino-4-carboxylic acid), shown in figure 4.3, is a non-native amino acid that shows a cyclic sidechain which confers a strong restricted mobility.[71] It was employed in several EPR studies to investigate the dynamic, backbone conformations and secondary structures of proteins.[71–73]

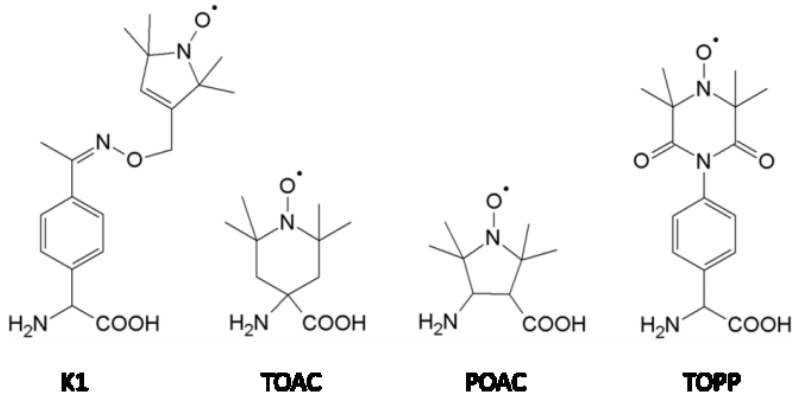

Figure 4.3. Unnatural amino acids that can be incorporated into the proteins backbone for EPR characterization.

However, considering the constraints on the side chain, this spin label does not easily adapt to the secondary structure of the protein and might disturb it. Other rigid spin labels derived from TOAC are β-TOAC and POAC (2,2,5,5,-tetramethylpyrrolidine-N-oxyl-3-amino-4-carboxylic acid). Both of them are β-amino acids because they show two methylene groups between the amino and the carboxylic functional groups; therefore, they were employed to explore the conformations of β-peptides.[74,75]

In order to reduce the influence of TOAC conformation on the secondary structure of a protein, in 2011 STOLLER and co-workers[76] developed a spin label which keeps some constraints on the nitroxide radical moiety without strongly affecting the protein structure. The spin label TOPP (4-(3,3,5,5-tetramethyl-2,6-dioxo-4-oxylpiperazin-1-yl)-L-phenylglycine) is a non-native amino acid derived from a phenylglycine which is conjugated with a piperizine ring carrying the nitroxide radical, as shown in figure 4.3. Density functional theory (DFT) calculations highlighted that C_α-C_β bond and N-$O\cdot$ radical bond are aligned to the same axis due to the two carbonyl groups which make nearly planar the piperizine ring.[76] PELDOR/DEER experiments at X-band frequencies (9 GHz) on a TOPP-labelled alanine-rich oligopeptide have revealed that TOPP spin label does not have an influence on the secondary structure yielding to narrow distance distributions in solution, comparable with that one predicted by spin labelled oligopeptide models.[76] A recent comparative study on a WALP transmembrane peptide has confirmed the higher accuracy and reliability of TOPP spin label over MTSSL for PELDOR/DEER measurements in solution and also in lipid bilayer.[77]

Considering the rigidity of this nitroxide radical, TOPP spin label was also employed for an orientation-selection PELDOR/DEER study at W-band frequencies (95 GHz).[14] The results have revealed some degree of freedom around the two single bonds because $\pm 20°$ of libration were required to fit the experimental data. However, the libration around one axis does not affect the position of $NO^{\cdot}$ moiety in the space; therefore, it has no impact in the distance distributions measured.

All these data suggest that TOPP spin label is a promising candidate for structural characterization of peptides by EPR spectroscopy. Part III of this thesis is dedicated to an EPR project where TOPP spin label is employed for structural investigation of β-peptides in solution and in lipid bilayer.

5. Other methodologies in structural biology

The role carried out by a biomolecule is strictly associated with its structure; therefore, several efforts have been made to characterize biological structures in order to clarify structure-function relationship. New tools are constantly developed to improve the technical performance in terms of resolution, sensitivity and speed of analysis with the goal to achieve more clear and detailed pictures of the biomolecules and the biochemical pathways in which they are involved.

Today X-ray crystallography is the most important technique adopted for the structural characterization of biological systems. Up to June 2018, more than 140.000 macromolecular structures were deposited in Protein Data Bank (PDB), whose almost 90% are achieved through X-ray crystallography (∼126.500). The remaining 10% (∼12.250) comes mostly from experiments performed through Nuclear Magnetic Resonance (NMR) spectroscopy in solution [78] or in solid-state.[79]

Starting from the beginning of 2000, the improvements of Electron Microscopy with the possibility to study biological samples in solution at cryogenic temperatures (below -180°C) has opened new frontiers in biochemistry. Cryo-electron microscopy (Cryo-EM) has allowed to obtain detailed 3D-pictures of biological systems at near-atomic resolution.[80–82] More than 2000 Cryo-EM structures are today present in PDB. The potential of this innovative approach in structural biology has induced the scientific community to award the Nobel Prize in Chemistry 2017 to Professors JACQUES DUBOCHET, JOACHIM FRANK and RICHARD HENDERSON who developed this methodology causing a “resolution revolution” in structural biology.[83]

An alternative optical method called FRET (Fluorescence Resonance Energy Transfer) enables to achieve structural information at atomic resolution by detecting the distance between two light-sensitive molecules (fluorophores) attached to a biomolecule.[84] When the donor fluorophore is excited with a specific wavelength, it may transfer the energy to the acceptor fluorophore through a non-radiative dipole–dipole coupling. The efficiency of this energy transfer is inversely proportional to the sixth power of the distance between donor and acceptor, making FRET extremely sensitive to small changes in distances inside the biological system under investigation. This method is widely used to study the structure and dynamic of proteins,[85,86] nucleic acids[87] and macromolecular complexes.[88,89]

EPR spectroscopy plays an its own important role in this field due to its peculiar features: EPR experiments can be performed in solution overcoming the challenges related to the crystallization process required by X-ray crystallography. In this way it is possible to study a biological system in its natural environment. Additionally, EPR shows higher sensitivity than NMR spectroscopy because the electron gyromagnetic ratio is much bigger than the nuclear gyromagnetic ratio $\left({\gamma_e}/{\gamma_H} \sim 660\right)$. Moreover there are no size limitations, allowing, for instance, to monitor a protein aggregation process.[90]

In comparison with FRET methodology, fluorophores have larger sizes than EPR spin labels, posing the risk of disturbing much more the natural conformation of the macromolecule. Additionally, it is possible to employ the same spin labels, simplifying a lot the labeling procedure, differently from FRET where the presence of two different fluorophores is always required.[84]

Continuous-wave EPR (CW-EPR) at X-band frequencies (9 GHz / 0.34 T) is largely adopted to characterize the coordination environment of paramagnetic metal ions in biological systems[91,92] or to explore the mobility and dynamics of nitroxide spin labels. If the spin-labelled site presents fast Brownian motions the correlation times of the nitroxide are of the order of $\sim ns$ yielding to three narrow EPR lines. If the mobility of nitroxide is restricted due to the interaction with neighbouring side chains or backbone atoms the EPR linewidth increases. It is possible to correlate the linewidth with the peculiarities of the binding site environment achieving some mobility parameters of different secondary structure elements.[45,48] The magnetic parameters can give also information on the solvent accessibility of the spin labelled site and on the polarity of the nitroxide microenvironment. The solvent influences the spin density of nitroxide radical modifying the nitrogen character of the π^*_{N-O} orbital. This effect reflects on slight differences in *g* and *A* values.[48,49]

Pulsed EPR methods, in particular at high fields and frequencies, give an essential contribution to the interpretation of complex EPR spectra of radical cofactors or reaction intermediates; moreover, allow to explore complex molecular dynamics and to probe long-range interspin distances.[10]

6. Interpretation of CW-EPR spectra of Cu(II) complexes

Part II of this thesis focuses on CW-EPR investigation of geometries and stereochemistries of binary and ternary Cu(II) complexes with some ligands with biological relevance. In this chapter the most important spectroscopic features of Cu(II) CW-EPR spectra are summarized to make easier the comprehension of the experimental results. More details can be found in the review of GOODMAN.[93]

Cu(II) ion has a d^9 electronic configuration and, therefore, presents one unpaired electron ($S = \frac{1}{2}$). As introduced in the paragraph §1.1, the magnetic moment associated to one electron in an atom is the result of the sum between the two magnetic momenta $\vec{\mu}_e$ and $\vec{\mu}_l$ related with the spin angular momentum $\vec{S}$ and the orbital angular momentum $\vec{l}$, respectively, of the electron. This interaction is called *spin-orbit coupling* and determines a deviation on the *g*-factor value from that one of an isolated electron ($g_e = 2.0023$). The spin-orbit coupling constant λ for a defined electronic configuration depends on the nuclear effective charge Z_{eff} and the average of the distance electron-nucleus.[5]

The existence of the orbital angular momentum $\vec{l}$ is strictly related to the degeneration of the orbitals involved in the spin-orbit coupling. When a transition metal ion is placed into a crystal field, the degeneration of *d*-orbitals is removed according to the direction of the ligands. As a result, the orbital angular momentum is partially or completely quenched so that, in these conditions, the magnetism should depend essentially on the electron spin $\vec{S}$.[5] However, when the system is placed into an external magnetic field, $\vec{B}_0$ induces a circulation of electrons perpendicularly to its direction. As a result, from a quantum mechanics point of view, the wave-functions of two orbitals perpendicular to the direction of the external magnetic field are intermixed restoring an angular orbital contribution. The entity of this mixing depends on the magnitude of the induced orbital motion and on the spin-orbit coupling constant. Therefore, this effect is very large for heavy atoms while it is negligible in the case of organic radicals.[5]

In particular, the mixing between two electronic states occurs when two orbitals can commute to each other. It means that it is possible to convert one orbital to another one by "rotating" it around the direction of the external magnetic field $\vec{B}_0$.[93] In general, if we consider the *d*-orbitals of a transition metal ion, different couples of orbitals commute to each other:

for instance, it is possible to convert the orbital d_{xy} in the d_{xz} orbital by a rotation of 45° around the *x* axis; alternatively, it is possible to convert the orbital d_{xz} in d_{yz} by a rotation of 45° around the *z* axis and so on.[93]

The circulation of electrons on the perpendicular plane of $\vec{B}_0$ creates an additional magnetic field which tends to oppose to the applied ones shifting the EPR transition to another magnetic field value. Therefore, the restore of the orbital angular momentum has the effect to deviate the *g*-factor from the g_e value. The magnitude of Δg shift is a function of λ and of the energy difference ΔE between the two electronic states involved in the orbitals commutation, according to equation (35).

$$g = g_e - \frac{n\lambda}{\Delta E} \tag{35}$$

The value n can be easily deduced, in a first approximation, by the so called *magic pentagon*, shown in figure 6.1, that indicates how many times one *d*-orbital can be converted to another one by rotation along one axis taking into account the symmetry representations of the group theory.[4]

In general, for transition metal ions with less than half full *d*-shell (d^n with $n < 5$), $\lambda > 0$ and $g < g_e$; on the contrary, for transition metal ions with more than half full *d*-shell (d^n with $n > 5$), $\lambda < 0$ and $g > g_e$, according to equation (35).[4]

The symmetry of the ligand field has a strong influence on the entity of the spin-orbit coupling and, consequently, on the *g* and *A* values recorded in the CW-EPR spectrum. Therefore, CW-EPR spectroscopy is a very sensitive method to characterize the geometries of these metal complexes.

In the next paragraph, the effects of the ligands on the energies of Cu(II) ions *d*-orbitals is discussed following the *crystal field theory*. It describes the breaking of degeneration of *d*-orbitals as a consequence of the static electric field generated by the ligands considered as negative point charges.[94]

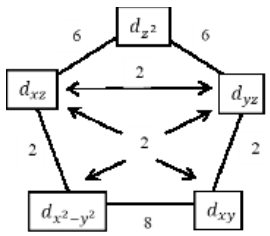

Figure 6.1 The magic pentagon.

6.1 Electronic configurations of some Cu(II) complex geometries

Cu(II) ions, differently from the other transition metal ions, do not have a preferential coordination geometry but show a certain plasticity according to the features of the ligand field.

6.1.1 Tetragonally elongated octahedral crystal field

In general, when Cu(II) ions are placed into an octahedral crystal field, the ligands are directed along the three *x*, *y* and *z* axis of the molecular frame. In this case, the degeneration of *d*-orbitals is selectively removed: d_{z^2} and $d_{x^2-y^2}$ have the highest probability to find the electron along the three axis and will be, therefore, destabilized by the ligands giving two degenerate orbitals at higher energy and forming an e_g set, according to the group theory. The other three orbitals d_{xy}, d_{xz} and d_{yz} have the maximum probability to find the electron along the bisectors and will be stabilize by the ligands moving to lower energy and forming t_{2g} set. Therefore, the orbital's degeneration is not completely removed and the energy separation between the t_{2g}. and e_g sets is called Δ_{oct}, figure 6.2.[94]

In biological fluids, the most common coordination geometry is that one of a tetragonally elongated octahedron due to Jahn-Teller distortions.[95]

In this case, the ligands (L) along the *z* axis are placed a bit farther by the metal centre than those on the equatorial plane so that the distance $M - L_z > M - L_{xy}$. As a result, the orbitals d_{xz} and d_{yz} will be more stabilized than d_{xy} in the t_{2g} set of orbitals; additionally, d_{z^2} will move to lower energy than $d_{x^2-y^2}$ in the e_g set of orbitals.

Consequently, taking into account the d^9 electronic configuration of Cu(II) ions, the unpaired electron will be localized in the $d_{x^2-y^2}$ orbital, as shown in figure 6.2.[94]

Which orbitals can commute with the $d_{x^2-y^2}$ orbital? Applying a magnetic field parallel to the *z* axis, the electron in the orbital d_{xy} commute with the unpaired electron located in $d_{x^2-y^2}$ orbital; therefore, according to the magic pentagon of figure 6.1.[93]

$$g_{||} = g_z = g_e - \frac{8\lambda}{E_{x^2-y^2} - E_{xy}} \qquad (36)$$

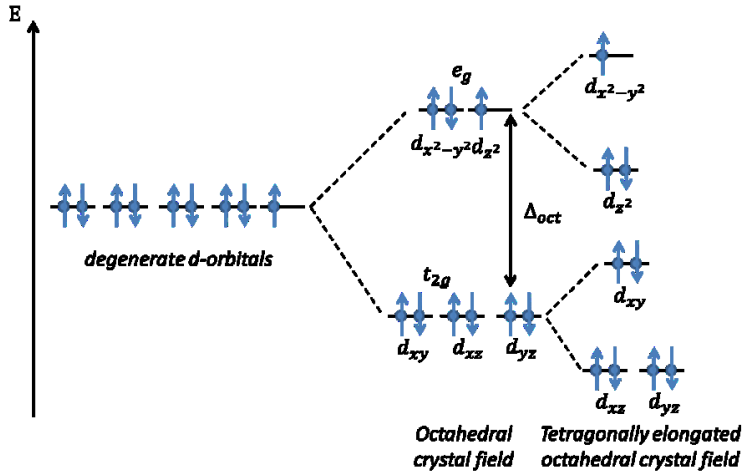

Figure 6.2. Splitting of *d*-orbital of one Cu(II) ion in an octahedral and a tetragonally elongated octahedral crystal field.

Applying a magnetic field perpendicular to the *z* axis, the electron in the orbital d_{xz} and d_{yz} commute with the unpaired electron located in $d_{x^2-y^2}$ orbital; therefore, according to the magic pentagon of figure 6.1.[93]

$$g_{\perp} = g_{xy} = g_e - \frac{2\lambda}{E_{x^2-y^2} - E_{xz,yz}} \tag{37}$$

Considering that for a d^9 electronic configuration $\lambda < 0$ the Cu(II) complex will present the following magnetic parameters:[4]

$$g_{||} > g_{\perp} > 2.0023 \tag{38}$$

6.1.2 Tetragonally compressed octahedral crystal field

In the case of a tetragonally compressed octahedral Cu(II) complex, on the contrary, the ligands along the *z* axis are placed a bit closer to the metal centre than those on the equatorial plane so that the distance $M - L_z < M - L_{xy}$. As a result, the orbitals d_{xz} and d_{yz} will be more destabilized than d_{xy} in the t_{2g} set of orbitals; additionally, $d_{x^2-y^2}$ will move to lower energy than d_{z^2} in the e_g set of orbitals. Consequently, the unpaired electron will be localized in the d_{z^2} orbital, as shown in figure 6.3.[94]

Which orbitals can commute with the d_{z^2} orbital?

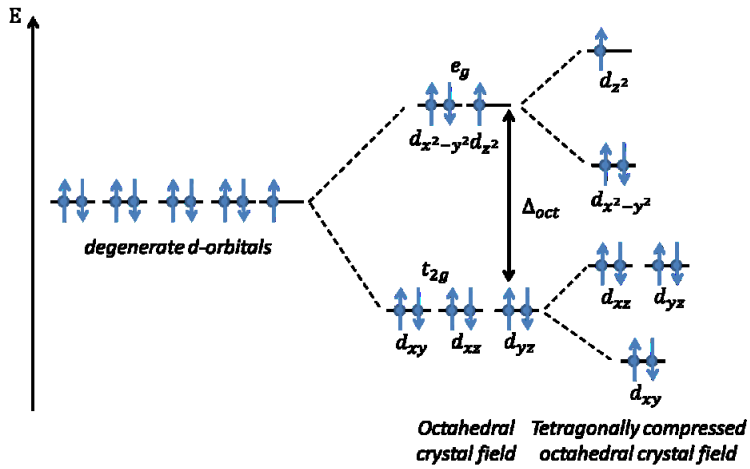

Figure 6.3. Splitting of *d*-orbitals of one Cu(II) ion in an octahedral and a tetragonally compressed octahedral crystal field.

Applying a magnetic field parallel to the *z* axis, the d_{z^2} orbital does not commute with any other *d*-orbital; therefore

$$g_{||} = g_z = g_e = 2.0023 \tag{39}$$

Applying a magnetic field perpendicular to the *z* axis, the electron in the orbital d_{xz} and d_{yz} commute with the unpaired electron located in d_{z^2} orbital; therefore, according to the magic pentagon of figure 6.1.[93]

$$g_{\perp} = g_{xy} = g_e - \frac{6\lambda}{E_{z^2} - E_{xz,yz}} \tag{40}$$

As a result it will be:

$$g_{\perp} > g_{||} = 2.0023 \tag{41}$$

6.1.3 Square-based pyramidal crystal field

A square-based pyramidal arrangement of ligands can be easily derived by the octahedral coordination geometry removing one ligand lying on the *z* axis. Then, the d_{z^2} orbital will be largely stabilized and also the d_{xz} and d_{yz} orbitals will be lowered in energy. Consequently, the unpaired electron will be placed in the $d_{x^2-y^2}$ orbital at highest energy, yielding to a similar electronic configuration already observed for tetragonally elongated octahedron in section §6.1.1.

6.2 How to calculate $g_{||}$ and $g_{\perp}$ of Cu(II) complexes

When a CW-EPR spectrum of a Cu(II) complex is recorded in solution at room temperature, the fast Brownian motions averaged out the magnetic parameters and only isotropic g_{iso} and a_{iso} values can be extracted. In the case of Cu(II) complexes, the hyperfine interactions between the unpaired electron and copper nucleus $\left(I = \frac{3}{2}\right)$ gives an EPR spectrum at room temperature with four EPR lines. Additionally, if the ligands present, as donor atoms, magnetically active nuclei a superhyperfine interaction will be also visible.

In part II of this thesis, several examples of low temperature EPR spectra of Cu(II) complexes with axial symmetry are shown to identify the parallel and the perpendicular components of *g*-tensor and *A*-tensor. In frozen solution, we have an ensemble of microcrystals randomly oriented in the space: applying a magnetic field $\vec{B}_0$ along the *z* direction there are few complexes with the spin parallel to the direction of $\vec{B}_0$ while several molecules have the spin oriented on the perpendicular plane to $\vec{B}_0$. Therefore, the intensity of $g_{\perp}$ is much bigger than that one of $g_{||}$. Moreover, for Cu(II) complexes in frozen solutions, the EPR lines related to $g_{||}$ will be split in four lines separated by an hyperfine $A_{||}$ constant and $g_{||}$ can be calculated by the midpoint of these four lines. The perpendicular part of the EPR spectrum will be split in four EPR lines as well separated by an hyperfine $A_{\perp}$ constant. Normally, $A_{||} \gg A_{\perp}$ and the four perpendicular EPR lines are not well resolved but form all together a very broad band. Metal complexes which have low symmetries yield more complicated EPR spectra where three different *g* and *A* values are measurable. In order to better resolve the *g* anisotropies, as discussed in chapter 2, it is useful to move from X-band towards higher fields and higher frequencies.[96]

The superhyperfine constants can be extracted as well by these spectra paying attention on the molecular frame of the ligands which often differ from that one of the metal centre. In particular, the donor atom of the ligand gives its maximum contribution to the superhyperfine coupling along the bond with the metal ion. The bond *M-L* is, therefore, assumed to be the *z* axis of the molecular frame for the ligand. In the case of a square-planar coordination geometry, the *z* axis of the metal ion is perpendicular to this plane, so that it is not coincident with the *z* axis of the ligands placed in the equatorial plane.[93] As result, in the parallel part of CW-EPR spectrum it is

possible to measure the perpendicular superhyperfine constant $A_{\perp}^{L}$; while, in the perpendicular part, if visible, the parallel superhyperfine constant $A_{\parallel}^{L}$ can be extracted.

Many times an extra-peak overlaps the perpendicular part of CW-EPR spectra acquired in frozen solution. These additional signal is typical of systems which present large *g* and *A* anisotropies and arise from the so called *angular anomalies*.[4] For Cu(II) complexes with axial symmetry only two resonances are expected corresponding to the two orientations of $\vec{B}_0$ along the *z* axis or on the *xy* plane. However, moving from the parallel to the perpendicular part of the spectrum some off-axis orientations of $\vec{B}_0$ can yield these "anomalies". The field of this extra–peak can be used in connection with the parallel parameters to estimate with a certain accuracy $g_{\perp}$ and $A_{\perp}$ components.[97,98] In any case, if there are some ambiguities in the interpretation of the spectra it is useful to move to Q-band or W-band frequencies.[4]

II. PART

EPR CHARACTERIZATION OF CU(II) COMPLEXES

7. Role of Copper in biological systems

All living organisms survive thanks to a fine equilibrium among several chemical constituents that maintain the physiological conditions. Such components are not just derived from "organic" elements, like carbon, hydrogen, oxygen, nitrogen and some sulphur and phosphorous compounds that form the most important biomolecules; but they include many essential inorganic metals which interact with these systems. The chemistry of a cell operates in a ionic medium which contains almost twenty elements. For these reasons, it is important to describe cell biochemistry not only in terms of genome and proteome, the whole family of genes and proteins in a cell line, but also in terms of "metallome" which refers to the cell metal content.[99,100] Furthermore, the interplay among these three "characters" has to be investigated for a deep comprehension of all biochemical pathways.[101]

Among the biometals, copper is an essential micronutrient because it is a transition metal which can exists in nature in two oxidation states: Cu(I) and Cu(II). Copper ions are important cofactors in a family of enzymes, called "cuproenzymes", which catalyse key biochemical redox reactions. The eventual copper deficiency ("hypocupremia") provokes serious pathological conditions.[102] For instance, these metal ions are involved in free radical detossification through the Cu-Zn superoxide dismutase (Cu-Zn SOD); the lack of copper ions can cause the oxidation of several cell components.[103] Cytochrome c oxidase is a large transmembrane protein located in the mitochondrial membrane and represents the complex IV of the electron transport chain. This enzyme drives the key step which converts molecular oxygen to two water molecules thanks to a series of redox reactions that involve Cu and Fe centres. A deficiency of these metals reduces the production of ATP.[104]

On the other side, Cu is also a potent cytotoxin when it is accumulated exceeding the cellular needs. In this case, Cu rapidly participates in reactions which produce highly reactive oxygen species (ROS).[105] Moreover, the excess of copper is able to displace other metal cofactors from their natural ligands in key cellular signalling proteins. For instance, Cu(II) ions are able to displace Zn(II) in the zinc-fingers of the estrogen receptors involved in DNA-binding resulting in non-specific receptor-DNA interactions.[106]

Considering this ambivalent nature of Cu, the mechanisms of uptake, transport, storage and efflux of copper ions in the different compartments are finely regulated by a complex copper trafficking pathway. It consists of several copper transporters and "metallochaperones" which has the critical task to maintain the copper homeostasis preventing its toxic accumulation.[107] These systems are cuproproteins that guide and maintain the functional oxidation state delivering copper ions safety to the appropriate target.[107] A dyshomeostasis of copper from the physiological concentrations typical of each compartment might cause the onset of metabolic disorders.[108]

Two well-known pathologies strictly associated with copper dyshomeostasis involve a dysfunction of specific copper transporters: Menkes disease is a genetic disorder that reduces copper levels in the body due to genetic mutations of copper transporter ATP7A which mediates the uptake of copper from food at the liver level.[109] Wilson disease is an autosomal-recessive disease caused by mutations in the ATP7B gene which encodes a transporter responsible of copper excretion always at the liver. As a result, the copper excess is released in the blood flux and it is accumulated in different compartments of the body altering the organs' functionalities.[110]

It is also well-known that copper is present in a large amount in human brain where it is unevenly distributed. Copper ions reach easily this compartment because they can cross the blood-brain barrier directly.[111] Experimental evidences highlight that both copper content and distribution in brain change during development and with the age.[112] Moreover, alterations of copper homeostasis seem to be connected with neurodegenerative disorders such as Alzheimer (AD), Parkinson (PD), Amyotrophic Lateral Sclerosis (ALS) or "prion" diseases.[112–117] However, in contrast to Menkes' and Wilson's disorders the role of copper in these pathologies is still not fully understood.

When we talk about copper in biological fluids, it must be taken into account that copper ions are never isolated but they are always dissolved in complex matrices. In this kind of medium there is a competition among several biological molecules which can coordinate the metal ions forming complex species. Therefore, it is important to point out that copper ions participate to a biochemical pathway never "alone" (in other words, as free ion) but coordinated by biological ligands. This makes the investigation of

metals' involvement in pathological conditions a challenging task.[11] Many times the construction of simple models are required to reduce the biological complexity in order to define the stereochemistry and the role of the different metal species which can form.[11]

In this scenario, this part of the thesis focuses on the CW-EPR characterization of binary and ternary Cu(II) complexes with some ligands of biological relevance in order to extract some bioinorganic implications from the experimental data. The experimental results of two EPR projects will be shown in the next chapter.

In the first, the formation of copper(II) complexes with two aminoacidate ions carrying a positive or a negative charge in their side chains under physiological conditions is investigated. In particular, two abundant amino acids in brain are considered: L-glutamic acid and L-arginine.

It is well-known that L-glutamic acid is an important neurotransmitter[118] and presents a negative carboxylate group in its side chain at pH around the neutrality. L-arginine is another essential amino acid which shows in the same conditions a positive guanidinium group. Some experimental evidences have highlighted an altered arginine metabolism in AD, suggesting a possible involvement of this amino acid in the pathogenesis of AD.[119,120] Taking into account all these considerations, the formation of binary and ternary copper(II) complexes with these two biological ligands were investigated *in vitro* by CW-EPR spectroscopy to characterize their peculiar geometry in aqueous solution.

In particular, aminoacidate ligands coordinate copper(II) giving rise to CuN_2O_2 chromophore in which the two nitrogen atoms of the amino groups could be in a *trans* or in a *cis* conformation, as shown in figure 7.1.[121]

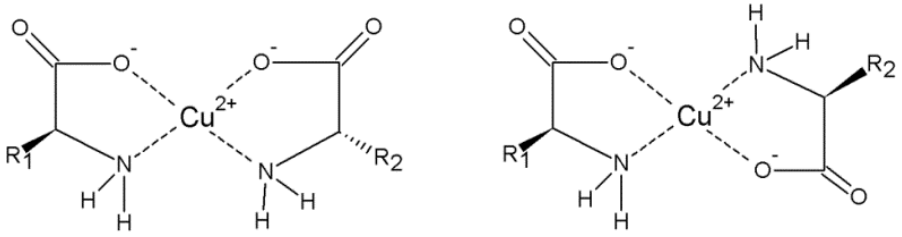

Figure 7.1. Two general L-aminoacidates coordinate Cu(II) ion in a *cis* (left) or in a *trans* (right) conformations forming a CuN_2O_2 coordination plane.

In the case of two L- (or D-) aminoacidate ligands, the side chains are placed on the same side of the coordination plane when the *trans* conformer is obtained; viceversa, on opposite faces when the *cis* forms.

If the ligands have two different configurations (one L- and the other D-), a reverse stereochemistry is achieved.[121]

The groups of YAMAUCHI[121] and PETTIT[122] were greatly involved in giving reason of the extra-stability of copper(II) complexes with aminoacidates having charged side chain groups, which could exert intramolecular electrostatic interactions. They stressed the influence of these non-covalent interactions on the ratio between *cis* and *trans* conformers.[121,123,124]

Therefore, in this project, the coordination environment of copper(II) complexes with arginate (Arg) and glutamate (Glu) was re-considered to evaluate the influence of the electrostatic interactions between the charged side chains on the stability of *cis* and *trans* conformers.

The second project focuses on the CW-EPR characterization of ternary copper(II) complexes with 1,10-phenantroline, as primary ligand, and different amino acids, as secondary ligands.

In the past decades several studies demonstrated how some copper complexes, in particular those including 2,2'-bipyridine (bipy) or 1,10-phenanthroline (phen), are able to bind to DNA in a partial intercalative interaction at its minor groove, showing DNA cleavage activity.[125,126] For these reasons, these complexes, known as *cassiopeinas*,[127,128] have been studied as antitumor agents and their cytotoxic properties against malignant cells have been proved on several tumour cell lines.[129–134] Unfortunately, the mechanism of action of cassiopeinas has yet to be understood: a variety of possibilities including proteasome inhibition, generation of reactive oxygen species and DNA damages have been invoked.[135–139]

Among these compounds, mixed copper(II) complexes containing 1,10-phenantroline and different amino acids attracted a lot of attention over the years. Therefore, many efforts have been dedicated to synthesize and characterize these systems.

Many scientific studies assume that the solid state structure, determined by means of X-ray crystallography, which very often show a distorted square pyramidal geometry with a water molecule apically bound, is maintained in solution .[129,131,140–143] In this project, CW-EPR spectra were recorded on some of these ternary copper(II) complexes in aqueous solution to verify if the geometry obtained at solid-state is really preserved.

8. CW-EPR characterization of Cu(II) complexes with ligands of biological interest

The two projects illustrated in this chapter were developed in the Department of Chemical Sciences at the University of Catania, under the supervision of Professor RAFFAELE PIETRO BONOMO. The shown results related are published.[11,144] Some figures of this chapter are adapted from the papers.

8.1 Design and scope of the projects

CW-EPR measurements at room (RT) and low temperature (LT) have been carried out on copper(II) complexes with some ligands of biological relevance to investigate their geometries in aqueous solution.

In the first project, binary and ternary copper(II) complexes with L-arginate (L-Arg) and L- or D-glutamate (L-/D-Glu) were characterized by means of CW-EPR spectroscopy to re-consider their coordination environment and their *cis/trans* ratio. Moreover, to support the spectroscopic data, Square Wave Voltammetry (SQV) measurements have been carried out on these systems in 0.1 M KNO_3 aqueous solution, as ground electrolyte, to check if *cis* and *trans* conformers have different formal redox potentials.

In the second project, CW-EPR spectroscopy was employed to study mixed copper(II) complexes with 1,10-phenanthroline (phen) and some amino acids to gain information about their peculiar molecular geometries and chemical behaviour in aqueous solution. The considered amino acids (AA) were the following: L-arginine (L-Arg), L-aspartic acid (L-Asp), L-histidine (L-His), L-glutamic acid (L-Glu), L-glutamine (L-Gln), L-leucine (L-Leu), L-lysine (L-Lys), L-methionine (L-Met), L-phenylalanine (L-Phe), L-tryptophan (L-Trp), L-tyrosine (L-Tyr) and L-valine (L-Val). SQV measurements were performed on these mixed complexes to support the spectroscopic data.

8.2 Materials and methods

8.2.1 Preparation of copper complexes in situ

All chemicals listed in paragraph §8.1 were purchased from Sigma-Aldrich and were used as received. Copper(II) complexes (charges were omitted for simplicity) were prepared for EPR experiments by addition of the appropriate volume of isotopically pure $^{63}Cu(NO_3)_2$ 50 mM to an aqueous solution containing the pertinent ligand. For binary complexes with L-Arg and L-/D-Glu, solutions of [L-Arg] = [L-Glu] = [D-Glu] = 10 mM were employed, with metal-to-ligand ratios ranging from 1:2 up to 1:10 to ensure the formation of bis complexes and with an absolute copper concentrations ranging from 1 to 3 mM. Ternary metal complexes with the same ligands were prepared in a metal to ligand ratio 1:5:5.

Ternary copper(II) complexes Cu:phen:AA were prepared with metal to ligand ratios ranging from 1:1:1 up to 1:1:1.1, respectively. A slight excess of AA was used to favour the ternary complex formation. The absolute copper concentrations ranged from 1 to 4 mM.

The final solution pH was adjusted by means of a Orion 9103SC combined glass microelectrode connected to a Orion Star A 211 pH meter in the range 6.5 - 7.5 for most of copper(II) complexes using concentrated NaOH or HNO_3 as required. The solutions were stirred for at least ten minutes in order to favour the copper binary or ternary species formation.

Only in the case of the complex [Cu(phen)(His)], the copper ternary complex was examined both in slight acidic (pH = 4.5 - 5.0) and neutral solutions (pH = 6.5 - 7.5).

8.2.2 CW-EPR experiments

CW-EPR experiments were performed at X-band frequencies (9.5 GHz) in a Bruker Elexsys E500 CW-EPR spectrometer equipped with a Super-X microwave bridge and a SHQE cavity.

The measurements at room temperature were recorded by means of a WG-812-H flat quartz cell. The isotropic magnetic parameters were evaluated from the average distances among the four peaks of the experimental spectra recorded in the 2nd derivative mode.

EPR spectra in frozen solution of copper(II) complexes were recorded in quartz tubes at 150 K cooling with liquid nitrogen and keeping the temperature by means of a ER4131VT variable temperature apparatus, also controlling all the experiments in the fluid aqueous solution at variable temperature. These latter were carried out by using a glass capillary inserted into a quartz tube. Methanol or glycerol up to 10 % was added to the copper(II) complex solutions in order to increase the resolution of the LT frozen solution spectra. The anisotropic magnetic parameters were obtained directly from the experimental EPR spectra, calculating them from the 2nd and the 3rd line to get rid of second order effects.[145] Perpendicular parameters were obtained exploiting the magnetic field of the extra–peak due to the angular anomaly.[97,98] CW-EPR simulations at low temperature were produced adopting a modified program from PILBROW.[146]

Instrumental settings employed to record frozen solution EPR spectra were the following: ν = 9.44-9.48 GHz; microwave power = 10 - 15 mW; modulation frequency = 100 kHz; modulation amplitude = 0.2-0.6 mT; time constant = 164 - 327 ms; sweep time 3 - 6 min; linear receiver gain = 10^4 - 10^5; number of scans 1-3. Instrumental settings of RT EPR spectra were the same, except for the value of microwave frequency which was in the range 9.70 - 9.80 GHz and microwave power up to 40 mW. Sometimes more than 10 scans were acquired to increase the signal to noise ratio.

8.2.3 Voltammetric experiments

Square wave voltammetry (SWV) experiments were carried out on Cu(II) complexes in 0.1 M KNO_3 aqueous solution in the same copper and ligand concentrations described in section §8.2.1. The measurements were performed at 25°C in a Metrohm glass cell with a three electrodes assembly by Metrohm: a working glassy carbon electrode (2 mm diameter), a platinum rod as auxiliary electrode and an Ag / AgCl reference electrode. The voltammograms of binary and ternary copper(II) complexes with Arg and Glu were recorded by means of a Metrohm Autolab PGSTAT 128N potentiostat – galvanostat. The voltammograms of ternary copper(II) complexes Cu:phen:AA were acquired by means of Metrohm Autolab PGSTAT 204 potentiostat - galvanostat. All complex solutions were degassed by using ultrapure nitrogen or argon gasses.

Electrochemical measurements were acquired for binary and ternary copper(II) complexes with Arg and Glu, in the region from +0.500 to -0.700 V, setting a frequency of 15 Hz. In the case of ternary copper(II) complexes Cu:phen:AA, the potential was swept in a range from -0.100 to -0.900 V, setting a frequency of 25 Hz. Pulses of 25 – 35 mV were applied, avoiding more intense pulses which can cause broadening of the current peak. All potentials are referred to Ag / AgCl reference electrode, +0.215 V vs. Normal Hydrogen Electrode (NHE). The Ag / AgCl electrode potential was checked by using methylviologen redox couple (MV^{2+}/MV^{+}) -0.446 V vs. NHE.[147]

Cyclic voltammetry (CV) measurements with a sweep rate of 50 mV s^{-1} were run in the same range of potentials adopted for SWV experiments.

8.3 Results and Discussions on characterization of binary and ternary Cu(II) complexes with Arg and Glu

As introduced in chapter §7, copper(II) complexes with L- or D-aminoacidate ligands show their side chains on the same side, when the *trans* conformation is obtained, viceversa when the *cis* forms, as shown in figure 7.1.[121] It has long been thought that the *trans* conformer has a stronger ligand field than the *cis*.[148] Recent experimental and theoretical data predict that this is true only in the gas phase, while the stability of two conformers reverses in aqueous solution due to the interactions with the water molecules.[149,150] It is also well-known that lower temperatures favours the thermodynamically more stable complex species.[151]

8.3.1 RT CW-EPR spectra of binary and ternary Cu(II) complexes

As discussed in section §1.1.2, when two nitrogen atoms are coordinated to a copper(II) ion, a pattern showing five superhyperfine (shf) lines with intensity distribution 1:2:3:2:1 might be reasonably expected form the Tartaglia's triangle due to the interactions between the electron and the nuclear spins of nitrogen donor atoms. The fact that the two nitrogen atoms could be in a *cis* or in a *trans* conformation in the copper(II) coordination plane do not have a great influence on the magnetic parameters of the complexes. The shf constants due to the interactions with the two nitrogen nuclei have approximately similar values.

In the case of aminoacidate ligands, the interactions between the side chains might stabilize one conformer over the other.[121,124,148] Experimental CW-EPR spectra of binary and ternary copper(II) complexes [Cu(L-Glu)$_2$], [Cu(L-Arg)$_2$], [Cu(L-Arg)(L-Glu)] and [Cu(L-Arg)(D-Glu)] recorded at pH =7.5 in 2nd derivative mode at 275 K and 305 K are illustrated in figure 8.1.

These CW-spectra show four hyperfine lines due to the interactions between the electron spin and nuclear spin of Cu(II) ion $\left(I = \frac{3}{2}\right)$. These hyperfine lines do not show the same intensity and the same linewidth because the tumbling motions of the system are not so fast to average out completely the molecular anisotropies.

The shf lines are better resolved on the hyperfine line at the highest magnetic field because it presents a favourable linewidth which depends on

the nuclear quantum number of the EPR transition. These shf lines are characterized by a peculiar feature: surprisingly, a complicated pattern with six or seven shf lines is visible. It can only come from the superposition of the five shf lines which belong to the *cis* conformer with those of *trans* conformer.

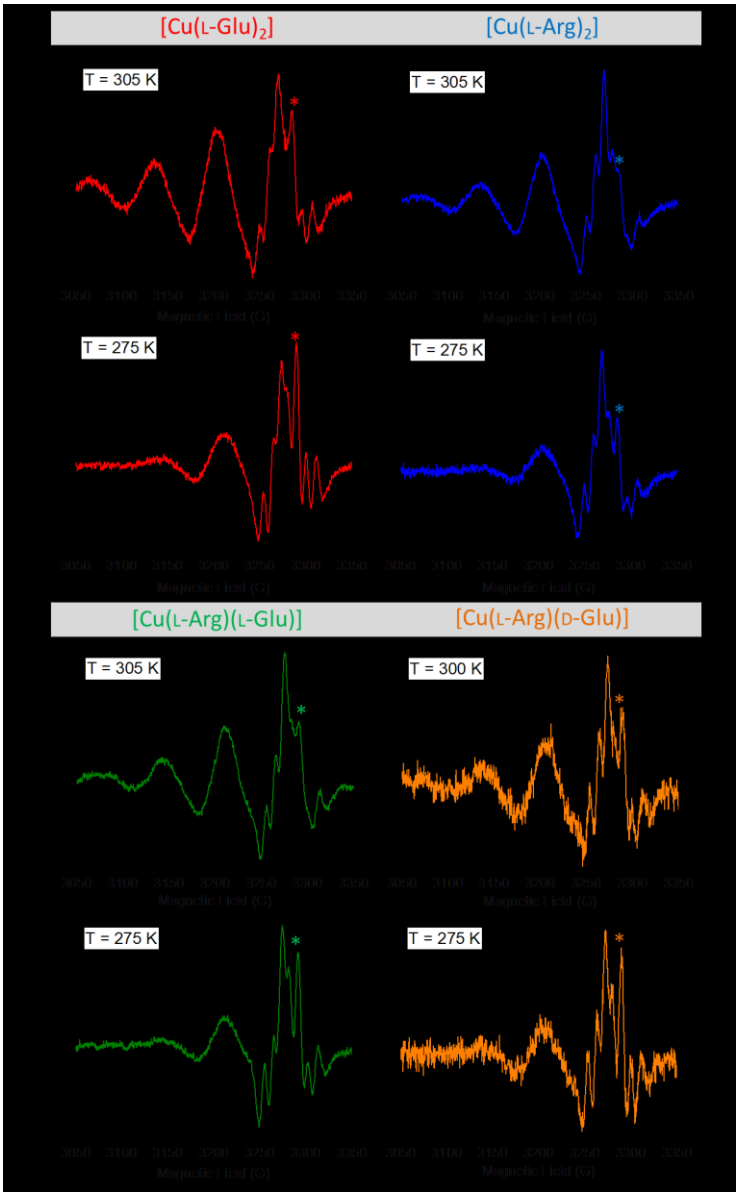

Figure 8.1. 2nd derivative CW-EPR spectra recorded at 275K and 305 or 300K on [Cu(L-Glu)$_2$] (red), [Cu(L-Arg)$_2$] (blue), [Cu(L-Arg)(L-Glu)] (green) and [Cu(L-Arg)(D-Glu)] (orange). The coloured asterisk indicates a shf line which reduces its intensity on going from 275 K to 305 / 300 K.

Looking at these CW-EPR spectra the two conformers have probably slightly different magnetic parameters resulting in this complicated pattern.

CW-EPR spectra of ternary complexes [Cu(L-Arg)(L-Glu)] and [Cu(L-Arg)(D-Glu)], shown on the bottom figure 8.1, were achieved calculating the difference between the experimental CW-EPR spectra of ternary complexes with the CW-EPR spectra of the binary copper(II) complexes [Cu(L-Glu)$_2$] and [Cu(L-Arg)$_2$]. A weight of 25% was assigned to each binary species according with the species distribution diagrams reported in figure 8.2. This diagram was obtained by means of Hyperquad simulation and speciation (HySS) program,[152] adopting a metal to ligands ratio of 1:5:5. Stability constants and logβ values of binary and ternary copper(II) complexes were taken from the literature.[153]

CW-EPR spectrum of [Cu(L-Arg)(D-Glu)] at higher temperature was recorded at 300 K instead of 305 K since the signal to noise ratio becomes worse with increasing temperature.

Looking more in details at these experimental CW-EPR spectra, it is possible to note that the intensity of the shf lines is temperature-dependent. Figure 8.1 reports only CW-EPR spectra recorded at 275 K and 305 K, but, a series of CW-EPR experiments (not shown) were run for each complex species in the whole range of temperatures from 275 K to 305 K with increments of 5.0 ± 0.5K degrees. These experiments have revealed a modifications of shf lines intensity and, in particular, an evident gradual decreasing of the shf line intensity marked with the asterisk in figure 8.1.

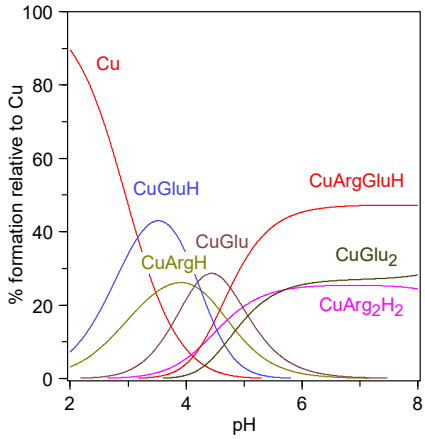

Figure 8.2. Species distribution diagram in the case of the formation of ternary [Cu(L-Arg)(L-Glu)] complex: [Cu] = 3 mM, [L-Glu] = [L-Arg]= 15 mM. The distribution diagram for the formation of [Cu(L-Arg)(D-Glu)] is analogue.

Over 305 K or above 275 K the linewidth of the fourth copper hyperfine line was not so favourable to clearly resolve the superhyperfine interactions with nitrogen donor atoms.

This behaviour can be explained considering that the temperature has an influence on the equilibrium between *cis* and *trans* conformers. In particular, as introduced at the beginning of this paragraph, the *cis* conformer, which has a slightly higher thermodynamic stability in aqueous solution,[149,150] is more stabilized at lower temperature, so that at 275 K there is a larger population of *cis* over the *trans* conformers. The *cis/trans* ratio changes towards the *trans* conformer moving from low to higher temperatures. There is no shift in the field of each shf line (always within 1 G), but experimentally it is clear their modifications in intensity due to the change in the relative populations.

Given that, it is possible to assign in the experimental CW-EPR spectra the shf lines which belong to the *cis* conformer (those at higher magnetic field superimposed on the fourth copper transition that decrease with the temperature) and those of the *trans* (at lower magnetic field). As a result, it is possible to conclude that the two conformers have almost the same g_{iso} but the *cis* conformer has a copper isotropic hyperfine constant a_{iso} slightly higher than the *trans*. The isotropic magnetic parameters extracted from the experimental CW-EPR spectra are reported in table 8.1.

Table 8.1. Isotropic spin Hamiltonian parameters of bis and ternary copper(II) complexes with L-Arg and L- or D-Glu at pH = 7.5, extracted from RT CW-EPR solution spectra. Estimated experimental errors on the last digit are reported in brackets.

Complex		g_{iso}	a_{iso} (10^{-4}cm^{-1})	a^{N}_{iso} (10^{-4}cm^{-1})
[Cu(L-Glu)$_2$]	*cis*	2.122(3)	71(3)	11(1)
	trans	2.124(3)	65(3)	10(1)
[Cu(L-Arg)$_2$]	*cis*	2.124(3)	72(3)	11(1)
	trans	2.128(3)	66(3)	9(1)
[Cu(L-Arg)(L-Glu)]	*cis*	2.126(3)	72(3)	10(1)
	trans	2.128(3)	66(3)	11(1)
[Cu(L-Arg)(D-Glu)]	*cis*	2.122(3)	71(3)	9(1)
	trans	2.124(3)	65(3)	11(1)

The two conformers present essentially the same isotropic shf coupling constants a_{iso}^{N}, considering an experimental error of ± 1x10^{-4} cm^{-1}. All these parameters fit well with those achieved by the simulations of GOODMAN and co-workers.[154]

A series of CW-EPR spectra in the same range of temperatures was recorded also on binary copper(II) complexes with a racemic mixtures of L-/D-Arg and L-/D-Glu ligands to check if the different stereochemistry might influence the shf patterns and the magnetic parameters. However, the same behaviour was observed even in the presence of the mesocomplex species with the DD- configurations: the distribution between *cis* and *trans* conformers was not altered.

Furthermore, looking at RT CW-EPR spectra of binary and ternary copper(II) complexes of figure 8.1, it is possible to estimate the percentages of each conformer in aqueous solution from the ratio of the central shf line assigned to the *cis* and to the *trans* conformers. These percentages are reported in table 8.2. and suggest a different behaviour of these copper(II) complexes in aqueous solution with the temperature.

First, comparing the two binary copper(II) complexes, at 275 K the *cis* conformer is dominant in solution for [Cu(L-Glu)$_2$]; on the contrary, for [Cu(L-Arg)$_2$], the *trans* is the most abundant species. Moving to higher temperatures, both copper(II) complexes evolve towards the *trans* conformer but with a different trend: in the case of [Cu(L-Arg)$_2$], at 305K the *trans* conformer overcomes the 80% of formation; *trans* [Cu(L-Glu)$_2$] stops around 60% of formation. In order to explain this different behaviour, an extra-stability contribution due to the electrostatic interactions between the charged groups of the side chains could be invoked.

Table 8.2. Estimated percentages of *cis* and *trans* conformers obtained from the ratio of the areas between the assigned central shf lines to the *cis* and *trans* conformers. Estimated errors are of the order of 10%. The data marked with an asterisk were achieved at 300K.

Complex	**275 K**		**305 K**	
	cis	***trans***	***cis***	***trans***
[Cu(L-Glu)$_2$]	76 %	24 %	36 %	64 %
[Cu(L-Arg)$_2$]	41 %	59 %	16 %	84 %
[Cu(L-Arg)(L-Glu)]	56 %	44 %	16 %	84 %
[Cu(L-Arg)(D-Glu)]	55 %	45 %	40 %*	60 %*

In both binary copper(II) complexes, electrostatic repulsions occur between the two positive guanidinium groups of Arg or the two negative carboxylate groups of Glu. These electrostatic repulsions are minimized in the *cis* conformer where the two side chains are on the opposite sides of the CuN_2O_2 coordination plane, as shown in the scheme of figure 8.3.

Additionally, weak apical interactions of glutamate negative charges with the hydrogen atoms of water apical molecules could occur, thus further stabilizing the *cis* conformer. In the case of [Cu(L-Arg)$_2$], the positive guanidinium groups interact much less with the oxygens of these water molecules because oxygens are involved in the copper(II) coordination sphere. These observations would explain the different population among *cis* and *trans* conformers of binary copper(II) complexes with these aminoacidate ligands.

Now the comparison of *cis/trans* ratio in the ternary copper(II) complexes, whose percentages of formation are reported in table 8.2, suggest that at 275K this ratio is the same for both systems and close to unity.

Increasing the temperature from 275K to 305K the population of *trans* conformer grows up at the expense of the *cis* conformer but the latter is more abundant for [Cu(L-Arg)(D-Glu)] than for [Cu(L-Arg)(L-Glu)]. This fact could be explained considering that in the *cis* [Cu(L-Arg)(L-Glu)] the side chains are on the opposite side of the CuN_2O_2 coordination plane. On the contrary, in the *cis* [Cu(L-Arg)(D-Glu)], the side chains of both ligands are on the same side of the CuN_2O_2 coordination plane due to the different stereochemistry of Glu, as shown in the scheme of figure 8.3. An attractive electrostatic interaction between the two opposite charged guanidinium and carboxylate groups in *cis* [Cu(L-Arg)(D-Glu)] probably stabilizes much more this conformer over the *trans* in comparison with [Cu(L-Arg)(L-Glu)].

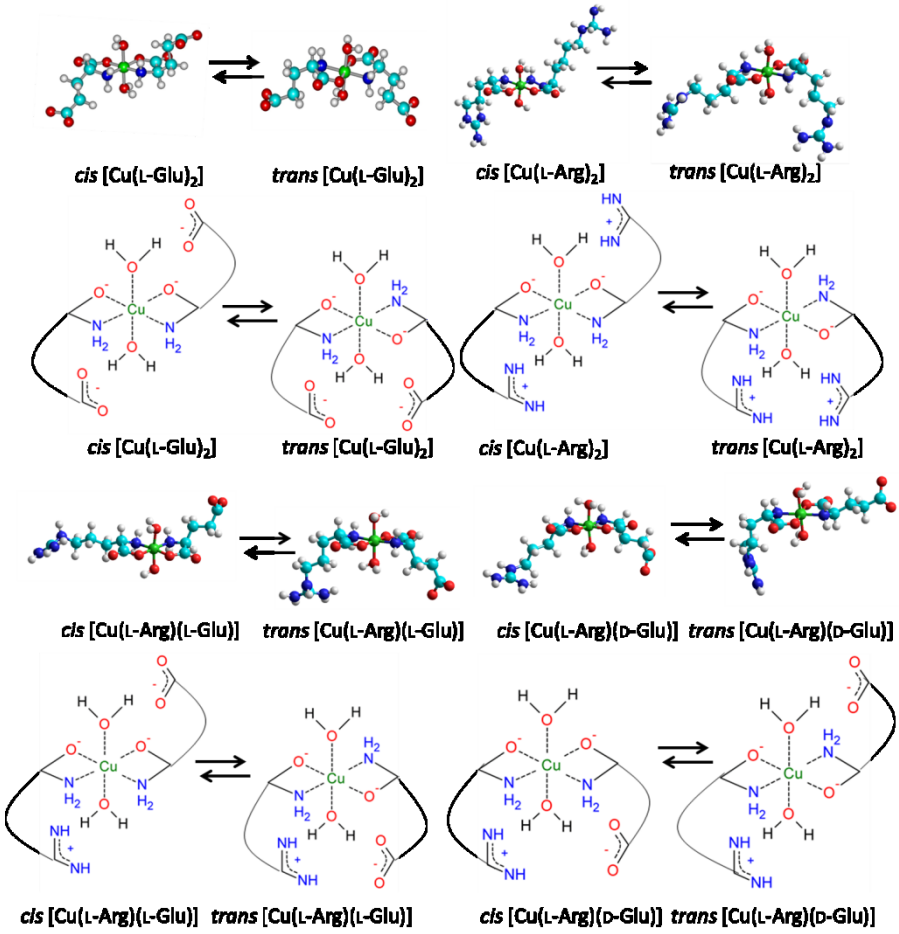

Figure 8.3. Scheme of the equilibria between *cis* and *trans* conformers of binary and ternary copper(II) complexes with L-Arg and L- or D-Glu.

8.3.2 LT CW-EPR spectra of binary and ternary copper(II) complexes

Experimental CW-EPR spectra of binary and ternary complexes [Cu(L-Glu)$_2$], [Cu(L-Arg)$_2$], [Cu(L-Arg)(L-Glu)] and [Cu(L-Arg)(D-Glu)] recorded in frozen solutions at 150 K are shown in figure 8.4.

In all cases, it is possible to observe clearly three hyperfine lines in the parallel region of the spectra; the forth overlaps those of the perpendicular region which are not resolved. An intense extra-peak, due to an angular anomaly, appears after the perpendicular region of the spectrum.[97]

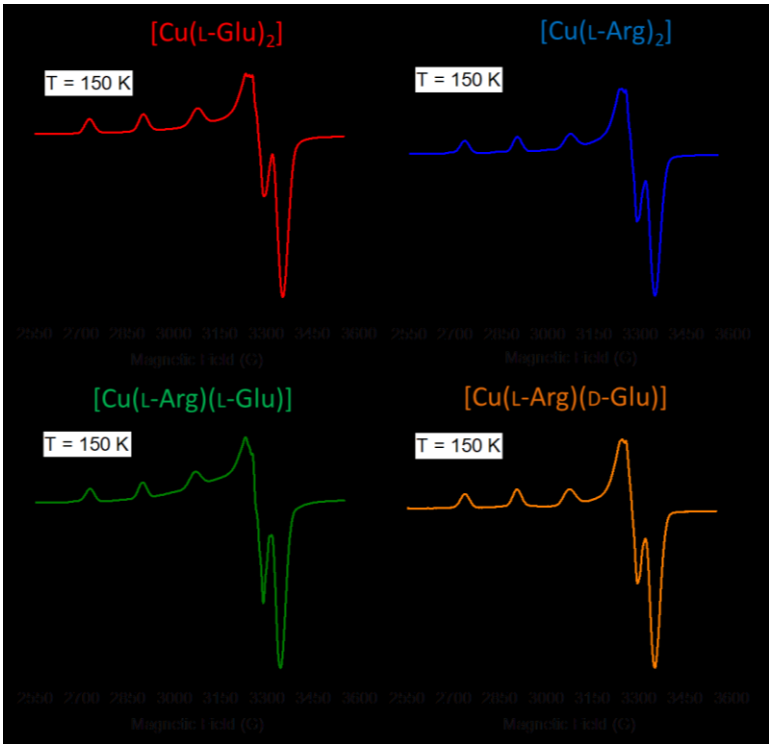

Figure 8.4. Experimental CW-EPR spectra of binary and ternary copper(II) complexes recorded at 150K: [Cu(L-Glu)$_2$] (red), [Cu(L-Arg)$_2$] (blue), [Cu(L-Arg)(L-Glu)] (green) and [Cu(L-Arg)(D-Glu)] (orange).

Only one copper(II) species is visible in the LT CW-EPR spectra; therefore, one of the two conformers is more stabilized at low temperatures. For the reasons discussed above, this copper(II) species is ascribable to the *cis* conformer.

The anisotropic magnetic parameters extracted from the experimental CW-EPR spectra are summarized in table 8.3. and can give more detailed information on the copper(II) complex geometries, as discussed in chapter §6. In particular, all these frozen solution EPR spectra are characterized by $g_{||} > g_{\perp} > 2.040$, indicating that all these copper(II) complexes have a copper $d_{x^2-y^2}$ or d_{xy} ground state, typical for octahedral, square-base pyramidal or square planar stereochemistries.[155] Since the absolute values of hyperfine constants are not so large to consider square planar geometries, or so low to take into account square-based pyramids, these data confirm that the tetragonally elongated octahedron is the preferential geometry with two oxygen atoms from water molecules as apical ligands.[155]

Table 8.3. Anisotropic spin Hamiltonian parameters of bis and ternary copper(II) complexes with L-/D-Glu or L-Arg at pH = 7.5, extracted from CW-EPR frozen solution spectra. Estimated experimental errors on the last digit are reported in brackets. Perpendicular parameters have been estimated making use of the extra-peak.[98]

Complex	$g_{\|\|}$	$A_{\|\|}$ (10^{-4} cm^{-1})	$g_{\perp}$	$A_{\perp}$ (10^{-4} cm^{-1})
[Cu(L-Glu)$_2$]	2.258(2)	181(2)	2.051(4)	16(4)
[Cu(L-Arg)$_2$]	2.257(2)	181(2)	2.049(4)	15(4)
[Cu(L-Arg)(L-Glu)]	2.265(3)	181(2)	2.057(4)	17(4)
[Cu(L-Arg)(D-Glu)]	2.260(3)	179(2)	2.051(4)	17(4)

Looking at the parameters of table 8.3., the differences among g and A value of the copper(II) complexes are negligible. However, some slight differences in the g values exceeding the experimental errors can be appreciated between the ternary complexes [Cu(L-Glu)(L-Arg)] and [Cu(L-Arg)(D-Glu)] and among the ternary and binary copper(II) species. These changes could be attributed to a different influence of the two charged side chains on the copper(II) polyhedron.

From the anisotropic magnetic parameters reported in table 8.3. it is possible to estimate the isotropic g and a value according to equation (11), introduced in chapter §1: $g_{iso} = \frac{1}{3}(g_{\|} + 2g_{\perp})$ and $a_{iso} = \frac{1}{3}(A_{\|} + 2A_{\perp})$. A comparison among the isotropic magnetic parameters extracted from the experimental CW-EPR spectra at RT and those calculated from the LT CW-EPR spectra is reported in table 8.4.

As one can see, the isotropic g and a values of the *cis* conformer obtained at RT fit well with the g_{iso} and a_{iso} values calculated from the frozen solution EPR spectra. This similarity further confirms that the *cis* conformer is thermodynamically more stable than the *trans* conformer in aqueous solution; therefore, it is stabilized at low temperatures. The *cis/trans* equilibrium evolves towards the *trans* conformer moving from low to high temperatures.

Table 8.4. Comparison among the isotropic spin Hamiltonian parameters reported in table 8.1. and those calculated form the anisotropic magnetic parameters of table 8.3 according to equation (11). Estimated experimental errors on the last digit are reported between brackets.

Complex		g_{iso}	g_{iso} *calcd*	a_{iso} (10^{-4} cm^{-1})	a_{iso} *calcd* (10^{-4} cm^{-1})	a^{N}_{iso} (10^{-4} cm^{-1})
[Cu(L-Glu)$_2$]	*cis*	2.122(3)	2.119(3)	71(3)	71(3)	11(1)
	trans	2.124(3)		65(3)		10(1)
[Cu(L-Arg)$_2$]	*cis*	2.124(3)	2.119(3)	72(3)	70(3)	11(1)
	trans	2.128(3)		66(3)		9(1)
[Cu(L-Arg)(L-Glu)]	*cis*	2.126(3)	2.126(3)	72(3)	72(3)	10(1)
	trans	2.128(3)		66(3)		11(1)
[Cu(L-Arg)(D-Glu)]	*cis*	2.122(3)	2.121(3)	71(3)	71(3)	9(1)
	trans	2.124(3)		65(3)		11(1)

8.3.3 Voltammetric results on Copper(II) bis and ternary complexes

Carrying out an electrochemical reduction of binary and ternary copper(II) complexes, a mono electronic step is detected, whose re-oxidation generally is not reversible and leads to decomposition products.[156] Geometrical constraints of copper complexes make difficult the re-oxidation of copper(I) complex to the previous copper(II) species.[157] SWV voltammograms on solutions of binary and ternary copper(II) complexes, prepared in 0.1. M KNO_3 solution, as ground electrolyte, are shown in figure 8.5. These measurements reveal an asymmetric peak associated with the Cu(II) → Cu(I) reduction process. This effect could be explained considering that the two *cis* and *trans* conformers have a slight different formal redox potential that can be calculated by deconvolution.

In particular, the experimental SWV peaks of binary copper(II) complexes [Cu(L-Glu)$_2$] and [Cu(L-Arg)$_2$] can be fitted by summing two Gaussian curves with slight different centres and widths. The two curves refer to the reduction peak of each single conformer. In the case of the ternary copper(II) complexes, [Cu(L-Arg)(L-Glu)] and [Cu(L-Arg)(D-Glu)], the experimental SWV peaks can be fitted by summing six Gaussian curves, according with the species distribution diagram of figure 8.2: four curves refer to the two conformers of each bis aminoacidate copper(II) species and

have a weight of 25 %. The other two curves refer to the ternary complex conformers.

The formal redox potentials extracted from this deconvolution process are summarized in table 8.5. It is possible to note that copper(II) binary complex with Arg presents a more negative formal redox potential than the analogous complex with Glu. This difference could be ascribable to a greater stability constant of copper(II) bis complex associated with Arg.[153] The slightly larger formal redox potentials of the copper(II) ternary complexes reflect the larger stability of the ternary over the binary species.

These voltammetric data support the EPR measurements and confirm the existence of an equilibrium in aqueous solution between *cis* and *trans* conformer for these binary and ternary copper(II) complexes with Arg and Glu ligands.

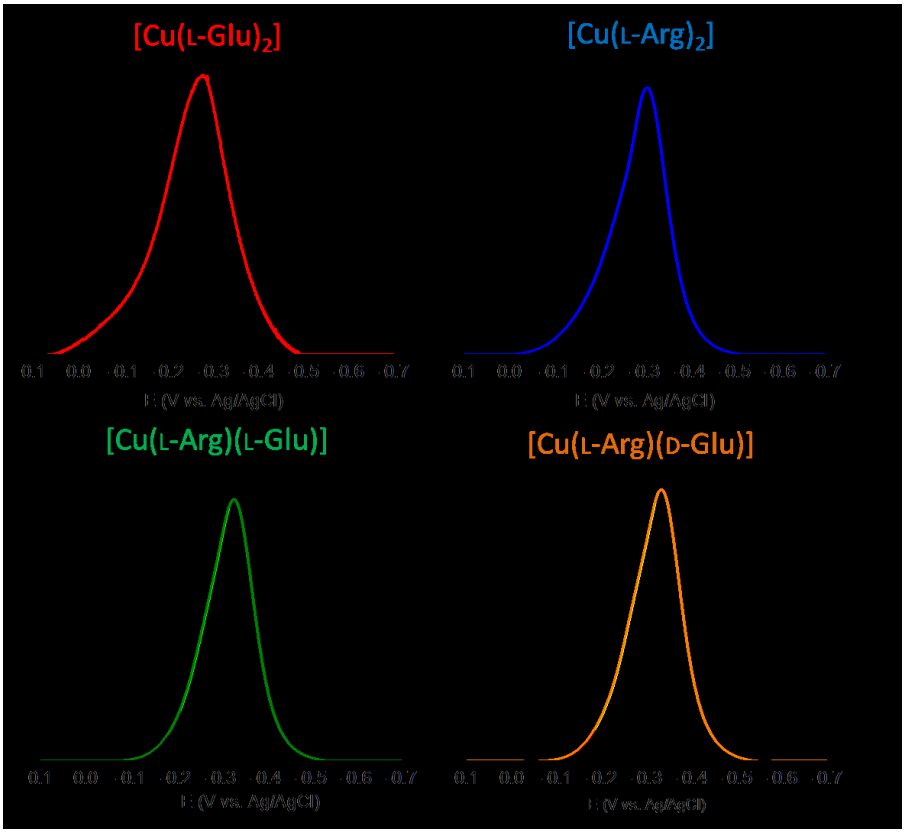

Figure 8.5. Normalized experimental Square Wave Voltammograms of [Cu(L-Glu)$_2$] (red), [Cu(L-Arg)$_2$] (blue), [Cu(L-Arg)(L-Glu)] (green) and [Cu(L-Arg)(D-Glu)] (orange) in KNO_3 0.1 M solution recorded at 25°C adopting 15 Hz frequency and 25 - 35 mV applied pulse.

Table 8.5. Formal redox potentials at 295K, obtained in aqueous solutions with 0.1 M KNO_3 as ground electrolyte. Errors in the extracted values are estimated to be about ± 0.010 V. The more negative formal redox potential is assigned to the *cis* conformer.

Complex	Ep, V, Ag/AgCl		ΔEp
	cis	***trans***	
[Cu(L-Glu)$_2$]	-0.273	-0.248	0.025
[Cu(L-Arg)$_2$]	-0.302	-0.278	0.024
[Cu(L-Arg)(L-Glu)]	-0.324	-0.301	0.023
[Cu(L-Arg)(D-Glu)]	-0.329	-0.305	0.024

8.4 Results and Discussions on characterization of copper(II) complexes with 1,10-phenantroline and different amino acids

8.4.1 Species distribution diagrams

Before performing spectroscopical and voltammetric experiments in aqueous solution, in the case of ternary copper(II) complexes, it is important to understand which species is expected at the experimental pH values.

Several pHmetric studies have shown that at pH higher than 6 the copper(II) ternary complexes with phen and AA is the most abundant species with 80% of formation, while other minor complex species reach less than 10% of formation.[123,158–163] This behaviour is the same for all ternary copper(II) complexes examined in this paragraph except for the complex [Cu(phen)(L-His)]. It is well-known that His coordinates copper(II) ions in two different ways: at acidic pH values the imidazole group is protonated and L-His involves the amino and carboxylate groups to coordinate the metal centre (glycine-like mode). Around neutral pH values the imidazole group deprotonates and L-His coordinates copper(II) ions in a histamine-like mode: the oxygen atom of the carboxylate group is still involved in the coordination sphere but an equilibrium between an equatorial or an apical position exists due to strong distortions of the coordination geometry at this pH values. Moreover, the deprotonated nitrogen of the heterocyclic side chain can take part to copper coordination.[164] This two coordination modes are shown in the scheme of figure 8.6 for the expected ternary complex [Cu(phen)(L-His)].

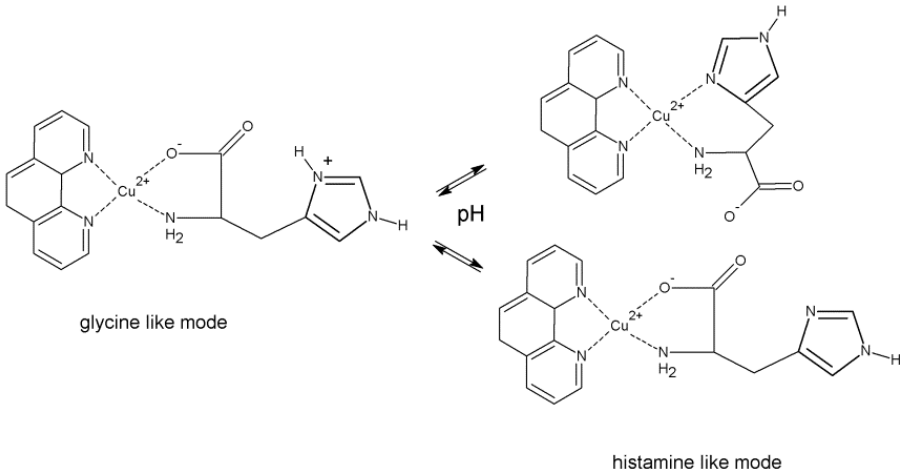

Figure 8.6. Scheme of ternary [Cu(phen)(L-His)] complex as a function of pH.

This behaviour of His is confirmed also by the species distribution diagram obtained with HySS program.[152] Figure 8.7 compares the species distribution diagram of [Cu(phen)(L-Leu)], calculated based on the logβ values reported in the studies of TÜRKEL and co-workers,[159] with that one of [Cu(phen)(L-His)], achieved with the logβ values from the study of PATEL and co-workers.[158] The charges are omitted for simplicity.

As it is possible to see, at the pH value near the neutrality, the formation of ternary species in both cases reaches more than 80% of the total copper. Around pH = 5 the two systems behave differently: in the case of [Cu(phen)(L-Leu)] there is an equilibrium between the binary [Cu(phen)] and the ternary [Cu(phen)(L-Leu)] species that form roughly with the same percentages. In the case of L-His, this equilibrium is between the binary [Cu(phen)] and the ternary [Cu(phen)(L-HisH)] with the protonated imidazole nitrogen. The deprotonated ternary complex [Cu(phen)(L-His)] forms with a percentage below 10% at this pH value. There are also some minor species below 5% of formation but they generally do not contribute to the overall EPR spectra because they are relegated to instrumental noise.

In the next sections, EPR and voltammetric measurements performed in aqueous solution on these ternary copper(II) complexes are presented in order to characterize their geometries and check if the structural crystallographic data are confirmed on going to the aqueous solution state.

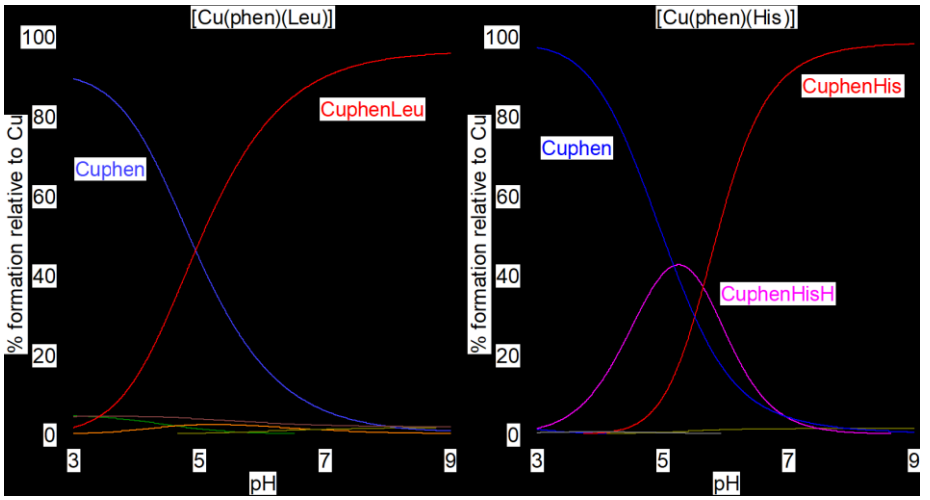

Figure 8.7. Species distribution diagrams of [Cu(phen)(L-Leu)] (left) and [Cu(phen)(L-His)] (right). Copper(II) complexes were considered with the following concentrations: [Cu] = [phen] = [L-Leu] or [L-His] = 1 mM.

8.4.2 CW-EPR spectra at room and low temperatures

RT and LT CW-EPR spectra of all ternary copper(II) complexes with phen and AA are discussed except for the case of histidine, whose CW-EPR spectra will be illustrated in the section §8.4.5.

In the case of [Cu(phen)(AA)] ternary complexes examined in this section, a tetragonally elongated octahedron geometry, like that of the other copper(II) complexes of the previous paragraph, is expected.

The coordination plane around the metal centre should be formed, in this case, by the two nitrogen atoms coming from phen, a third nitrogen from the amino group of the aminoacidate ligand and the oxygen atom of the carboxylate groups. When three quasi equivalent nitrogen atoms are coordinated to copper(II) ions a pattern of seven shf lines (with intensity distribution 1:3:6:7:6:3:1 from the Tartaglia's triangle) might be expected, as discussed in section §1.1.2.

Figure 8.8 shows, as example, the RT CW-EPR spectrum of [Cu(phen)(L-Leu)] recorded in the 2nd derivative mode, in aqueous solution and at pH around the neutrality. All RT CW-EPR spectra of [Cu(phen)(AA)] ternary complexes examined in this section present the same features: four hyperfine lines are visible due to the interaction between the electron spin and nuclear spin of Cu(II) ion $\left(I = \frac{3}{2}\right)$.

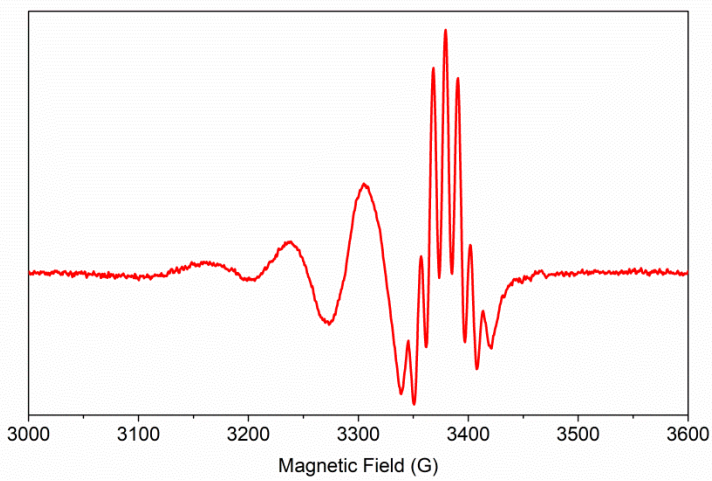

Figure 8.8. 2nd derivative mode RT CW-EPR spectrum of [Cu(phen)(L-Leu)] in aqueous solution at pH around 7.

Then, the hyperfine line at the highest magnetic field is characterized by seven clearly visible shf lines due to the interaction of copper(II) free electron with the nuclei of three nitrogen donor atoms in its equatorial coordination plane.

The isotropic magnetic parameters extracted from all RT CW-EPR spectra are basically the same with negligible differences, always within the experimental error: g_{iso}= 2.121 ± 0.002, a_{iso}= 70 ± 2x10^{-4} cm^{-1}, a_{iso}^{N}= 10 ± 1x10^{-4} cm^{-1}.

These data are confirmed by the frozen solution CW-EPR spectra of these ternary complexes recorded at 150 K, in fact all of them presents only one signal coming from the copper(II) ternary complex species, [Cu(phen)(AA)]$^{+}$.

Figure 8.9 shows, as example, LT CW-EPR spectrum of the ternary copper(II) complex [Cu(phen)(L-Tyr)] recorded at 150 K. It presents three visible hyperfine EPR lines in the parallel region of the spectrum; the forth one overlaps with the perpendicular region which is not resolved. An intense extra-peak, due to an angular anomaly, appears after the perpendicular region of the spectrum.[98] The inset of figure 8.9 shows the well resolved $A_{\perp}^{N}$ superhyperfine coupling constant on the parallel lowest field line. As discussed in paragraph §6.2, according to the different molecular frames of the ligands and of the metal centre, the perpendicular superhyperfine constant coupling can be measured in the hyperfine parallel part of frozen solution CW-EPR spectrum.

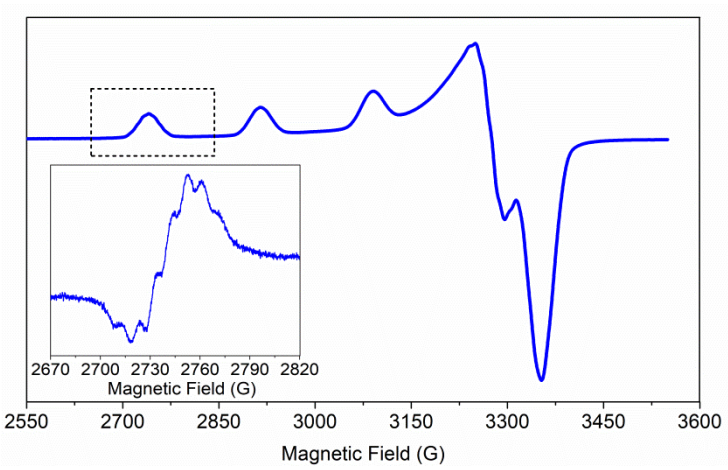

Figure 8.9. 2nd derivative mode LT CW-EPR spectrum of [Cu(phen)(L-Tyr)] in aqueous solution at pH = 7. The inset contains an enlarged view of the seven shf lines superimposed on the lowest field feature.

All these data taken together confirm that, in these experimental conditions, the [Cu(phen)(AA)] ternary complexes investigated in this section have three nitrogen donor atoms on the equatorial coordination plane around copper(II) ions.

The anisotropic magnetic parameters extracted from each LT CW-EPR spectrum are reported in table 8.6., together with the isotropic magnetic parameter obtained from RT CW-EPR spectra, for all complexes. The superhyperfine coupling constant $A_{\perp}^{N}$ was clearly resolved only for the copper(II) ternary complex with L-Tyr. In all the other ternary complexes the parallel nitrogen shf structure was not clearly resolved. All these parameters do not present remarkable differences.

Like the copper(II) complexes of the previous paragraph all the frozen solution EPR spectra are characterized by $g_{||} > g_{\perp} > 2.040$, indicating that [Cu(phen)(AA)] ternary complexes have a copper $d_{x^2-y^2}$ or d_{xy} ground state, typical for octahedral, square-base pyramidal or square planar stereochemistries.[155] Since the absolute values of hyperfine constants are not so large to consider square planar geometries, or so low to take into account square-based pyramids, these data confirm that the tetragonally elongated octahedron is the preferential geometry with two oxygen atoms from water molecules as apical ligands.[155]

Table 8.6. Spin Hamiltonian parameters of ternary copper(II) complexes with 1,10-phenanthroline and different aminoacidates at pH around 7, extracted from frozen solution and liquid solution CW-EPR spectra. Estimated experimental errors on the last digit are reported in brackets. All the hyperfine and superhyperfine coupling constants are expressed in 10^{-4} cm^{-1} units.

Complex	g_{iso}	a_{iso}	$g_{\|\|}$	$A_{\|\|}$	$g_{\perp}$	$A_{\perp}$	a_{iso}^{N}	$A_{\perp}^{N}$	$A_{\|\|}^{N}$
Cu(phen)(L-Arg)	2.121(2)	71(2)	2.240(3)	188(3)	2.052(5)	12(5)	10(1)	-	11(1)
Cu(phen)(L-Asp	2.122(2)	72(2)	2.242(3)	187(3)	2.053(5)	10(5)	10(1)	-	11(1)
Cu(phen)(L-Glu)	2.119(2)	70(2)	2.242(3)	186(3)	2.050(5)	11(5)	10(1)	-	12(1)
Cu(phen)(L-Gln)	2.122(2)	71(2)	2.241(3)	186(3)	2.048(5)	13(5)	11(1)	-	12(1)
Cu(phen)(L-Leu)	2.122(2)	71(2)	2.241(3)	187(3)	2.049(5)	11(5)	10(1)	-	11(1)
Cu(phen)(L-Lys)	2.119(2)	70(2)	2.240(3)	187(3)	2.051(5)	14(5)	10(1)	-	11(1)
Cu(phen)(L-Met)	2.122(2)	72(2)	2.241(3)	186(3)	2.049(5)	11(5)	10(1)		11(1)
Cu(phen)(L-Phe)	2.121(2)	70(2)	2.238(3)	186(3)	2.053(5)	10(5)	10(1)	-	11(1)
Cu(phen)(L-Trp)	2.122(2)	71(2)	2.237(3)	188(3)	2.054(5)	11(5)	10(1)	-	11(1)
Cu(phen)(L-Tyr)	2.121(2)	71(2)	2.241(3)	184(3)	2.050(5)	14(5)	10(1)	10(1)	11(1)
Cu(phen)(L-Val)	2.119(2)	70(2)	2.240(3)	188(3)	2.051(5)	14(5)	10(1)	-	11(1)

8.4.3 Voltammetric measurements

Like the copper(II) complexes with Arg and Glu described in the paragraph §8.3, the electrochemical reduction from Cu(II) to Cu(I) oxidation state of ternary copper(II) complexes [Cu(phen)(AA)] presents a mono electronic step, whose re-oxidation generally is not reversible and leads to decomposition products.[156] Geometrical constraints of copper complexes make difficult the re-oxidation of copper(I) complex to the previous copper(II) species.[157]

Figure 8.10 shows the SWV peaks recorded on solutions of [Cu(phen)(L-Asp)], which has an aromatic residue, and [Cu(phen)(L-Leu)] with an aliphatic residues. The formal redox potentials extracted for some ternary copper(II) complexes [Cu(phen)(AA)] are summarized in the table 8.7.

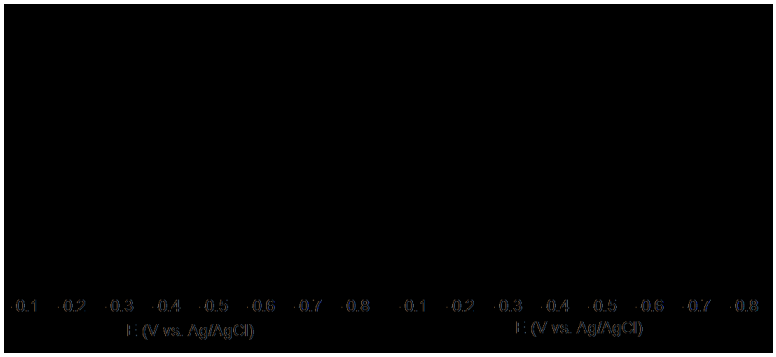

Figure 8.10. Square Wave voltammograms of the copper ternary species [Cu(phen)(L-Asp)] (left) and [Cu(phen)(L-Leu)] (right) recorded in 0.1 M KNO_3 solution, as ground electrolyte at neutral pH.

Table 8.7. SWV formal redox potentials of some ternary copper(II) complexes with 1,10-phenanthroline and aminoacidates at pH around 7, in aqueous solution by using KNO_3 0.1 M as ground electrolyte. PWHH is the abbreviation of peak width at half height. Presumed errors are reported in brackets.

Complex	***pH***	***Ep, mV*** *(12 mV)*	***PWHH, mV*** *(10mV)*
Cu(phen)(L-Arg)	7.2	-363	200
Cu(phen)(L-Lys)	7.4	-354	170
Cu(phen)(L-Asp)	7.2	-503	110
Cu(phen)(L-Leu)	7.0	-510	93
Cu(phen)(L-Phe)	7.2	-488	227
Cu(phen)(L-Trp)	7.1	-498	235
Cu(phen)(L-Tyr)	7.0	-496	195

The reduction peak occurs generally at negative potentials versus Ag/AgCl reference electrode. As one can see form table 8.7., the copper(II) ternary complexes with aromatic residues present a slightly more positive formal redox potential values than those with aliphatic residues and this small difference could be probably ascribed to weak interligand stacking interactions, which are known to be present in these systems.[153,165]

Copper(II) ternary complexes [Cu(phen)(AA)] with aminoacidate carrying positively charged residues also showed more positive formal redox potentials. Anyway the substantial negative formal redox potentials found for these ternary copper(II) complexes correlate well with their tetragonally elongated octahedral geometries found in this spectroscopic study.

8.4.4 The case of [Cu(phen)(L-His)]

As introduced in section §8.4.1 the ternary copper(II) complex [Cu(phen)(L-His)] behaves differently from those analysed till now. In this section spectroscopical and voltammetric measurements associated with this complex species will be illustrated at different pH values.

First, the RT CW-EPR spectrum in the 2nd derivative mode on a solution of [Cu(phen)(L-His)] in 1:1:1 metal to ligands ratios at acidic pH value is shown in figure 8.11.

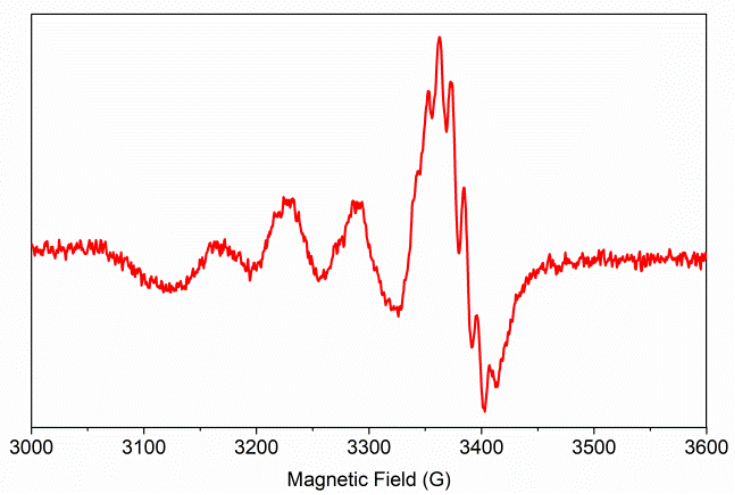

Figure 8.11. 2nd derivative mode RT CW-EPR spectrum of [Cu(phen)(L-His)] prepared with the metal to ligands ratio 1:1:1 in aqueous solution at pH 5.

This RT CW-EPR spectrum was obtained subtracting the contribution of [Cu(phen)] giving it a weight of 35 % according to the species distribution diagram of figure 8.7. The resulting CW-EPR spectrum presents seven shf lines superimposed on the hyperfine line at highest field.

The following isotropic magnetic parameters were extracted: g_{iso}= 2.120 ± 0.002, a_{iso}= 68 ± 2x10^{-4} cm^{-1}, a_{iso}^{N}= 10 ± 1x10^{-4} cm^{-1}. This RT CW-EPR spectrum, ascribable to [Cu(phen)(HisH)] species, presents the same parameters recorded for the other ternary copper(II) complexes [Cu(phen)(AA)] (table 8.6.).

LT CW-EPR spectrum of [Cu(phen)(L-His)] recorded at 150 K at the same pH is shown in figure 8.12. It clearly presents two absorbing species as expected by the species distribution diagram: the simple copper complex [Cu(phen)] and the ternary copper(II) complex [Cu(phen)(HisH)].

The first has these anisotropic parameters: $g_{||}$ = 2.310 ± 0.003, $A_{||}$ = 162 ± 3x10^{-4} cm^{-1}, $g_{\perp}$ = 2.067 ± 0.005, $A_{\perp}$ = 8 ± 5x10^{-4} cm^{-1}. These parameters are not dissimilar from those reported in the literature.[166]

The ternary [Cu(phen)(HisH)] shows a frozen EPR spectrum similar to those of the other copper(II) ternary complexes with the following parameters: $g_{||}$ = 2.240 ± 0.003, $A_{||}$ = 187± 3x10^{-4} cm^{-1}, $g_{\perp}$ = 2.053 ± 0.005, $A_{\perp}$ = 11 ± 5x10^{-4} cm^{-1} (table 8.6.)

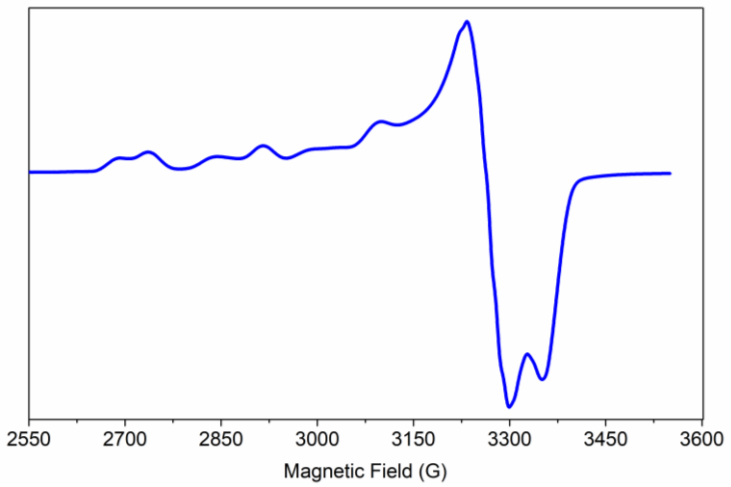

Figure 8.12. 2nd derivative mode LT CW-EPR spectrum of [Cu(phen)(L-His)] prepared with the metal to ligands ratio 1:1:1 in aqueous solution at pH 5.

Taken all together these results it is possible to conclude that, at relatively acidic pH values, in the case of Cu-phen-L-His system, the coordination environment around copper(II) ion is not different from that of the other copper(II) ternary complexes so far examined. This complex shows a pseudo-octahedral geometry with a CuN_3O in plane chromophore.

The situation is completely different when the pH value is raised up to the neutral region. The RT CW-EPR spectrum, reported in figure 8.13, does not show resolved shf lines due to coordinated nitrogen atoms. However, the isotropic spin Hamiltonian parameters extracted from this CW-EPR spectrum are quite different from those determined at pH 5: g_{iso} = 2.125 ± 0.002 and a_{iso} = 60 ± 2x10^{-4} cm^{-1}. These data indicate the formation of another species at neutral pH that is ascribable to [Cu(phen)(His)]$^{+}$, according to the species distribution diagram of figure 8.7.

LT CW-EPR spectrum of this solution always at neutral pH is illustrated in figure 8.14. Unfortunately it is not conclusive because it shows more than one absorbing species. In order to disentangle this complex LT CW-EPR spectrum, a simulation was performed (dot line in figure 8.14) resulting in three different species which contribute to the overall EPR spectrum.

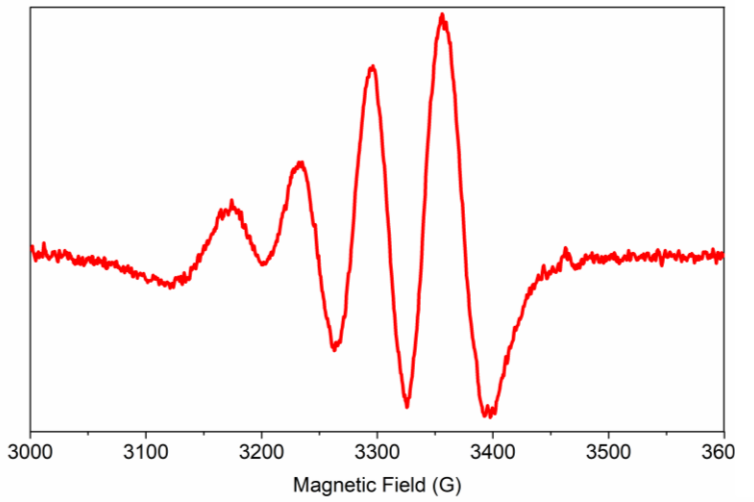

Figure 8.13. 2nd derivative mode RT CW-EPR spectrum of [Cu(phen)(L-His)] prepared with the metal to ligands ratio 1:1:1 in aqueous solution at pH 7.

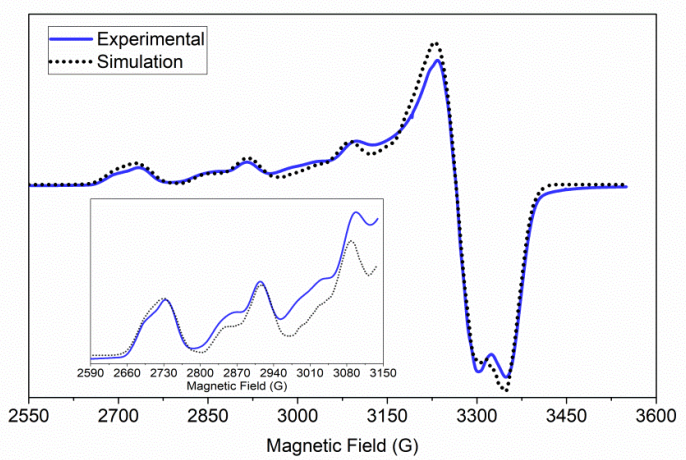

Figure 8.14. 2nd derivative mode LT CW-EPR spectrum of [Cu(phen)(L-His)] prepared with the metal to ligands ratio 1:1:1 in aqueous solution at pH 7. The dot line represents the best simulation of the entire spectrum. The inset shows the enlarged parallel part.

The formation percentages of each species and the corresponding anisotropic magnetic parameters, achieved by the simulated CW-EPR spectrum, are reported in table 8.8. together with the experimental anisotropic magnetic parameters extracted at acidic pH for the complexes $[Cu(phen)]^+$ and [Cu(phen)(HisH)] for comparison.

At first sight the two additional copper complex species might be considered the disproportion products of $[Cu(phen)(His)]^+$, namely $[Cu(phen)_2]^{2+}$ and $[Cu(His)_2]$, according to the reaction written below:

$$2\ [Cu(phen)(His)]^+ \rightleftarrows [Cu(phen)_2]^{2+} + [Cu(His)_2]$$

Table 8.8. Percentages of formation and anisotropic spin Hamiltonian parameters of copper(II) complex species calculated from the simulated LT CW-EPR spectrum of figure 8.14 (dot line). The anisotropic spin Hamiltonian parameters of [Cu(phen)] and [Cu(phen)(HisH)] are reported below for comparison. Estimated experimental errors on the last digit are reported in brackets.

Complex	***abundance***	$g_{\|\|}$	$A_{\|\|}$ (10^{-4} cm^{-1})	$g_{\perp}$	$A_{\perp}$ (10^{-4} cm^{-1})
species 1	45%	2.304(5)	162(3)	2.068(5)	7(5)
species 2	38%	2.239(4)	184(3)	2.054(5)	9(5)
species 3	17%	2.282(5)	173(3)	2.064(5)	8(5)
[Cu(phen)]		2.310(3)	162(3)	2.067(5)	8(5)
[Cu(phen)(HisH)]		2.240(3)	187(3)	2.053(5)	11(5)

Nevertheless, the average magnetic parameters reported in the literature for the copper(II) bis complex species with phen and His are different from the simulated parameters. In particular, for $[Cu(phen)_2]^{2+}$, the following anisotropic magnetic parameters are reported:[142,167] $g_{||}$ = 2.280 ± 0.003, $A_{||}$ = 164 ± 4x10^{-4} cm^{-1}, $g_{\perp}$ = 2.070 ± 0.005, $A_{\perp}$ = 29 ± 5x10^{-4} cm^{-1}; for $[Cu(His)_2]$:[164,168] $g_{||}$ = 2.228 ± 0.008, $A_{||}$ = 185 ± 5x10^{-4} cm^{-1}, $g_{\perp}$ = 2.050 ± 0.006, $A_{\perp}$ = 13 ± 5x10^{-4} cm^{-1}. Thus, this first hypothesis must be excluded.

However, looking at the table 8.8 more in details, it is possible to note that the most abundant copper species (45%), found by simulating the LT CW-EPR spectrum, has actually identical magnetic parameters of the $[Cu(phen)]^{2+}$ complex. It means that the ternary $[Cu(phen)(His)]^{+}$ species dissociates at low temperature.

The second species (38%) is ascribable to the same ternary complex [Cu(phen)(HisH)] obtained at pH 5, according to the anisotropic magnetic parameters reported in the table 8.8. Finally, the third species (17%) might be a square-based pyramidal complex (properly $[Cu(phen)(His)]^{+}$), in which histidine probably coordinates copper with its histamine-like mode. The higher g parallel value, $g_{||}$ = 2.282 ± 0.005 and the relatively lower parallel hyperfine constant, $A_{||}$ = 173 ± 3x 10^{-4} cm^{-1}, in comparison with the magnetic parameters of $[Cu(phen)(HisH)]^{+}$, tend to confirm this second hypothesis.

These observations suggest that the copper ternary complex $[Cu(phen)(His)]^{+}$ is stable only at room temperature while low temperatures disfavour its existence. Therefore there is an equilibrium between $[Cu(phen)(HisH)]^{+}$ and $[Cu(phen)(His)]^{+}$. This equilibrium is a function of the temperature and it is complicated by a side reaction which could involve the dissociation of the species $[Cu(phen)]^{2+}$ or [Cu(His)] from the copper ternary complex, according to two reactions written below:

$$2\ [Cu(phen)(His)]^{+} + H_2O \rightleftarrows [Cu(phen)(HisH)]^{+} + [Cu(phen)]^{2+} + His + OH^{-}$$

$$2\ [Cu(phen)(His)]^{+} + H_2O \rightleftarrows [Cu(phen)(HisH)]^{+} + [Cu(His)]^{+} + phenH^{+} + OH^{-}$$

Actually, [Cu(His)] species has magnetic parameters quite similar to those of the $[Cu(phen)]^{2+}$ species: $g_{||}$ = 2.310, $A_{||}$ = 170x10^{-4} cm^{-1}, $g_{\perp}$ = 2.070;[169,170] moreover both dissociation process might perhaps occur simultaneously, giving the reason of the highest abundance (45%) of this species due to both contributions.

All these results taken together led to the conclusion that the [Cu(phen)(His)] species has a different stereochemistry compared with [Cu(phen)(HisH)]: at room temperature the relatively higher g_{iso} and the smaller absolute value of a_{iso} suggest that a square based pyramidal geometry better represents the coordination environment around copper ion.[155] A scheme of two optimized geometrical models of [Cu(phen)(HisH)] and [Cu(phen)(His)] complexes is shown in figure 8.15. Unfortunately, the shf structure is not resolved in both RT and LT EPR spectra of [Cu(phen)(His)] complex species; therefore, the donor atoms in the equatorial coordination plane to copper ions cannot be drawn out. In particular, this pyramidal geometry could equivalently form from an equatorial CuN_3O chromophore with one of the nitrogen donor atoms apically bound or an equatorial CuN_4 chromophore with the carboxylate oxygen atom apically bound. Generally in a square based pyramid the metal is tilted out of the equatorial coordination plane and this could explain why the nitrogen shf structure is not resolved (or totally absent) in the RT CW-EPR spectra at pH 7 (figure 8.13). Some diffractometric results on crystals of [Cu(bipy)(His)] showed that at the solid state pentacoordinate copper(II) in an approximate pyramidal structure is simultaneously bound to four nitrogen atoms in a distorted equatorial plane with the carboxylate oxygen atom apically interacting with copper.[171]

About the frozen solution EPR spectra, unfortunately, they do not refer exactly to the major complex species present at room temperature because the freezing procedure might change the complex species distribution of the system under consideration. In our case a dissociation reaction also occurs complicating the overall picture.[163]

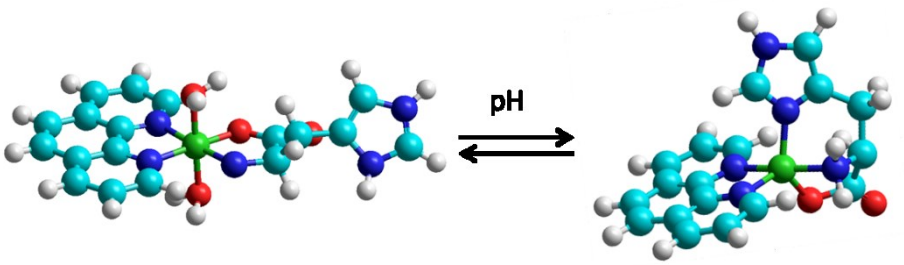

Figure 8.15. Scheme of the different coordination geometry for the complexes [Cu(phen)(HisH)], on the left, and [Cu(phen)(His)], on the right, as a function of pH.

Figure 8.16. Square wave voltammograms of the copper ternary complex [Cu(phen)(L-His)] at pH 5 (on the left)and at pH 7 (on the right) in 0.1 M KNO_3 solution as ground electrolyte.

The formation of different species in the case of ternary copper(II) complexes with phen and L-His as a function of pH is detectable also through Square-Wave voltammetry. Figure 8.16 shows the voltammograms recorded at pH = 5 and at pH = 7 of [Cu(phen)(L-His)] prepared in 0.1 M KNO_3 solution.

At pH 5, as already observed from the species distribution diagram and from the pertinent spectroscopic data, [Cu(phen)] and [Cu(phen)(HisH)] are contemporarily present and the voltammogram shows two peaks associated with the reduction of both complex species. The extracted formal redox potentials are reported in table 8.9.

At pH 5, The formal redox potential, E_p = -420 mV, is ascribable to the reduction of $[Cu(phen)(HisH)]^+$ and this value is somewhat in between the formal redox potentials found for aminoacidates having charged residues and those pertaining to aromatic residues (table 8.7.).

At pH 7 an unique SQW peak can be observed and its value is the more positive among the values associated with all the ternary systems examined in this study (table 8.7.).

Table 8.9. SWV formal redox potentials of complex species associated with Cu-phen-L-His system in aqueous solution at pH 5 and at pH 7 by using KNO_3 0.1 M as ground electrolyte. PWHH is the abbreviation of peak width at half height. Presumed errors are reported in brackets.

Complex	***pH***	***Ep, mV*** *(12 mV)*	***PWHH, mV*** *(10mV)*
Cu(phen)	5	-164	84
Cu(phen)(L-HisH)	5	-420	100
Cu(phen)(L-His)	7.1	-315	125

8.5 Conclusions and perspectives

Spectroscopic and voltammetric experimental data strongly suggest that copper(II) complexes studied in this project have a unique molecular geometry in aqueous solution. It is a tetragonally elongated octahedron with a coordination plane containing, in the case of bis and ternary complexes with Arg and Glu, the two nitrogen atoms of the amino groups and the two oxygens of the carboxylate groups coming from the aminoacidate ligands. In the case of ternary complexes with 1,10-phenantroline and amino acids, the coordination plane consists of the two nitrogen atoms of the heterocyclic diimine and the nitrogen and oxygen atoms of the aminoacidate ligand. Additionally, in all cases, two water molecules are apically bound.

The only square pyramidal geometry in aqueous solution among all these systems is probably attributable to the ternary copper(II) complex with 1,10-phenanthroline and histidine near the neutrality, in which histidine behaves as terdentate ligand and coordinates by its histamine-like mode.

These data highlight that the metal complex stereochemistry found at the solid state (where generally these copper(II) species adopt distorted square pyramid coordination geometries with a water molecule apically bound)[129,140–143] is not preserved when the complex is dissolved in a aqueous solution. Therefore, these data give important indications about the real complex geometry in solution whose knowledge is required by all biological studies where these copper(II) complexes are investigated.

In particular, in the case of ternary copper(II) complexes with Arg and Glu, the experimental data suggest the existence of an equilibrium between *cis* and *trans* conformers whose percentages of formation depend on the temperature. In physiological conditions, the body temperature is around 37°C (310K), according to the data shown in paragraph §8.3, it is reasonable to assume that the *trans* conformer predominates over the *cis,* when copper(II) ions form bis and ternary complexes with L-Arg and/or L-Glu. In this case, both charged side chains are on the same side of the CuN_2O_2 coordination. Considering that many cuproproteins are involved in redox reactions, these structural data might indicate that one of the apical sites, occupied by a water molecule, could be easily available for substitution with other substrates so that copper(II) can take part in the biochemical pathway. For instance, an involvement of copper(II) ions in glutamatergic synapses have been suggested because it is well known that copper(II) is accumulated in synaptic vesicles and it might be co-released with glutamate to modulate

the receptors' response. Some evidences suggest the existence of an oxidation-sensitive domain of AMPA receptor close to the agonist binding site and it could be affected by redox activity of copper(II) ions reducing its affinity for ligands.[172,173]

About the ternary copper(II) complexes [Cu(phen)(AA)], another consideration can be made looking at the formal redox potentials achieved by the SVW measurements. Only the $[Cu(phen)(His)]^+$ complex has the most positive formal redox potential which is ascribable to a square based pyramidal stereochemistry.[157] The other copper(II) complexes show highly negative formal redox potentials suggesting that the biochemical mechanism of action of this class of copper(II) compounds is not associated with a reduction of Cu(II) to Cu(I) ion. In a recent work on a similar class of ternary complexes with aminoacidates, a complete reduction of copper(II) complexes was only achieved by using relevant amounts of glutathione.[174]

III. PART

EPR CHARACTERIZATION OF β-PEPTIDES

9. Structural characterization of membrane proteins

Membrane proteins play a key role in all living organisms because they represent the most important way of communication between the intracellular and the extracellular environments to maintain the correct homeostasis between these two compartments. More than 60% of commercially available drugs have membrane proteins as pharmaceutical target.[175] Despite their importance, in comparison with the soluble proteins, our knowledge about their structure, function and interactions with the membrane is still insufficient due to several experimental limitations. There are many challenging steps such as expression, extraction, isolation and purification of proteins as the investigation in their natural environment under physiological conditions. For these reasons, up to now the literature is poor of high-resolution structures of membrane proteins.[175]

As discussed in chapter 5, X-ray crystallography is the leading technique in the field of structural biology. It requires always the formation of highly organized 3D crystals. In the case of membrane proteins it is not trivial to find out the best crystallization conditions in order to keep the physiological membrane environment and to guarantee the native biomolecular structure. Numerous trials have to be attempted making crystallization a challenging and time-consuming process often limited by the low availability of the sample.[175,176]

NMR spectroscopy, differently from X-ray crystallography, enables the investigation of membrane proteins in soluble detergent micelles or detergent-free membrane sample which mimics much better the protein physiological environment.[177] However, as already mentioned, this approach is strongly limited by the size of the biological system; therefore a full assignment of large membrane protein complex through NMR spectroscopy still remains a challenging task.[178]

The recent Cryo-EM microscopy can be applied for the investigation of big membrane proteins in detergent micelles requiring very low amounts of sample. This is an advantage considering the difficulties to have good expression and purification yields for these systems. This method allows to get 3D-pictures at high resolution achieved summing thousands of images of sample microcrystals obtained after a rapid freezing procedure and keeping them below 100 K. In these cryogenic conditions, water molecules have no

time to form ordered ice crystals and do not influence the picture resolution.[179]

Unfortunately, Cryo-EM imaging often requires glycerol or high salts concentrations to maintain the solubility of the membrane protein with the result to suppress contrast and signal to noise ratio.[179] Moreover, it is very difficult to investigate the dynamics of the membrane proteins following its conformational changes.[178]

In this context, EPR spectroscopy in combination with SDSL strategies is a sensitive analytical tool which can offer detailed structural information at atomic resolution on membrane proteins in their natural environment with no size limitations.[69] CW-EPR spectroscopy can deliver many information on water accessibility of nitroxide chemical environment allowing to study the topology of the protein at water-membrane edge.[178] Moreover, PELDOR/DEER spectroscopy allows to measure interspin distances between two spin labels introduced at specific positions of the biomolecule by means of SDSL approaches.[77,178] Additionally, EPR enables to investigate protein-protein and protein-lipid interactions.[178,180] Many further details and application of EPR spectroscopy in this field can be found in the chapter of BORDINGNON and STEINHOFF.[181]

The lipid environment plays a critical role to maintain the proper folding and function of a transmembrane (TM) protein. Therefore, the investigation of lipid-protein interactions is fundamental to understand at molecular level how these systems cooperate to ensure the communication between the extracellular and the intracellular sides.[182]

TM proteins are complex systems made up of different hydrophilic and hydrophobic regions whose sequence determines the overall structure and the biological function. In order to better characterize the lipid-protein interaction, many simple peptide models have been designed with the goal to mimic the most important regions of TM proteins.[183,184] This new approach has paved the way towards the design of biomimetic systems able to assume similar conformations and functions of natural biomolecules. In this way it is easier to clarify the biochemical pathways or to investigate and extend the biological features of TM proteins. Among the peptidomimetic structures, in the last years β-peptides have attracted a lot of attention due to their peculiar conformations and their biological activities.[185–188] The main features of β-peptides are discussed in the next chapter.

10. β-peptides

β-peptide is a family of synthetic oligomers which present a backbone made up of β-amino acids containing an additional methylene group between the amino and the carboxylic groups in comparison with the natural α-amino acids. According to the position of the side chain (-R), it is possible to synthesize β^2-, β^3-amino acids or the disubstituted $\beta^{2,3}$-amino acids (figure 10.1). Several synthetic routes have been suggested in the literature to achieve enantiomeric pure β-amino acids, as described in the book edited by JUARISTI and SOLOSHONOK.[189]

The presence of an additional single bond between C_α and C_β in β-amino acids largely increases the flexibility of β-peptide's backbone; therefore, it would be expected that these oligomers are entropically disfavoured to form stable conformations. In contrast with this intuitive observation, several structural investigations have revealed that these oligomers can adopt many stable secondary structures. In the last years, SEEBACH and co-workers made a lot of work in this field unveiling that β-peptides can form helices, β-sheets or hairpins, like the corresponding α-peptides.[73,186,187,190] Right- and left-handed helical secondary structures, such as 14-, 12-, 10- or 8-helix, shown in figure 10.1, are well known. The nomenclature refers to the number of atoms involved in one hydrogen-bond ring formation.[188] Surprisingly, these foldamers are even more stable than the corresponding α-helices because the larger flexibility of the backbone promotes the thermodynamically favoured *gauche* conformation of the side chains (R).[188]

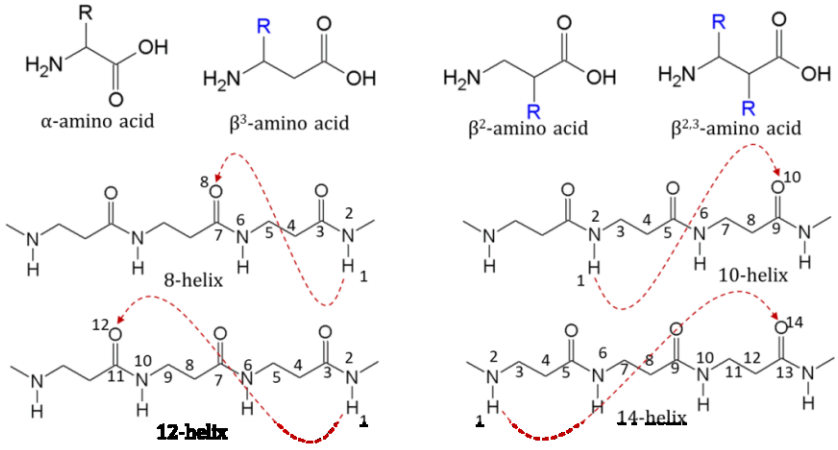

Figure 10.1. In the upper part, β-amino acids which differ in the position of the side chain (-R), depicted in blue,. Some helical β-peptide secondary structure types are shown below.

Considering that β-peptides are unnatural oligopeptides, they are resistant against the proteolytic degradation *in vitro* and *in vivo*,[191] making these oligomers suitable tools for several biological applications.[186]

β-peptides can be used as biomimetic scaffolds to synthesize peptide-based drugs.[192] For instance, a β-peptide sequence was designed to mimic a natural peptide-based antibiotic, magainins, which is naturally degraded by proteolytic enzymes, emerging as highly selective against the bacterial cells over the mammalian cells.[193]

Furthermore, the huge variety of stable foldamers make β-peptides excellent candidates to explore new protein structures or to design peptide models in order to investigate protein interactions with other targets. For instance, β-peptide sequences can give further information on the protein-lipid interaction of an analogue transmembrane α-peptide. SEEBACH and coworkers[194] have synthesized small amphiphilic β-peptides able to mimic the α-helices involved in lipid uptake in the small intestine mammalian cells.

The properties of β-peptides are strictly related to their primary sequence and their conformations. Among all possible secondary structures, one of the most investigated is the 14-helix whose features were already well characterized through NMR, X-ray diffractions and CD measurements.[187,195–197] The overall structure differs from that one of an α-helix for the polarity, net dipole and radius, as shown in figure 10.2.[187] An α-peptide consisting of L-amino acids folds into a right-handed helix, while, the corresponding β-peptide sequence forms a left-handed 14-helix with a reverse oriented net dipole. The distance between two consecutive turns of the helix, called pitch, is a bit longer in an α-helix than in a 14-helix, whereas the diameter of one hydrogen bond-ring is larger in the latter.

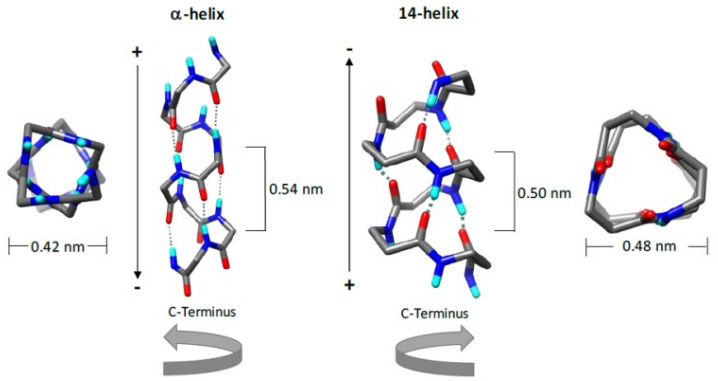

Figure 10.2. Comparison between an α-helix and a 14-helix. The figure is taken from the PhD thesis of Dr. Janine Wegner.[185,198]

Additionally, one turn of the α-helix consists of 3.6 residues while a 14-helix presents approximately 3 residues per turn, therefore, this secondary structure is generally called 3_{14}-helix. However, some oligopeptides with a 3_{14}-helix secondary structures have been investigated revealing that the periodicity might be slightly different. In particular, SEEBACH and co-workers[199] studied a β^3-eicosapeptide made up of 20 L- β^3-amino acids highlighting an offset of around 15° in the right-handed direction from the ideal 3_{14}-helix. These experimental data suggested a periodicity of 3.1 ÷ 3.4 residues per turn of the 14-helix.

To get further details about the 3_{14}-helix secondary structure, in this project, EPR spectroscopy in combination with SDSL approach were employed to investigate one turn of the 14-helix in a representative β-peptide sequence designed by DIEDERICHSEN and co-workers (figure 10.3).[200] The potential of TOPP spin label to get structural information on β-peptide secondary structure was investigated. A recent study on WALP-TOPP transmembrane α-peptide reveals that this spin label is a suitable tool for high-resolution distance measurements in solution and in lipid bilayer.[77]

In this project β-peptide secondary structure was characterized in solution and in multilamellar vesicles (MLVs). Therefore, the backbone consists of 19 β^3-Val (depicted in red in figure 10.3), as central hydrophobic region, and eight hydrophilic residues (in blue): 2 β^3-Trp and 2 β^3-Lys on each side. Previous data have revealed that β^3-Val are able to stabilize the 14-helix formation.[201] Similar to WALP peptides, the tryptophans interact with the head groups of the phospholipids in order to orient the β-peptides in the lipid bilayer because their indole ring is preferentially located close to the carbonyl groups of the lipid chains.[200,202] The two β^3-Lys increase the solubility of β-peptide in solution. Preliminary CD measurements have indicated that this sequence forms a 14-helix secondary structure in solution and in lipid bilayer.[200,202] CW-EPR and pulsed EPR experiments were performed on β^3-TOPP peptide sequences to obtain more detailed structural information on the periodicity of the helix.

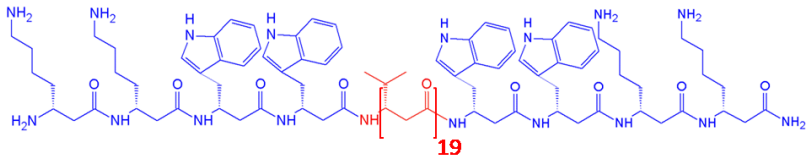

Figure 10.3. β-peptide designed by DIEDERICHSEN and co-workers.[200]

11.CW and pulse EPR characterization of β^3-TOPP peptides

This project was developed at the Max Planck Institute for Biophysical Chemistry (Göttingen, Germany) in the research group of Electron-Spin Resonance spectroscopy, under the supervision of Professor MARINA BENNATI, in collaboration with Dr. KARIN HALBMAIR and ANNEMARIE KEHL and with the research group of Professor ULF DIEDERICHSEN of the Institute for Organic and Biomolecular Chemistry at the Georg-August University of Göttingen.

Some results are illustrated in the PhD thesis of Dr. JANINE WEGNER,[198] who was directly responsible for the design of the project, synthesis, purification and the theoretical models of spin labelled β^3-peptides adopted in this thesis. A paper containing most of these data is actually under revision for a publication on a scientific journal. Some figures of this chapter are adapted from it.

11.1 Scope and design of the project

Four β^3-TOPP doubly labelled peptides based on the sequence of figure 10.3 have been synthesized and characterized by EPR spectroscopy in solution and in lipid bilayer. The nitroxide β^3-TOPP spin labels were introduced in defined positions of β^3-peptide hydrophobic stretch to investigate one turn of the helix in order to check if the periodicity changes between solution and a lipid environment.

Firstly, CW-EPR measurements at X-band frequency (9.5 GHz) were carried out on β^3-TOPP peptides prepared in solution to verify the labeling efficiency of the samples. The CW-EPR spectra were also recorded in the same samples prepared in multilamellar vesicles (MLVs) to investigate the mobility of nitroxide spin label in the lipid environment.[48,77,181]

3-pulse ESEEM experiments at Q-band frequencies (35 GHz) on the EPR samples prepared in deuterated lipid and protonated buffer were employed to have more clear indications about the peptide incorporation into the lipid bilayer measuring the electron-nuclear dipolar interactions with the deuterons in the surrounding. Finally, PELDOR/DEER distance measurements at Q-band frequencies (35 GHz) have enabled to explore the periodicity of the 3_{14}-helix secondary structure at atomic resolution measuring the interspin distances between two β^3-TOPP spin labels.

11.1.1 β³-TOPP peptide samples

In order to investigate one turn of β³-peptide 3_{14}-helix by EPR spectroscopy, four doubly labelled β³-peptide sequences were designed based on the backbone shown in figure 10.3. Nitroxide TOPP spin label, introduced in paragraph 4.2., was employed to make the samples detectable by EPR. The unnatural β³-TOPP amino acid, shown in the inset of figure 11.1, was synthesized by Dr. JANINE WEGNER[198] and incorporated directly into the β³-peptide sequence. The nitroxide spin labels were introduced into the hydrophobic stretch replacing two β³-Val for each sample.

The positions which have to be modified were defined according with the actual distance limits for PELDOR/DEER measurements, discussed in section §3.3.1, so that the expected interspin distances exceed 2 nm. Moreover, to avoid any π-π interactions with the aromatic side chains of tryptophan, β³-TOPP labels were not placed in close proximity to these residues. Taking into account all these considerations, one β³-TOPP label replaces the β³-Val in position 22 in all mutants. The four β³-peptide differ in the position of the second nitroxide radical (9, 8, 7 and 6). Consequently, the distances between the labels are in the range 13 ÷ 16 amino acids. For this reason, the four peptides are named: β-TOPP[1-14] (red), β-TOPP[1-15] (blue), β-TOPP[1-16] (green) and β-TOPP[1-17] (in orange), figure 11.1.

Considering that the whole sequence is 4.50 nm long, with a hydrophobic stretch of 3.17 nm, the interspin distances estimated moves in range from 2.17 to 2.67 nm. These values are calculated according with the formation of an ideal 3_{14}-helix, thus, using the basic parameters discussed in chapter 8 (3 amino acids per turn and a pitch of 0.50 nm).

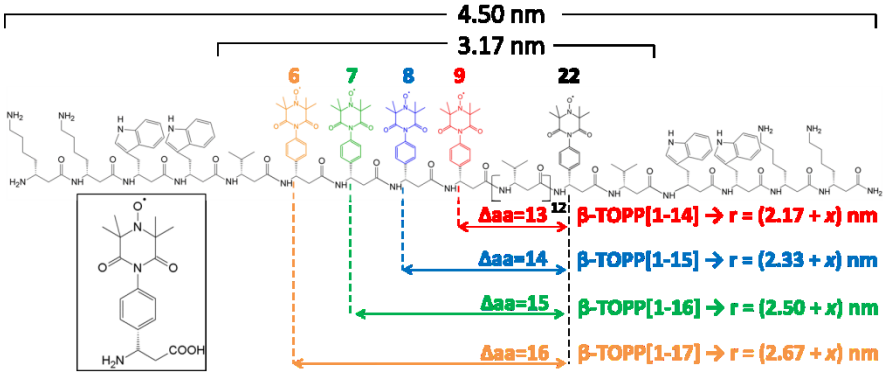

Figure 11.1. The four doubly labelled β³-TOPP peptide samples. The structure of β³-TOPP nitroxide spin label is shown in the inset.

An additional undefined contribution (*x*) in the interspin distances due to the intrinsic mobility of β^3-TOPP spin label incorporated into the peptide backbone has to be included.

However, some structural models of β^3-TOPP peptide sequences have been built to make some predictions about the PELDOR/DEER distances for these four EPR samples.[198] The models are based on three sets of torsion angles of β^3-peptide backbones published in literature[203–205] that yield to three slight different 14-helix arrangements. These structural models will be illustrated in paragraph §11.4 and, for simplicity, are called 3_{14}-QM, 3_{14}-crystal and 3_{14}-EO (this symbolism will be discussed in paragraph §11.4 as well). Three hydrophobic stretch values were extracted from each model and they are reported in table 11.1.[198]

Table 11.1. Hydrophobic stretch values estimated for four β^3-TOPP peptide 14-helix structural models based on different sets of torsion angles of β^3-peptide backbones. More details about these models will be given in paragraph §11.4.[198]

	3_{14}-QM	**3_{14}-crystal**	**3_{14}-EO**	**3_{14}-ideal**
hydrophobic stretch	2.86 nm	2.80 nm	2.52 nm	3.17 nm

11.1.2 Multilamellar vesicles of POPC

All EPR experiments were performed in methanol solution to increase the solubility of these samples, and in multilamellar vesicles (MLVs) of 1-palmitoyl-2-oleoyl-sn-glycero-3-phosphocholine (POPC), shown in the inset of figure 11.2. POPC was employed because it presents an hydrophobic thickness similar to the hydrophobic stretch of β^3-TOPP peptide sequences so that the samples can be incorporated in the lipid bilayer avoiding stretching and tilting of the backbone, aggregation or exclusion phenomena (hydrophobic match), as shown in figure 11.2.[183]

The hydrophobic match is a critical parameter that must be considered for structural characterization of transmembrane peptides in a lipid environment. Several NMR, FRET, EPR, X-ray and CD spectroscopy studies on different transmembrane peptide models have characterized the hydrophobic mismatch phenomena which influence the structure and the dynamics of membrane proteins into their natural environment.[183,206,207]

The hydrophobic thickness ($2D_C$) of a lipid bilayer is defined as the distance between two opposite acyl chains starting from the carbon C_2. [184] However, this value can be varied according to the different experimental conditions. Based on data in the literature, the hydrophobic thickness of a lipid bilayer made up of POPC fits well with the hydrophobic stretch values reported in table 11.1 ($2D_C \approx 2.58 \div 2.88$ nm)[208–210] to ensure a matching condition between polypeptide and membrane.

β^3-peptide samples in MLVs were prepared in two ways: in one case deuterated phospholipid (d_{31}POPC) and Tris(hydroxymethyl)aminomethane hydrochloride (Tris-HCl) buffer in H_2O were employed; in the second case, protonated POPC and Tris-HCl buffer in D_2O. d_{31}POPC has deuterium instead of hydrogen atoms in the saturated aliphatic acyl chains.

These two sample preparations were designed to better clarify the incorporation of the β^3-peptide into the lipid bilayer through the EPR experiments as discussed in the paragraph §11.3 Results and Discussions.

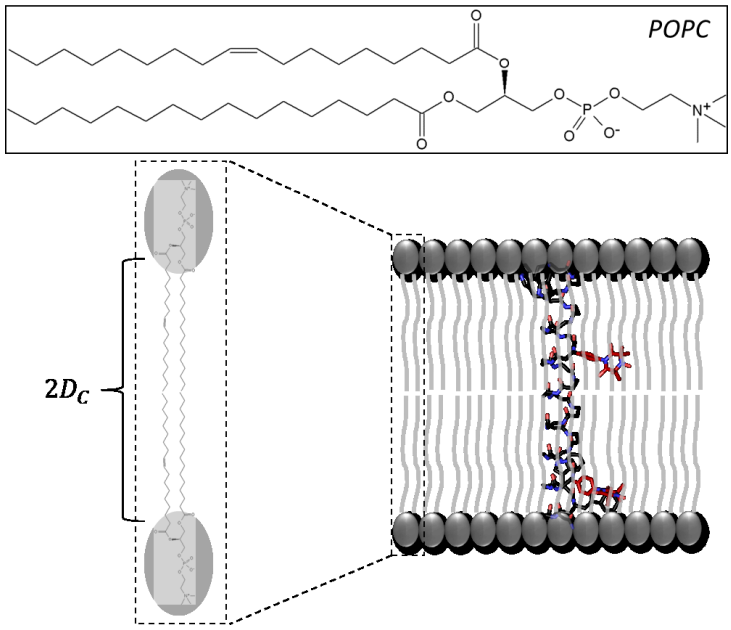

Figure 11.2. Scheme of the hydrophobic match between POPC, shown in the inset, and a structural model of one β^3-TOPP peptide sequence adopted in this thesis. $\boldsymbol{2D_c}$ is the hydrophobic thickness of the lipid bilayer.

11.2 Materials and methods

The four β^3-TOPP peptide samples were received as a dry white powder by Dr. JANINE WEGNER (Georg-August University of Göttingen) and stored at -20°C up to their use.

11.2.1 Preparation of EPR samples

β^3-TOPP sequences for EPR experiments in solution were prepared by dissolving the peptides in methanol containing 20% glycerol as cryoprotectant. Peptide concentrations, as determined by UV absorbance of the tryptophans, were adjusted adding the proper volume of methanol in order to reach 50 µM. Sample volumes of 20 µL were transferred into EPR quartz tubes (1.6 mm O.D., 1 mm I.D.) to perform CW-EPR experiments.

β^3-TOPP peptides in multilamellar vesicles (MLVs) of POPC in Tris-HCl buffer (20 mM, pH = 7.4) were prepared either using D_2O-buffer and protonated lipid (POPC) or H_2O-buffer and deuterated lipid (d_{31}POPC). Stock solutions of POPC or d_{31}POPC (25 mg/mL) in chloroform and the β^3-TOPP-labeled peptide in methanol were mixed yielding a spin/phospholipid molar ratio of ≈ 1/3000. A previous study on a transmembrane α-peptide revealed that this value of spin/phospholipid ratio prevents the aggregation of the peptide at the membrane.[77] Solvents were removed under nitrogen stream followed by 3 h vacuum drying. Tris-HCl buffer (20 mM, pH = 7.4) was added to the dry β^3-peptide/phospholipid mixture yielding spin concentrations of 40 µM. After 1 h of incubation, 20 µL of sample were transferred into an EPR quartz tube (1.6 mm O.D., 1 mm I.D.) and used for CW-EPR experiments at room temperature. After that all EPR samples were frozen in liquid nitrogen before performing pulsed EPR experiments.

11.2.2 CW-EPR experiments and labeling efficiency

CW-EPR experiments were performed at room temperature and at X-band frequencies (9.5 GHz) in a Bruker Elexsys E500 spectrometer equipped with a Bruker super-high Q resonator ER4122SHQE.

For characterization of the labeling efficiency, the standard 4-Hydroxy-2,2,6,6-tetramethylpiperidine 1-oxyl (4-OH-TEMPO) standard was employed. Five standard solutions were prepared in a range of concentrations between

10 µM and 200 µM dissolving 4-OH-TEMPO in the same methanol solution adopted for β^3-TOPP peptides. CW-EPR spectra of each standard was recorded and the double integration of the EPR signal was calculated to build up a calibration curve. CW-EPR spectra of β^3-TOPP labeled peptides in methanol solution were recorded as well and the double integration of their EPR signal revealed the samples' spin concentration by interpolation with the calibration curve. Labeling efficiency was calculated by comparing spin concentrations determined by EPR and nominal peptide concentration determined by UV absorbance of the tryptophans.

CW-EPR spectra of each β^3-TOPP labelled peptide in MLV were recorded as well to investigate the mobility of nitroxide radical in lipid bilayer.

Instrumental settings were the following: ν = 9.874 GHz; center field = 3520 G; sweep width = 200 G; microwave power = 2 mW; modulation frequency = 100 kHz; modulation amplitude = 1 G; conversion time = 5.12 ms; sweep time = 5.24 s. The number of scans varied in a range from 100 to 500 according to the intensity of the EPR signal.

All CW-EPR spectra were simulated with the EasySpin program[211] to extract information on the correlation times of nitroxide spin labels in both environments.

11.2.3 Pulsed EPR experiments

Pulsed EPR experiments were performed at Q-band frequencies using a commercial Bruker Elexsys E580 pulse X/Q-band spectrometer equipped with a pulsed 170 W Q-band TWT-amplifier (Model 187Ka, Applied Systems Engineering Inc.), a Bruker ENDOR resonator (EN5107D2), a continuous He-flow cryostat (CF95550, Oxford Instruments) and a temperature controller (ITC-5035, Oxford Instruments). The experimental temperature was set to 80 K during the introduction of the sample into the resonator and stabilized at 50 K to perform EPR experiments.

Electron spin echo envelope modulation (ESEEM) experiments were carried out using the three-pulse sequence $\frac{\pi}{2}$ - τ - $\frac{\pi}{2}$ - T - $\frac{\pi}{2}$ with a pulse length of 8-10 ns. In order to avoid *blind spots*, 2D-experiments were performed. In the *x*-axis 512 points were acquired with increasing the delay time T between the second and the third $\frac{\pi}{2}$ pulse with a time-step of 4 ns. In the *y*-axis the delay time τ between the first and the second $\frac{\pi}{2}$ pulse was

increased with a time-step of 16 ns starting from 254 ns to 398 ns. 4-step phase cycling was applied to suppress artefacts due to overlaps between echoes. The area of the stimulated echo was integrated fixing a symmetric gate around the center of the EPR signal with a length between 8 and 14 ns. 20 shots per points were acquired with a shot repetition time of 3 ms. The microwave frequency was set to the center of the resonator dip and the magnetic field adjusted to the maximum of the EPR signal. The number of scans varied between 15 and 20. Each spectrum was converted from the time domain to the frequency domain applying the Fourier transformation. Firstly, the experimental data were background corrected using a 1st order polynomial function. Then, a zero-filling procedure was adopted achieving 2048 points in order to improve the resolution of the Fourier transformation procedure. The Hamming window function allowed smoothing the exponential decay of the stimulated echo till zero. Fourier transformation function was applied focusing on a range of frequencies from 5 to 60 MHz including the Larmor frequencies of deuterons and protons at Q-band frequencies.

All PELDOR/DEER experiments were performed under strong overcoupling conditions in order to ensure a broad dip of resonance. The standard 4-pulse sequence was adopted fixing ν_{pump} 30-50 MHz over the center of the dip in the maximum of the nitroxide line and ν_{detect} 90 MHz below ν_{pump}. This set-up allows to generate short pulses with large bandwidths for both pumping and detection frequencies to avoid orientation selection. PELDOR/DEER experiments on samples in MeOH were carried out with typical π-pulse length of 12 ns at ν_{pump} and 20/22 ns at ν_{detect}. The typical π-pulse length was 12/14 ns at ν_{pump} and 14/16 ns at ν_{detect} for EPR samples in MLVs. Time delay between the first $\frac{\pi}{2}$ and the second π detection pulses was set to 400 ns. The dipolar evolution time between the Hahn-echo sequence and the third detection pulse varied in a range between 1.2 and 4.3 µs. The pump π pulse was applied at 500 ns and moved with a time-step of 4-8 ns with the last pulse applied 100 ns before the last detection π pulse to avoid an overlap between pump and detection pulses. However, some artefacts appeared in the last 100-800 ns of the experimental PELDOR/DEER trace, that was cut during data analysis. The area of the refocused echo was integrated fixing a symmetric gate around the center of the EPR signal with a length between 20 and 34 ns to reduce the noise of the PELDOR/DEER trace. 50 shots per points were acquired with

a shot repetition time of 4 ms. Typical acquisition times were on the order 10 ÷ 22 h. The number of scans recorded per hour varied between 39 and 95 depending on the length of the respective PELDOR/DEER trace.

For data analysis, the program DeerAnalysis[5] was employed: dipolar traces were background corrected using either a mono-exponential or a second-order polynomial function. Distance distributions were extracted from the experimental data, using a fitting procedure based on Tikhonov regularization.[40]

11.3 Results and Discussions

11.3.1 CW-EPR spectra of β³-TOPP peptides

Normalized experimental and simulated CW-EPR spectra of β^3-TOPP peptide samples recorded at room temperature in methanol solution and in MLVs of d_{31}POPC or POPC are reported in figure 11.3. It is possible to observe for all samples three EPR lines typical of a nitroxide radical.

The linewidths and the different intensities of EPR lines in methanol solution (first column) reveal some mobility restrictions due to the incorporation of β^3-TOPP spin label into the peptide backbone.

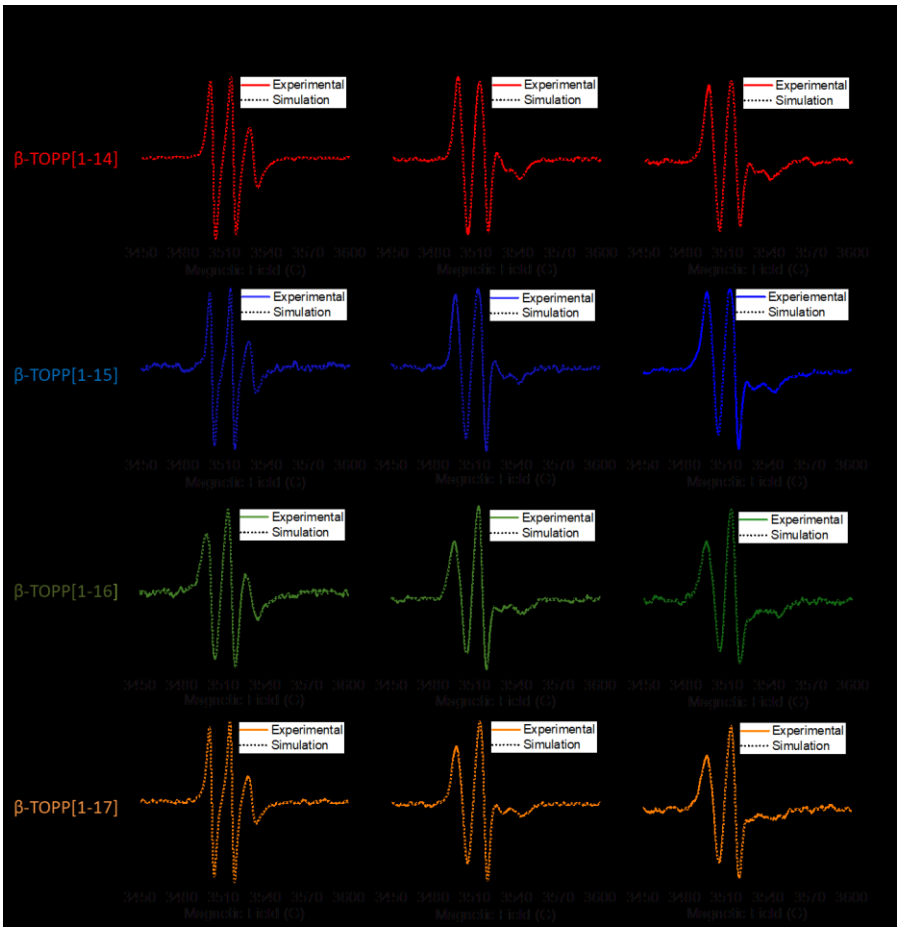

Figure 11.3 Normalized experimental (coloured solid line) and simulated (black dot line) CW-EPR spectra of β^3-TOPP peptides in methanol solution with 20% glycerol (first column); MLVs of d_{31}POPC with Tris-HCl buffer in H_2O (second column); MLVs of POPC with Tris-HCl buffer in D_2O (third column).

As a result, g and hyperfine anisotropies are partially resolved affecting, in particular, the intensity of the third EPR line.

Looking at CW-EPR spectra acquired in lipid bilayer, a further broadening proves the reduced mobility of β^3-TOPP spin label in this environment with the third EPR line which almost disappears in the baseline.

These observations are confirmed by the EasySpin simulations: the chili spectral simulation function[211] was used to simulate the lineshape modifications as dependent on the different correlation times along the three axis: τ_x, τ_y and τ_z. The following magnetic parameters were adopted to fit the experimental data: g_1= 2.0086 ± 0.0006, g_2= 2.0048 ± 0.0006, g_3= 2.0037 ± 0.0006, A_1= 16 ± 3, A_2= 10 ± 5, A_3= 64 ± 9. The linewidths (lw) and the correlation time values are shown in table 11.2.

Looking at these parameters it is possible to note how the EPR signal broadens in lipid bilayer with a linewidth which almost doubles in most of the cases comparing with the same sample in methanol.

The calculated correlation times in solution confirm the axial symmetry of β^3-TOPP spin label also suggested by previous studies.[14,76,77] In particular, τ_x and τ_y assume similar values of the order of nanoseconds, while the motions around the *z* axis are much more slower with a τ_z of the order of μs or in some cases ms.

Table 11.2. Linewidths (lw) and correlation time parameters of β^3-TOPP peptide samples in methanol solution and in lipid bilayer estimated through EasySpin simulations of the experimental CW-EPR spectra. The values are affected by an estimated error of 10%.

EPR samples		lw	τ_x	τ_y	τ_z
β-TOPP[1-14]	*MeOH*	0.22	1.3 ns	2.6 ns	70.8 μs
	d_{31}POPC	0.40	10.2 ns	286 μs	552 μs
	POPC	0.46	6.5 ns	7.7 μs	28 ms
β-TOPP[1-15]	*MeOH*	0.13	1.3 ns	2.3 ns	28.2 μs
	d_{31}POPC	0.35	5.8 ns	7.5 μs	24.4 ms
	POPC	0.49	3.2 ns	50 μs	12 ms
β-TOPP[1-16]	*MeOH*	0.34	1.9 ns	2.2 ns	69 ms
	d_{31}POPC	0.46	7.7 ns	93.8 μs	6.2 ms
	POPC	0.53	7.3 ns	1.1 μs	49 ms
β-TOPP[1-17]	*MeOH*	0.12	1.4 ns	2.7 ns	2.2 μs
	d_{31}POPC	0.35	8.0 ns	123 μs	882 μs
	POPC	0.39	7.1 ns	1.7 μs	54 ms

These parameters are in agreement with the data obtained by the simulations of other nitroxide radicals with axially symmetric rotational diffusion.[212]

The rotational diffusion of β^3-TOPP spin label becomes fully anisotropic in lipid bilayer with a severe enhancement of τ_y more than three orders of magnitude and τ_x values which undergo only a slight raising.

The similar lineshape of experimental nitroxide CW-EPR spectra recorded in MLVs of d_{31}POPC with protonated Tris-HCl buffer and in MLVs of POPC with deuterated Tris-HCl buffer indicate that deuterons or protons do not influence the nitroxide radical magnetic parameters. However, the unique effect is a decreasing of the EPR signal absolute intensity in POPC comparing with d_{31}POPC, as documented for the sample β-TOPP[1-17] in figure 11.4, shown as example. This is a consequence of the lower relaxation times of the electron spin magnetic moment placed into a protonated chemical environment than in a deuterated one, as discussed in chapter §3.

These spectroscopical features give a first clue about the incorporation of β^3-TOPP peptides into the lipid bilayer: the samples prepared in MLVs of d_{31}POPC with protonated buffer show a higher EPR signal intensity because β^3-TOPP spin labels are in close proximity to the deuterons of d_{31}POPC acyl chains. On the contrary, in MLVs of POPC, the nitroxide radicals are closer to the protons of POPC phospholipid chains giving an EPR signal which presents almost half intensity comparing with the first sample preparation.

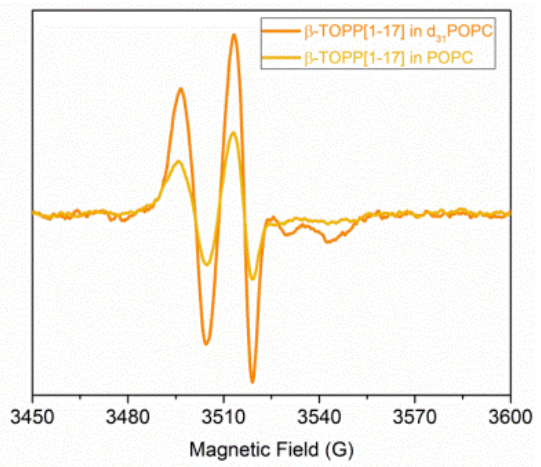

Figure 11.4. Comparison between the absolute intensities of the experimental β-TOPP[1-17] CW-EPR spectra recorded in d_{31}POPC (orange) and POPC (yellow) MLVs.

11.3.2 Estimation of spin concentration and labeling efficiency

Estimation of spin concentration for each β3-TOPP peptide sample was achieved employing a calibration curve built up with 4-OH-TEMPO standard solutions in a range of concentrations between 10µM and 200µM. Their CW-EPR spectra were recorded in the same medium of EPR samples prepared in solution (80 % methanol + 20 % glycerol). Then, the double integration of the EPR signals was calculated to build up the standards calibration curve, shown in figure 11.5. Double integration of β3-TOPP peptide sample CW-EPR spectra in methanol was calculated as well to extract their spin concentration by interpolation. The β3-TOPP peptide samples were prepared with a peptide concentration around 50 µM. Considering that each β3-peptide is doubly labelled, the expected spin concentration might be around 100 µM to reach 100% labeling efficiency.

The experimental spin concentrations are around 60 % less than those expected. These spin concentration values were taken as reference to prepare the EPR samples in lipid bilayer in order to use the proper amount of peptide to reach 40 µM spin concentrations in MLVs. Some HPLC evidences from Dr. JANINE WEGNER highlighted that after β3-peptide sequences purification, the nitroxide might undergo a reduction process to the diamagnetic hydroxyl amine group. To restore the radical species the samples might be treated with atmospheric oxygen.[198]

However, the real spin concentration is not so low to compromise the further EPR measurements.

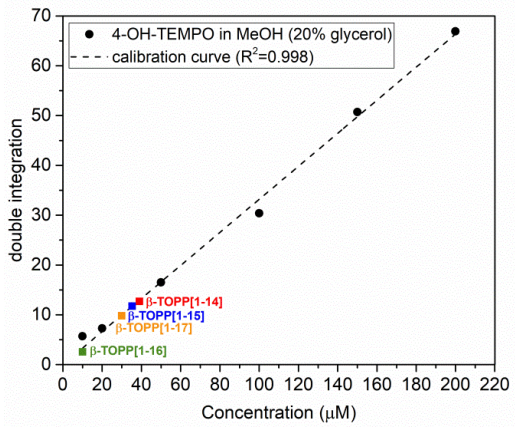

Figure 11.5. Determination of spin concentration in β3-TOPP labelled peptide samples by CW-EPR. Estimated error is about 10 % for each point.

11.3.3 PELDOR/DEER distance measurements in methanol solution

PELDOR/DEER experiments were carried out to explore one turn of β^3-TOPP peptide 14-helix secondary structure in solution and in MLVs. In this section the experimental results in methanol solution are illustrated. These PERLDOR/DEER traces were recorded and analysed by Dr. KARIN HALBMAIR at Max Planck Institute for Biophysical Chemistry (Göttingen).

The experimental traces acquired in methanol solutions, the corresponding background corrected traces and the distance distributions achieved with the DeerAnalysis program[39] are reported in figure 11.6.

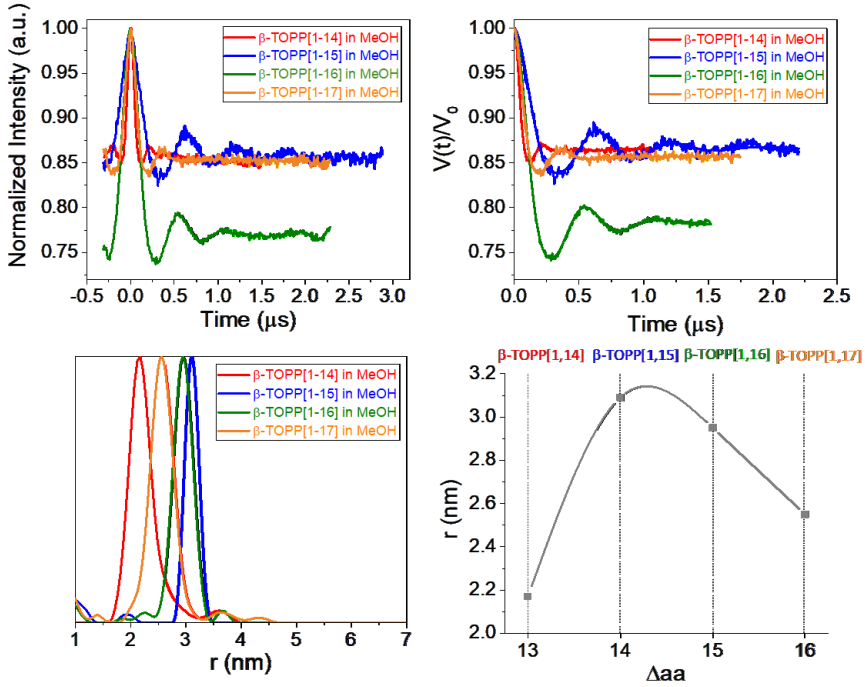

r [nm]	β-TOPP[1-14] Δaa=13	β-TOPP[1-15] Δaa=14	β-TOPP[1-16] Δaa=15	β-TOPP[1-17] Δaa=16
PELDOR	2.17	3.09	2.95	2.55
MeOH	Δr = 0.24	Δr = 0.15	Δr = 0.21	Δr = 0.21

Figure 11.6. On the upper part, the experimental PELDOR/DEER traces (left) and the background corrected traces (right) of β^3-TOPP peptides in methanol solution are shown. In the centre, the extracted distance distributions are illustrated together with a. graphical representation of their trend as a function of the amino acid separation Δaa. On the button the experimental distances are summarized in a table. Δr is the half width at half height.

All time traces present a high signal to noise ratio. After the undetected echo at zero-time, clear modulations with just one dominating dipolar frequency are visible due to the dipolar coupling between nitroxide TOPP spin labels. These data yield to reliable and narrow distance distributions characterized by one main peak centred in a range between 2.17 nm and 3.09 nm. A summary of the experimental interspin distances are reported in the table on the bottom of figure 11.6. *Δr* represents the half-width at half height of the main peak and is correlated with the mobility of nitroxide spin labels.[34]

A graphical representation of the interspin distances as a function of the amino acid interspin separation (Δaa) highlights that the trend of PELDOR/DEER distances in methanol solution is wave-like due to the helical secondary structure of β^3-peptides and the orientation of β^3-TOPP spin labels. The formation of the 14-helix secondary structure confirms the CD measurements of Dr. JANINE WEGNER.[198]

11.3.4 3-pulse ESEEM experiments on β^3-TOPP peptides in MLVs

β^3-TOPP peptides incorporation into the lipid bilayer was probed by 3-pulse ESEEM experiments. As discussed in section §3.3.2, this EPR approach enables to detect electron-nuclear dipolar coupling giving a modulated stimulated echo decay at the Larmor frequency of the nearest nuclei in the surrounding.

As introduced in section §11.1.2 β^3-TOPP peptide samples in lipids were prepared in two different conditions: in one case d_{31}POPC in Tris-HCl buffer dissolved in H_2O were employed. For the second sample preparation POPC and Tris-HCl buffer in D_2O were adopted. A deuterium modulation is expected to be detected for the samples prepared in d_{31}POPC and protonated buffer due to the close proximity between the nitroxide radical and the deuterated phospholipid chains. On the contrary, this modulation should be not visible for the second sample preparation with POPC and deuterated buffer because the β^3-TOPP spin labels incorporated into the lipid bilayer should be far away from the deuterons of the buffer.

3-pulse ESEEM experiments suffer from *blind spots* for specific τ values (section §3.3.2). Thus, to avoid a misinterpretation of the experimental data, 2D experiments were performed to find out the best parameter τ which yields to the most intense modulation.

Figure 11.7 shows, as example, the 2D 3-pulse ESEEM spectra in time domain acquired on β-TOPP[1-14] prepared in lipid bilayer of d_{31}POPC (sketched on the left). A window of τ values was swept in a range between 254 ns and 398 ns with a time-step of 16 ns. A clear modulation of the stimulated echo decay is visible and its magnitude changes according with the delay time between the first two $\frac{\pi}{2}$ pulses. The most intense modulation is visible around τ = 318 ns.

To discover which nucleus is responsible of this modulation, the EPR traces were Fourier transformed and so converted in frequency domain. At Q-band frequencies (35 GHz), deuterons have a Larmor frequency, $\nu_D \approx 7.8$ MHz and protons, $\nu_H \approx 51$ MHz.

Figure 11.8 presents the 3-pulse ESEEM experiments in time and in frequency domains of β^3-TOPP peptides in MLVs adopting both sample preparations. The shown traces were acquired with τ = 318 ns.

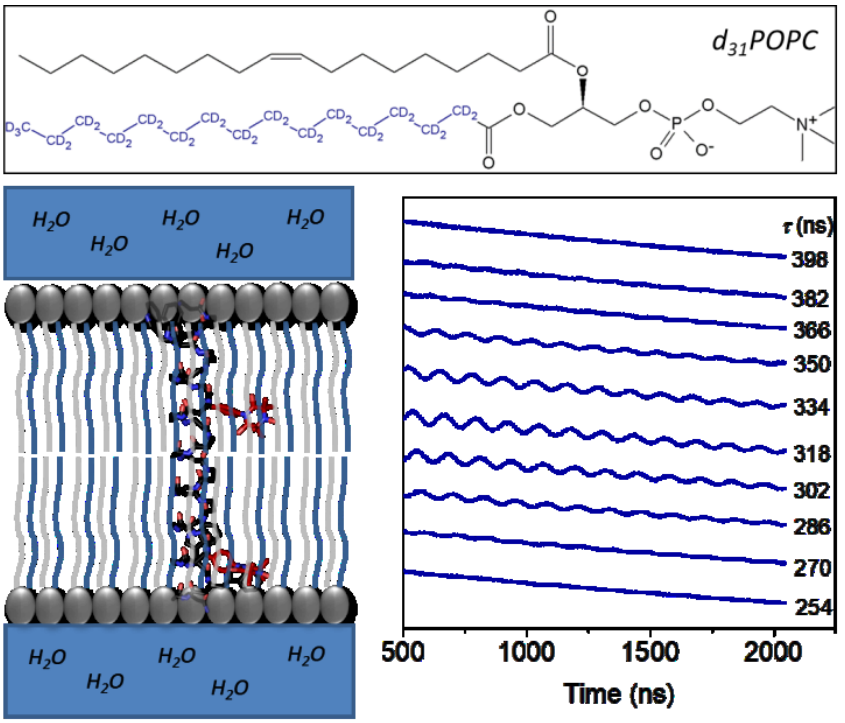

Figure 11.7. 2D 3-pulse ESEEM experiment in time domain performed on β^3-TOPP[1-14] in MLVs of d_{31}POPC, shown in the inset, and protonated Tris-HCl buffer. The time traces were recorded with a τ = 318 ns.

A clear deuterium modulation is visible only in d_{31}POPC MLVs. If POPC and D_2O-buffer are employed only a residual deuterium ESEEM is observed, which is in agreement with some penetration of water molecules into the MLVs. These experimental data support the conclusions taken from the CW-EPR spectra and further suggest a proper integration of β³-TOPP peptides into the phospholipid bilayer.

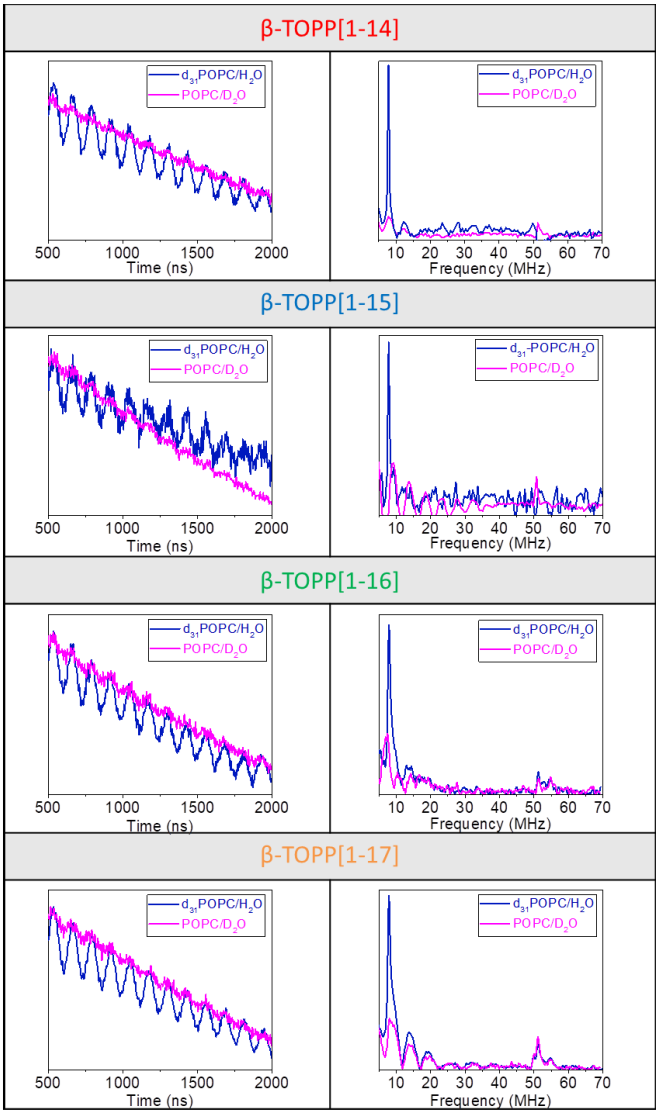

Figure 11.8. 3-pulse ESEEM spectra in time and in frequency domains of β³-TOPP peptides prepared in MLVs of POPC in D_2O-buffer (magenta line) and d_{31}POPC in H_2O-buffer (blue line).

11.3.5 PELDOR/DEER distance measurements in MLVs

The experimental PELDOR/DEER traces and the corresponding background corrected traces acquired on β^3-TOPP peptide samples in MLVs of d_{31}POPC and POPC are shown in figure 11.9. Overall for the same sample the data reveal that β^3-TOPP spin labels behave similarly in both MLVs environments yielding similar experimental traces.

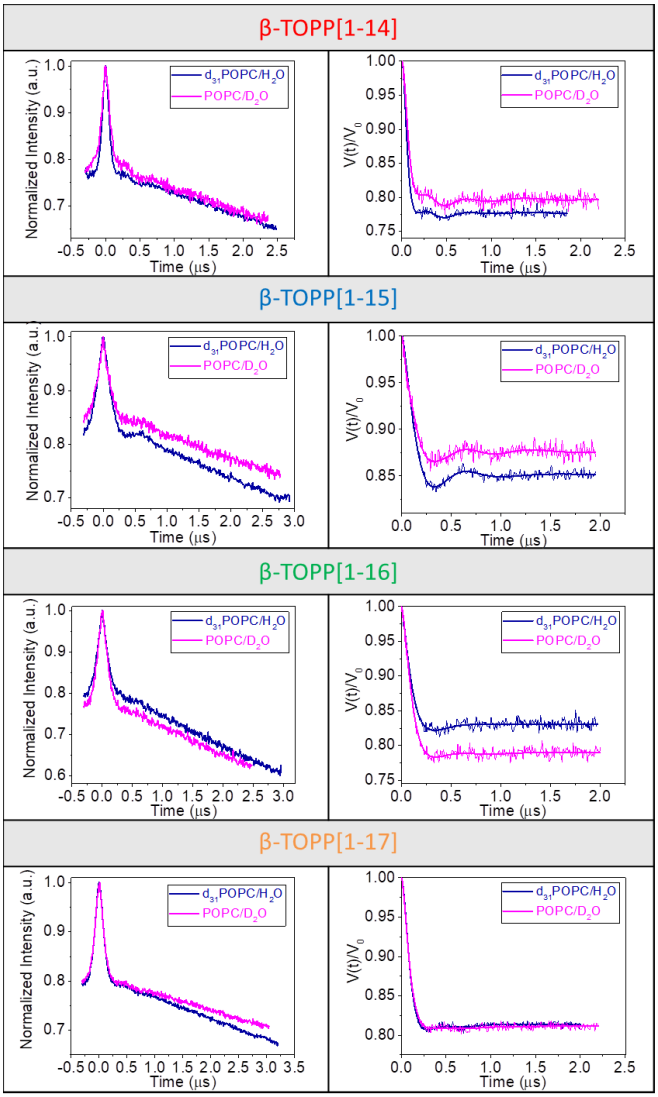

Figure 11.9. Experimental PELDOR/DEER traces (left) and the background corrected traces (right) of β^3-TOPP peptides in MLVs of d_{31}POPC (blue) and POPC (magenta) are shown.

However, it is possible to note that, keeping the same experimental set-up, the PELDOR/DEER traces recorded in POPC MLVs have a worse signal to noise ratio than the corresponding samples in d_{31}POPC. Like the CW-EPR spectra, this effect is associated with the decreasing of refocused echo intensity due to the POPC protonated phospholipid chains which reduce the relaxation times of the closed nitroxide radicals.

After the undetected echo at zero-time, dipolar modulations are visible. The most evident is that one of β-TOPP[1-15]; while two shallow dipolar modulations are detectable for the samples β-TOPP[1-16] and β-TOPP[1-17]. About the sample β-TOPP[1-14], more than one dipolar frequencies contribute to the PELDOR/DEER trace which yields a more complex distance distribution.

Distance distributions of β^3-TOPP peptides in MLVs are reported in figure 11.10 together with the PELDOR/DEER distances previously measured in methanol solution for comparison. The extracted distance distributions in lipid bilayer are very similar to each other and present the same main peak centred in a range between 2.37 nm and 3.09 nm for both sample separations. These results confirm the large accuracy and reliability of PELDOR/DEER technique for high-resolution distance measurements in biomolecular structures. The main distance peak corresponds with that one measured in methanol solution with only a slight deviation to longer distances (~+0.2 nm) for the samples β-TOPP[1-14] and β-TOPP[1-17]. In general, the distance distributions are broader in lipid bilayer than in methanol solution because the peptide-lipids interactions can increase the label's conformational space. According to the experimental results, this effect is more pronounced in β-TOPP[1-16] and β-TOPP[1-17] where labelling positions are closer to the lipid head group tail interface when compared to the other two β-TOPP peptides. β-TOPP[1-14] sample shows also some small additional peaks which however do not compromise the analysis of the experimental data. In order to exclude a possible aggregation of the peptide at the membrane, a series of PELDOR/DEER experiments with lower spin/phospholipid ratio from 1/3000 up to 1/12000 were performed by ANNAMARIE KEHL and Dr. KARIN HALBMAIR at the Max Planck Institute for Biophysical Chemistry. The dilution of peptide should prevent a possible aggregation; nevertheless, the extra-peaks does not vanish suggesting that they might be associated with little structural perturbations for that defined label position.

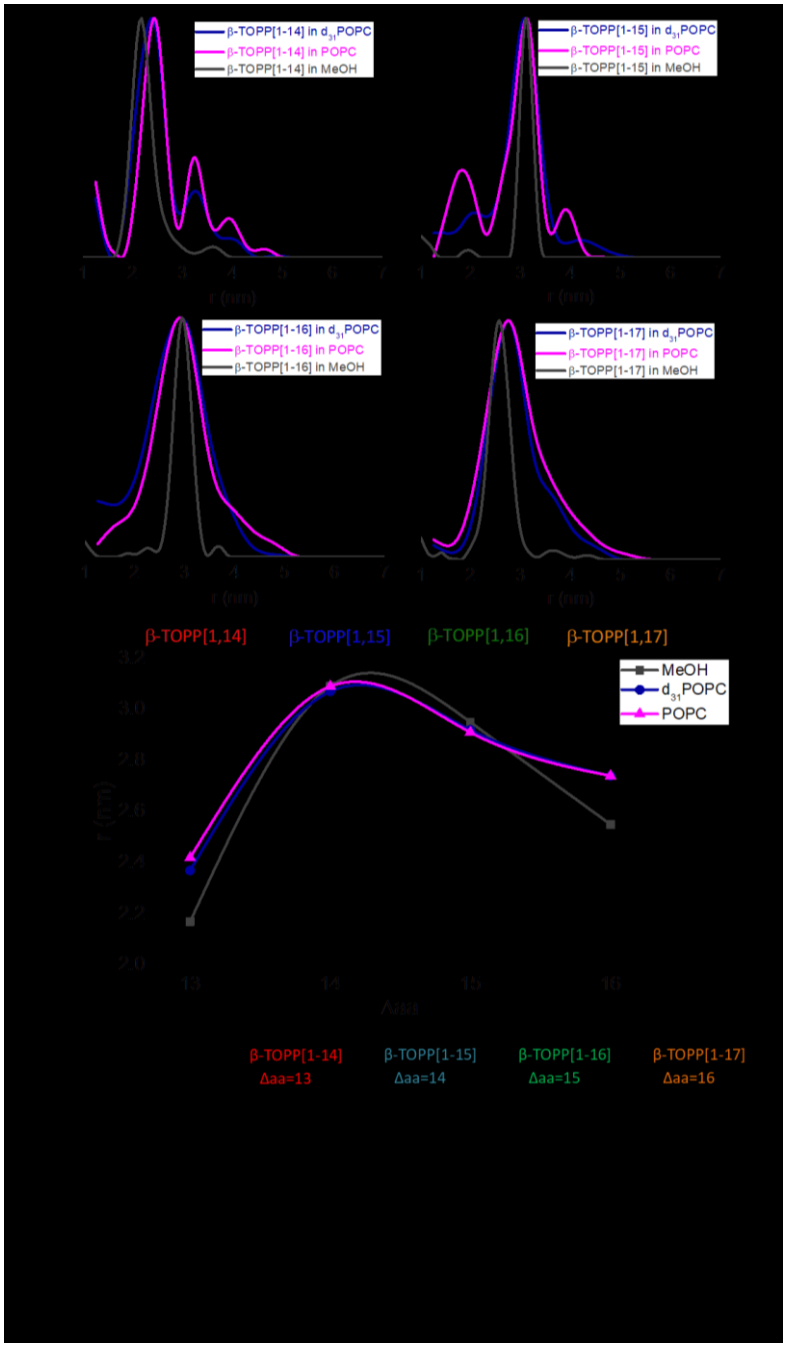

Figure 11.10. On the upper part, the extracted distance distributions of β^3-TOPP peptides in MLVs of d_{31}POPC (blue) and POPC (magenta) together with the experimental PELDOR/DEER distance in methanol solution (grey) for comparison are shown. On the bottom part all experimental PELDOR/DEER data are summarized in a table and a. graphical representation of the distance trend as a function of the amino acid separation is reported.

Looking at the graphical illustration of the experimental distances of figure 11.10, a helical secondary structure is confirmed also in MLVs with a very similar periodicity of the helix in methanol and in lipid environment. These results strongly indicate that β^3-peptides fold similarly in solution and in a phospholipid bilayer and lipid-peptide interactions do not influence β^3-peptides' secondary structure.

The distance distributions of β^3-TOPP peptide samples extracted in lipid bilayer were validated employing the statistical validation tool of DeerAnalysis 2013 program.[39] For all PELDOR/DEER traces the background starting point was varied in a range from 240 ns up to 1000 ns, performing 11 trials. Additionally, the influence of the noise on the distance distributions was estimated carrying out other 10 trials where the noise was increased of a factor of 2 by adding artificially random points to the experimental data. Combining all data sets achieved from each attempt for both parameters under investigation, in total 110 trials were carried out followed by pruning of the trial results with a prune factor of 1.15. This procedure excludes the data sets which exceed more than 15% the lowest root mean square deviation (rmsd). The resulting distance distributions, shown in figure 11.11, present a 2σ confidential interval; the grey bars correspond to an error of ±2 times the rmsd for each point of the distance distribution.

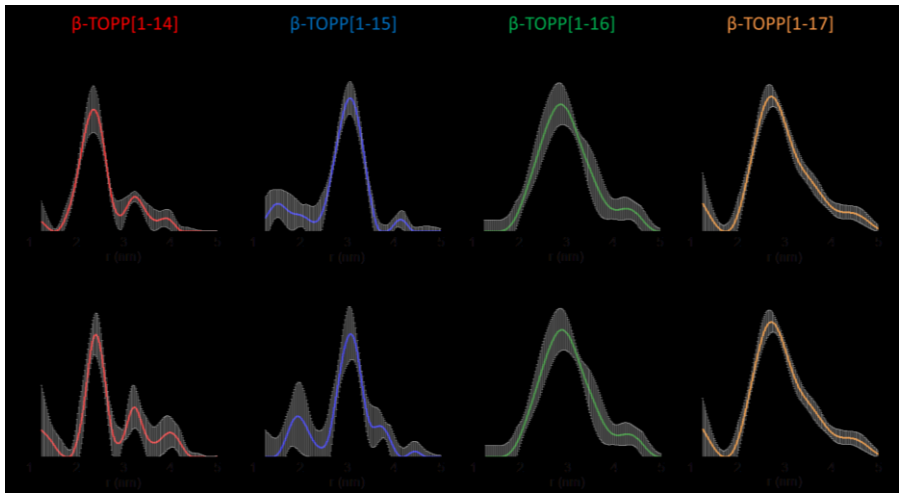

Figure 11.11 Validation of distance distributions extracted from the experimental PELDOR/DEER traces of β^3-TOPP peptide samples recorded in MLVs of d_{31}POPC and POPC.

These outcomes confirm the existence of more than one distance for the sample β-TOPP[1-14] whose origin is still unclear. Moreover, β-TOPP[1-15] presents a bit more complicated distance distribution pattern in POPC than in d_{31}POPC but with a main peak always centred around 3.1 nm. In any case, the presence of additional distance peaks do not interfere with the overall interpretation of results.

11.4 Structural molecular models of β^3-TOPP peptide samples

Simplified β^3-TOPP peptide models of the 3_{14}-helix secondary structure were created by Dr. JANINE WEGNER[198] to make a comparison with the experimental data. The models are based on three different sets of torsion angles of β^3-peptide backbones published in the literature.[203–205] The presence of an additional methylene group in β-amino acids implies that four torsion angles, shown in figure 11.11, have to be considered when the dynamics of a β-peptide sequence has to be investigated.

The first structural model, named 3_{14}-QM, comes from a quantum mechanics optimization of a β^3-peptide backbone;[203] the second (3_{14}-crystal) derived from a β^3-peptide crystal structure; [204] the third (3_{14}-EO) is achieved through a computed ideal 3_{14}-helix with an energy-optimized backbone.[205] The values of the three sets of torsion angles are reported in figure 11.11.

Firstly, the peptide backbones were generated according with the published data, dismissing valine and lysine side-chains for simplification of the modelling. The molecular editor Avogadro was employed.[213] Afterwards, planar TOPP spin labels were DFT optimized. Then, the four spin labelled β^3-peptide models were obtained keeping fixed the backbone and nitroxide geometries and adjusting their mutual orientations around the connecting bond. A more reasonably adjusted orientation of the residues was achieved by applying the MERCK molecular force field (MMFF94).[214]

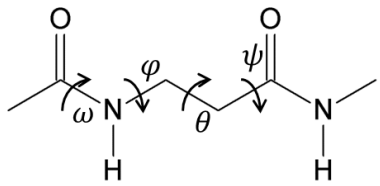

3_{14}-helix	ψ	θ	φ	ω
3_{14}-QM	139.9°	-60°	134.3°	-180°
3_{14}-crystal	132.3°	-54.2°	135.1°	-180°
3_{14}-EO	139.3°	-55°	123.4°	-180°

Figure 11.12. The table shows three sets of backbone torsion angles for a 3_{14}-helix secondary structure. These values were employed to create structural models for the four β^3-TOPP peptide samples characterized in this project.

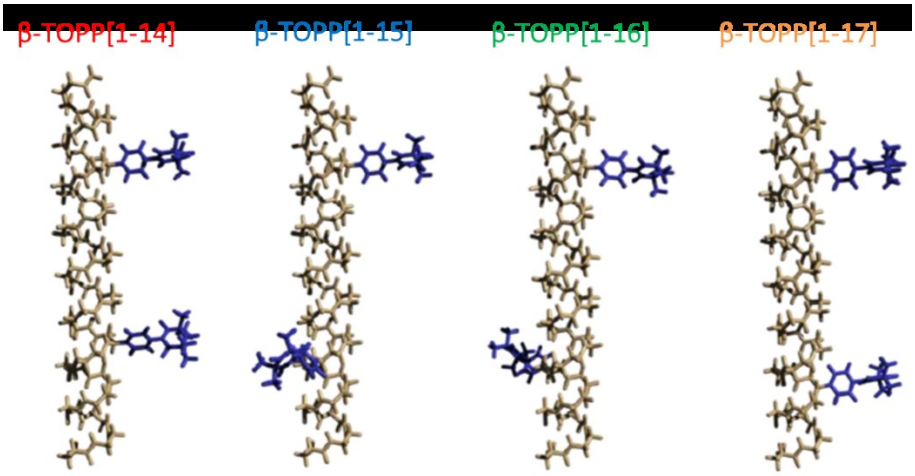

Figure 11.13. β^3-TOPP peptide 3_{14}-QM structural models. The figure is adapted from the PhD thesis of Dr. Janine Wegner.[198]

The structure of the four β^3-TOPP peptide samples achieved by the 3_{14}-QM model[203] is illustrated, as example, in figure 11.12.

Since the unpaired electron is delocalized between the oxygen and nitrogen atom of the nitroxide radical, the inter-spin distances between the first spin label (N_1-O_1·) and the second one (N_2-O_2·) were determined as average of the distances O_1–O_2, O_1–N_2, N_1–O_2 and N_1–N_2. All values and the average are given in the following tables (11.3. ÷ 11.6.).[198]

Table 11.3. Calculated inter-spin distances r [nm] from the three theoretical models for β-TOPP[1-14][198]

β-TOPP[1-14]	3_{14}-QM	3_{14}-crystal	3_{14}-EO
***r* (O_1–O_2)**	2.0525	2.3656	2.2133
***r* (O_1–N_2)**	2.0461	2.3336	2.1609
***r* (N_1–O_2)**	2.0753	2.3227	2.1912
***r* (N_1–N_2)**	2.0597	2.2861	2.1337
***r* (average)**	**2.0584**	**2.3270**	**2.1748**

Table 11.4. Calculated inter-spin distances r [nm] from the three theoretical models for β-TOPP[1-15].[198]

β-TOPP[1-15]	3_{14}-QM	3_{14}-crystal	3_{14}-EO
r **(O_1–O_2)**	2.9592	3.1896	3.0241
r **(O_1–N_2)**	2.8830	3.0809	2.9099
r **(N_1–O_2)**	2.8843	3.1000	2.9277
r **(N_1–N_2)**	2.8084	2.9943	2.8161
r **(average)**	**2.8837**	**3.0912**	**2.9195**

Table 11.5. Calculated inter-spin distances r [nm] from the three theoretical models for β-TOPP[1-16].[198]

β-TOPP[1-16]	3_{14}-QM	3_{14}-crystal	3_{14}-EO
r **(O_1–O_2)**	3.0211	2.3708	2.1480
r **(O_1–N_2)**	2.9533	2.3659	2.1420
r **(N_1–O_2)**	2.9345	2.3583	2.1241
r **(N_1–N_2)**	2.8688	2.3488	2.1129
r **(average)**	**2.9444**	**2.3600**	**2.1318**

Table 11.6. Calculated inter-spin distances r [nm] from the three theoretical models for β-TOPP[1-17].[198]

β-TOPP[1-17]	3_{14}-QM	3_{14}-crystal	3_{14}-EO
r **(O_1–O_2)**	2.5312	2.7378	2.4616
r **(O_1–N_2)**	2.5383	2.7051	2.4261
r **(N_1–O_2)**	2.5234	2.7245	2.4456
r **(N_1–N_2)**	2.5234	2.6884	2.4066
r **(average)**	**2.5291**	**2.7140**	**2.4350**

A graphical comparison between the calculated interspin distances and the experimental data obtained in methanol solution and in lipid bilayer is shown in figure 11.13.

The three structural theoretical models show three different periodicity of the helical secondary structures according with the three different β-peptide's backbone employed. Looking at the shape of the curves (figure 11.13) the experimental distances in methanol solution and in lipid bilayer are in close agreement with the interspin distances predicted by the structural model 3_{14}-QM depicted in yellow in figure 11.13. This observation strongly suggests a periodicity of the 14-helix consisting of 3.25 residues per turn.[203]

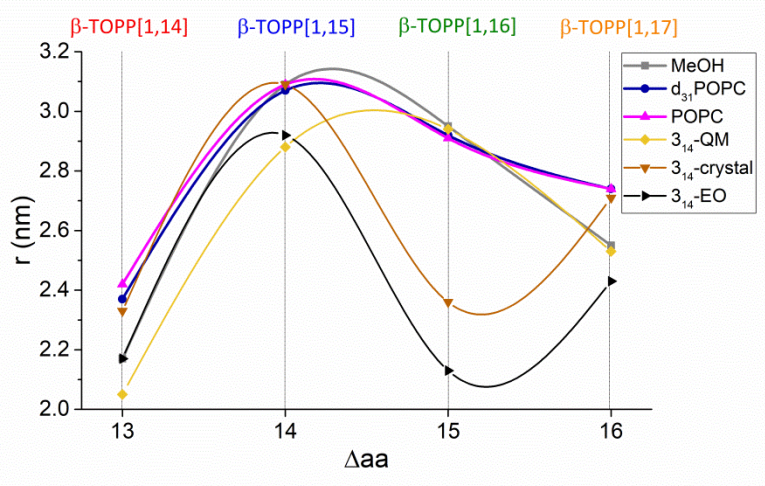

r [nm]	β-TOPP[1-14] *Δaa=13*	β-TOPP[1-15] *Δaa=14*	β-TOPP[1-16] *Δaa=15*	β-TOPP[1-17] *Δaa=16*
PELDOR MeOH	2.17 Δr = 0.24	3.09 Δr = 0.15	2.95 Δr = 0.21	2.55 Δr = 0.21
PELDOR d_{31}POPC	2.37 Δr = 0.39	3.07 Δr = 0.33	2.92 Δr = 0.64	2.74 Δr = 0.45
PELDOR POPC	2.42 Δr = 0.27	3.09 Δr = 0.29	2.91 Δr = 0.55	2.74 Δr = 0.45
3_{14}-QM	2.06	2.88	2.94	2.53
(3_{14}-crystal)	2.33	3.09	2.36	2.71
3_{14}-EO	2.17	2.92	2.13	2.43

Figure 11.14. Graphical comparison between the experimental PELDOR/DEER distances and the distances predicted by the three β^3-TOPP peptide models. All values are summarized in the table below.

The experimental distances in solution and in MLVs for the sample β-TOPP[1-16] fit perfectly with the theoretical one. The other samples present just a slight deviation to longer distances (~+0.2 nm). This might likely come from a too simplified structural model due to the disregard, during the construction of the models, of the solvent effects (for samples in methanol solution), and of lipid effects (for samples in MLVs).

Looking at the periodicity of the helix, these results seem to confirm the data coming from a previous NMR study on β^3-eicosapeptide in methanol solution performed by SEEBACH and co-workers.[199] This study reveals an offset of around 15° in the right-handed direction from the ideal 3_{14}-helix that yields an helical periodicity made up of 3.1. ÷ 3.4 amino acids per turn.[199] Taken together all these considerations it is possible to assume that β^3-peptide sequence designed by DIEDERICHSEN and co-workers (figure 10.3) and the four doubly labelled β^3-TOPP peptides employed in this project fold in solution forming a "3.2_{14}" helix. PELDOR/DEER experiments carried out in MLVs indicate that peptide-lipid interactions do not affect this secondary structure which is preserved in the lipid environment. These data are consistent with CD measurements on labelled and non-labelled β-peptide sequences recorded in both environments by Dr. JANINE WEGNER.[198]

11.5 Conclusions and Perspectives

The experimental results have demonstrated that EPR spectroscopy in combination with SDSL strategies is a powerful biophysical tool which allows to reveal biomolecular structural information on spin labelled biological systems in their natural environment. In particular, this study has demonstrated that the semi-rigid β^3-TOPP spin label incorporated into a β^3-peptide backbone enables to achieve reliable and narrow distance distributions in solution and in lipid bilayer at atomic resolution.

CW-EPR and 3-pulse ESEEM experiments on β^3-TOPP peptide samples have given some indications about the proper incorporation of peptides into MLVs. Moreover, PELDOR/DEER distance measurements have unveiled that the β^3-TOPP spin labelled peptide sequences investigated in this project fold in a "3.2_{14}-helix" in solution and in lipid bilayer with negligible influences of peptide-lipid interactions on the secondary structure.

These data strongly encourage the usage of TOPP spin label for the study of further transmembrane peptide systems by EPR spectroscopy.

12. Final conclusions

The experimental data shown in this thesis highlight the potential of EPR spectroscopy to unveil peculiar information on systems containing one or more paramagnetic centres. Both CW and pulsed EPR methods emerge as very powerful techniques to characterize a wide range of paramagnetic samples from small metal complexes to large macromolecular structures with high resolution. In fact, EPR is not limited by any size restrictions and it is sensitive only to the magnetic moment of the unpaired electron and its magnetic interactions with the close surrounding. The remaining parts of the system under investigation is EPR silent.

The critical steps that must be considered to perform an EPR measurement are associated with the sample preparation, in particular when a spin labelled macromolecule is designed, and to the set-up of the experimental parameters that has to ensure an adequate signal to noise ratio to probe specific magnetic interactions.

In particular, the experimental temperature is a key parameter that must be properly set because it influences the relaxation times of the electron spin and the resolution of EPR signal. Moreover, moving from fluid solution to frozen solution, where the electron magnetic momenta are not free to move, EPR spectroscopy enable to resolve g and hyperfine anisotropies revealing the "fingerprints" of the paramagnetic centres and the peculiar features of its close surrounding. Performing EPR experiments at high fields and high frequencies it is also possible to explore specific orientations of the unpaired electron.[14,59]

About the copper(II) complexes with arginate and glutamate ligands, investigated in the second part of the thesis, CW-EPR spectra recorded at room temperature and in frozen solution at X-band frequencies (9.5 GHz) clearly suggest that this complex species adopt a tetragonally elongated octahedral geometry. Furthermore, the EPR measurements unveil the existence in solution of an equilibrium between the *cis* and *trans* conformers for the same complex species, giving also some indications about the percentages of formation of each conformer. The modifications of the *cis/trans* ratio as a function of the temperature suggest how the electrostatic interactions among the charged side chains of aminoacidate ligands might favour the formation of one conformer over the other.

CW-EPR experiments performed always at X-band frequencies (9.5 GHz) on ternary copper(II) complexes with 1,10-phenantroline and some

aminoacidate ligands, known as *cassiopeinas*, prove that all these systems present the same stereochemistry observed for the copper(II) complexes with arginate and glutamate ligands differently from the geometry adopted at solid-state and determined by X-ray crystallography.[131,140–142] Only the ternary complexes with 1,10-phenantroline and histidine show a peculiar behaviour. Histidine can coordinate Cu(II) ions with a glycine-like, at acidic pH values, or with a histamine-like mode at pH values around the neutrality, involving the deprotonated nitrogen atom of the imidazole side chains in the coordination sphere.[164] The anisotropic magnetic parameters extracted at pH around 7 and 150 K for this complex highlight that the temperature might influence the formation of the [Cu(phen)(His)] complex, leading to think that this formation process is endothermic. Actually, at 150 K it is possible to see the spectral features of the [Cu(phen)(HisH)] complex together with other copper species coming from a dissociation of [Cu(phen)(His)]. In any case, the geometrical characteristics of [Cu(phen)(His)] complex differ from those of [Cu(phen)(HisH)] because the former adopts probably a square-based pyramidal geometry.

All the voltammetric measurements, performed on these copper(II) complexes, support these conclusions.

The spectroscopic and voltammetric data shown in the second part of this thesis allow to extract also some useful bioinorganic implications about these copper(II) complexes. In particular, in the case of complexes with arginate and glutamate it is possible to determine which conformer easier form in physiological condition in the brain giving the basis to explore further biochemical properties of this copper(II) species in this compartment.

About the *cassiopeinas*, the highly negative formal redox potentials extracted by voltammetric measurements give some indications about the redox properties of the metal centre excluding the hypothesis of an involvement of copper(II) redox reactions in the mechanism of action of this class of metal-based drugs.

CW and pulsed EPR measurements performed on a β-peptide sequence in solution and in lipid bilayer demonstrate the great potential of EPR spectroscopy, in combination with SDSL strategies, for structural characterization of peptides in both environments at atomic resolution. In particular, the semi-rigid nitroxide TOPP spin label, thanks to its restricted mobility, shows good spectroscopic features, which make it an excellent

probe to monitor peptide secondary structures and structural modifications due to the interactions with different environments. The spectroscopic data, in fact, clearly prove that the periodicity of the 14-helix secondary structure adopted by β-TOPP peptide is around 3.2 residues per turn either in methanol solution or in multilamellar vesicles of POPC with negligible influences associated with the peptide-lipid interactions.

Placing TOPP spin label in other positions of the peptide backbone it would be possible to detect if this "3.2" periodicity of the helix is maintained along the whole sequence or if there are some deviations from this value.

This β-TOPP peptide sequence represents a promising tool that can be used as a model for further structural investigations of peptides in a lipid environment. Changing some experimental conditions, such as the peptide/lipid ratio, the peptide length or employing a phospholipid, which has a different hydrophobic thickness, it would be possible to perform a systematic EPR characterization of all adaption mechanisms of this system to the mismatch conditions.[206,207]

References

[1] K. M. Salikhov, in *Found. Mod. EPR*, World Scientific, **1998**, pp. 45–50.

[2] C. Altenbach, T. Marti, H. G. Khorana, W. L. Hubbell, *Science* **1990**, *248*, 1088–1092.

[3] J. E. Wertz, J. R. Bolton, *Electron Spin Resonance - Elementary Theory and Practical Applications*, Springer Netherlands, **1986**.

[4] M. Brustolon, E. Giammello, *Electron Paramagnetic Resonance - A Practitioner's Toolkit*, John Wiley And Sons Inc., Hoboken, New Jersey, **2009**.

[5] K. A. McLauchlan, *Magnetic Resonance*, Oxford University Press, Oxford, **1972**.

[6] O. Schiemann, T. F. Prisner, *Q. Rev. Biophys.* **2007**, *40*, 1–53.

[7] W. B. Mims, K. Nassau, J. D. McGee, *Phys. Rev.* **1961**, *123*, 2059–2069.

[8] L. Kevan, M. K. Bowman, P. A. Narayana, R. K. Boeckman, V. F. Yudanov, Y. D. Tsvetkov, *J. Chem. Phys.* **1975**, *63*, 409–416.

[9] E. Reijerse, F. Lendzian, R. Isaacson, W. Lubitz, *J. Magn. Reson.* **2012**, *214*, 237–243.

[10] M. Bennati, T. F. Prisner, *Reports Prog. Phys.* **2005**, *68*, 411–448.

[11] G. Valora, R. P. Bonomo, G. Tabbì, *Inorg. Chim. Acta* **2016**, *453*, 62–68.

[12] S. Blanchard, G. Blondin, E. Rivière, M. Nierlich, J. J. Girerd, *Inorg. Chem.* **2003**, *42*, 4568–78.

[13] A. L. Barra, L. C. Brljnel, J. B. Robert, *Chem. Phys. Lett.* **1990**, *165*, 107–109.

[14] I. Tkach, S. Pornsuwan, C. Höbartner, F. Wachowius, S. T. Sigurdsson, T. Y. Baranova, U. Diederichsen, G. Sicoli, M. Bennati, *Phys. Chem. Chem. Phys.* **2013**, *15*, 3433–3437.

[15] W. Hagen, *Biomolecular EPR Spectroscopy*, CRC Press, Boca Raton, **2009**.

[16] G. R. Eaton, S. S. Eaton, D. P. Barr, R. T. Weber, *Quantitative EPR*, Springer-Verlag Wien, **2010**.

[17] G. Jeschke, "CW and Pulse EPR," can be found under http://www.epr.ethz.ch/education/basic-concepts-of-epr.

[18] P. E. Spindler, P. Schöps, A. M. Bowen, B. Endeward, T. F. Prisner, *eMagRes* **2016**, *5*, 1477–1492.

[19] E. L. Hahn, *Phys. Rev.* **1950**, *80*, 580–594.

[20] H. Y. Carr, E. M. Purcell, *Phys. Rev.* **1954**, *94*, 630–638.

[21] G. Jeschke, Y. Polyhach, *Phys. Chem. Chem. Phys.* **2007**, *9*, 1895–1910.

[22] G. W. Reginsson, O. Schiemann, *Biochem. J.* **2011**, *434*, 353–363.

[23] G. Jeschke, *Annu. Rev. Phys. Chem.* **2012**, *63*, 419–446.

[24] A. D. Milov, A. B. Ponomarev, Y. D. Tsvetkov, *Chem. Phys. Lett.* **1984**, *110*, 67–72.

[25] R. E. Martin, M. Pannier, F. Diederich, V. Gramlich, M. Hubrich, H. W. Spiess, *Angew. Chemie Int. Ed.* **1998**, *37*, 2833–2837.

[26] M. Pannier, S. Veit, A. Godt, G. Jeschke, H. W. Spiess, *J. Magn. Reson.* **2000**, *142*, 331–340.

[27] P. P. Borbat, E. R. Georgieva, J. H. Freed, **2013**, *4*, 170–175.

[28] P. E. Spindler, I. Waclawska, B. Endeward, J. Plackmeyer, C. Ziegler, T. F. Prisner, *J. Phys. Chem. Lett.* **2015**, *6*, 4331–4335.

[29] E. J. Hustedt, A. H. Beth, in *Distance Meas. Biol. Syst. by EPR* (Eds.: L.J. Berliner, G.R. Eaton, S.S. Eaton), Springer US, Boston, MA, **2002**, pp. 155–184.

[30] J. E. Banham, C. M. Baker, S. Ceola, I. J. Day, G. H. Grant, E. J. J. Groenen, C. T. Rodgers, G. Jeschke, C. R. Timmel, *J. Magn. Reson.* **2008**, *191*, 202–218.

[31] M. Drescher, in *EPR Spectrosc. Appl. Chem. Biol.* (Eds.: M. Drescher, G. Jeschke), Springer Berlin Heidelberg, Berlin, Heidelberg, **2012**, pp. 91–119.

[32] G. Jeschke, M. Pannier, H. W. Spiess, in *Distance Meas. Biol. Syst. by EPR* (Eds.: L.J. Berliner, G.R. Eaton, S.S. Eaton), Springer US, Boston, MA, **2002**, pp. 493–512.

[33] S. S. Eaton, G. R. Eaton, in *Distance Meas. Biol. Syst. by EPR* (Eds.: L.J. Berliner, G.R. Eaton, S.S. Eaton), Springer US, Boston, MA, **2002**, pp. 29–154.

[34] K. Halbmair, J. Seikowski, I. Tkach, C. Höbartner, D. Sezer, M. Bennati, *Chem. Sci.* **2016**, *7*, 3172–3180.

[35] R. Ward, A. Bowman, E. Sozudogru, H. El-Mkami, T. Owen-Hughes, D. G. Norman, *J. Magn. Reson.* **2010**, *207*, 164–167.

[36] T. Schmidt, M. A. Wälti, J. L. Baber, E. J. Hustedt, G. M. Clore, *Angew. Chemie - Int. Ed.* **2016**, *55*, 15905–15909.

[37] I. M. S. de Vera, M. E. Blackburn, L. Galiano, G. E. Fanucci, *Curr.*

Protoc. Protein Sci. **2013**, 1–29.

[38] Y. D. Tsvetkov, Y. A. Grishin, *Instruments Exp. Tech.* **2009**, *52*, 615–636.

[39] G. Jeschke, V. Chechik, P. Ionita, A. Godt, H. Zimmermann, J. Banham, C. R. Timmel, D. Hilger, H. Jung, *Appl. Magn. Reson.* **2006**, *30*, 473–498.

[40] Y. W. Chiang, P. P. Borbat, J. H. Freed, *J. Magn. Reson.* **2005**, *172*, 279–295.

[41] W. B. Mims, *Phys. Rev. B* **1972**, *5*, 2409–2419.

[42] S. A. Dikanov, Y. D. Tsvetkov, *Electron Spin Echo Envelope Modulation (ESEEM) Spectroscopy*, Boca Raton, **1992**.

[43] L. G. Rowan, E. L. Hahn, W. B. Mims, *Phys. Rev.* **1965**, *137*, A61–A71.

[44] R. D. Britt, K. Sauer, M. P. Klein, D. B. Knaff, A. Kriauciunas, C. A. Yu, L. Yu, R. Malkin, *Biochemistry* **1991**, *30*, 1892–1901.

[45] H. S. Mchaourab, M. A. Lietzow, K. Hideg, W. L. Hubbell, *Biochemistry* **1996**, *2960*, 7692–7704.

[46] G. Jeschke, *Emerg. Top. Life Sci.* **2018**, *2*, 9–18.

[47] I. Krstic, B. Endeward, D. Margraf, A. Marko, T. F. Prisner, *Top Curr Chem* **2012**, *321*, 159–198.

[48] J. P. Klare, H. J. Steinhoff, *Photosynth. Res.* **2009**, *102*, 377–390.

[49] E. Bordignon, *eMagRes* **2017**, *6*, 235–254.

[50] M. R. Fleissner, E. M. Brustad, T. Kálai, C. Altenbach, D. Cascio, F. B. Peters, K. Hideg, S. Peuker, P. G. Schultz, W. L. Hubbell, *Proc. Natl. Acad. Sci.* **2009**, *106*, 21637–21642.

[51] J. L. Flippen-Anderson, C. George, G. Valle, E. Valent, A. Bianco, F. Formaggio, M. Crisma, C. Toniolo, *Int. J Pept. Protein Res* **1996**, *47*, 231–238.

[52] R. S. Keyes, A. M. Bobst, in *Biol. Magn. Reson. Vol. 14 Spin Labeling* (Ed.: L.J. Berliner), Springer US, Boston, MA, **2002**, pp. 283–338.

[53] S. A. Shelke, S. T. Sigurdsson, *European J. Org. Chem.* **2012**, 2291–2301.

[54] A. Martorana, G. Bellapadrona, A. Feintuch, E. Di Gregorio, S. Aime, D. Goldfarb, *J. Am. Chem. Soc.* **2014**, *136*, 13458–13465.

[55] Y. Yang, F. Yang, Y. J. Gong, J. L. Chen, D. Goldfarb, X. C. Su, *Angew. Chemie - Int. Ed.* **2017**, *56*, 2914–2918.

[56] M. J. Schmidt, J. Borbas, M. Drescher, D. Summerer, *J. Am. Chem. Soc.* **2014**, *136*, 1238–1241.

[57] A. A. Kuzhelev, R. K. Strizhakov, O. A. Krumkacheva, Y. F. Polienko, D. A. Morozov, G. Y. Shevelev, D. V. Pyshnyi, I. A. Kirilyuk, M. V. Fedin, E. G. Bagryanskaya, *J. Magn. Reson.* **2016**, *266*, 1–7.

[58] E. Matalon, T. Huber, G. Hagelueken, B. Graham, V. Frydman, A. Feintuch, G. Otting, D. Goldfarb, *Angew. Chemie - Int. Ed.* **2013**, *52*, 11831–11834.

[59] G. Prokopiou, M. D. Lee, A. Collauto, E. H. Abdelkader, T. Bahrenberg, A. Feintuch, M. Ramirez-Cohen, J. Clayton, J. D. Swarbrick, B. Graham, *Inorg. Chem.* **2018**, *57*, 5048–5059.

[60] T. F. Cunningham, M. D. Shannon, M. R. Putterman, R. J. Arachchige, I. Sengupta, M. Gao, C. P. Jaroniec, S. Saxena, *J. Phys. Chem. B* **2015**, *119*, 2839–2843.

[61] H. Y. V. Ching, F. C. Mascali, H. C. Bertrand, E. M. Bruch, P. Demay-Drouhard, R. M. Rasia, C. Policar, L. C. Tabares, S. Un, *J. Phys. Chem. Lett.* **2016**, *7*, 1072–1076.

[62] G. W. Reginsson, N. C. Kunjir, S. T. Sigurdsson, O. Schiemann, *Chem. - A Eur. J.* **2012**, *18*, 13580–13584.

[63] M. M. Haugland, J. E. Lovett, E. A. Anderson, *Chem Soc Rev* **2018**, *47*, 668–680.

[64] V. Meyer, M. A. Swanson, L. J. Clouston, P. J. Boratyński, R. A. Stein, H. S. McHaourab, A. Rajca, S. S. Eaton, G. R. Eaton, *Biophys. J.* **2015**, *108*, 1213–1219.

[65] A. J. Fielding, M. G. Concilio, G. Heaven, M. A. Hollas, *Molecules* **2014**, *19*, 16998–17025.

[66] Y. Polyhach, E. Bordignon, G. Jeschke, *Phys. Chem. Chem. Phys.* **2011**, *13*, 2356–2366.

[67] G. Hagelueken, R. Ward, J. H. Naismith, O. Schiemann, *Appl. Magn. Reson.* **2012**, *42*, 377–391.

[68] M. R. Fleissner, M. D. Bridges, E. K. Brooks, D. Cascio, T. Kalai, K. Hideg, W. L. Hubbell, *Proc. Natl. Acad. Sci.* **2011**, *108*, 16241–16246.

[69] I. D. Sahu, R. M. McCarrick, K. R. Troxel, R. Zhang, H. J. Smith, M. M. Dunagan, M. S. Swartz, P. V. Rajan, B. M. Kroncke, C. R. Sanders, *Biochemistry* **2013**, *52*, 6627–6632.

[70] M. Lorenzi, C. Puppo, R. Lebrun, S. Lignon, V. Roubaud, M. Martinho, E. Mileo, P. Tordo, S. R. A. Marque, B. Gontero, *Angew. Chemie - Int. Ed.* **2011**, *50*, 9108–9111.

[71] S. Schreier, J. C. Bozelli, N. Marín, R. F. F. Vieira, C. R. Nakaie, *Biophys. Rev.* **2012**, *4*, 45–66.

[72] E. F. Vicente, L. G. M. Basso, G. F. Cespedes, E. N. Lorenzón, M. S. Castro, M. J. S. Mendes-Giannini, A. J. Costa-Filho, E. M. Cilli, *PLoS One* **2013**, *8*, DOI 10.1371/journal.pone.0060818.

[73] M. H. Shabestari, M. Van Son, A. Moretto, M. Crisma, C. Toniolo, M. Huber, *Biopolym. - Pept. Sci. Sect.* **2014**, *102*, 244–251.

[74] K. Wright, M. Wakselman, J. P. Mazaleyrat, L. Franco, A. Toffoletti, F. Formaggio, C. Toniolo, *Chem. - A Eur. J.* **2010**, *16*, 11160–11166.

[75] M. Tominaga, S. R. Barbosa, E. F. Poletti, J. Zukerman-Schpector, R. Marchetto, S. Schreier, C. Paiva, C. R. Nakaie, *Chem. Pharm. Bull. (Tokyo).* **2001**, *49*, 1027–1029.

[76] S. Stoller, G. Sicoli, T. Y. Baranova, M. Bennati, U. Diederichsen, *Angew. Chemie - Int. Ed.* **2011**, *50*, 9743–9746.

[77] K. Halbmair, J. Wegner, U. Diederichsen, M. Bennati, *Biophys. J.* **2016**, *111*, 2345–2349.

[78] D. K. Yadav, P. J. Lukavsky, *Prog. Nucl. Magn. Reson. Spectrosc.* **2016**, *97*, 57–81.

[79] P. C. A. van der Wel, *Solid State Nucl. Magn. Reson.* **2017**, *88*, 1–14.

[80] E. L. Hesketh, K. Saunders, C. Fisher, J. Potze, J. Stanley, G. P. Lomonossoff, N. A. Ranson, *Nat. Commun.* **2018**, *9*, 1–10.

[81] A. W. P. Fitzpatrick, B. Falcon, S. He, A. G. Murzin, G. Murshudov, H. J. Garringer, R. A. Crowther, B. Ghetti, M. Goedert, S. H. W. Scheres, *Nature* **2017**, *547*, 185–190.

[82] D. Quentin, S. Raunser, *J. Mol. Med.* **2018**, *96*, 483–493.

[83] W. Kühlbrandt, *Elife* **2014**, *3*, e03665.

[84] D. Klose, J. P. Klare, D. Grohmann, C. W. M. Kay, F. Werner, H.-J. Steinhoff, *PLoS One* **2012**, *7*, e39492.

[85] K. a Merchant, R. B. Best, J. M. Louis, I. V Gopich, W. a Eaton, *Proc. Natl. Acad. Sci. U. S. A.* **2007**, *104*, 1528–1533.

[86] C. Kim, J. Y. Kim, S. H. Kim, B. Il Lee, N. K. Lee, *Chem. Commun.* **2012**, *48*, 1138–1140.

[87] M. Bood, S. Sarangamath, M. S. Wranne, M. Grøtli, L. M. Wilhelmsson, *J. Org. Chem.* **2018**, *14*, 114–129.

[88] T. Lavergne, R. Lamichhane, D. A. Malyshev, Z. Li, L. Li, E. Sperling, J. R. Williamson, D. P. Millar, F. E. Romesberg, *ACS Chem. Biol.* **2016**, *11*, 1347–1353.

[89] A. M. van Oijen, *Curr. Opin. Biotechnol.* **2011**, *22*, 75–80.

[90] F. Scarpelli, M. Drescher, T. Rutters-Meijneke, A. Holt, D. T. S. Rijkers, J. A. Killian, M. Huber, *J. Phys. Chem. B* **2009**, *113*, 12257–12264.

[91] R. P. Bonomo, G. Impellizzeri, G. Pappalardo, E. Rizzarelli, G. Tabbì, *Chem. - A Eur. J.* **2000**, *6*, 4195–4202.

[92] N. Kisseleva, S. Kraut, *HFSP J.* **2007**, *1*, 127–136.

[93] B. A. Goodman, J. B. Raynor, in *Adv. Inorg. Chem. Radiochem.*, **1970**, pp. 135–362.

[94] C. E. Housecraft, A. G. Sharpe, *Inorganic Chemistry*, Pearson, Essex, **2012**.

[95] M. V. Veidis, G. H. Schreiber, T. E. Gough, G. J. Palenik, *J. Am. Chem. Soc.* **1969**, DOI 10.1021/ja01035a051.

[96] R. Gupta, T. Taguchi, A. S. Borovik, M. P. Hendrich, *Inorg. Chem.* **2013**, *52*, 12568–12575.

[97] R. P. Bonomo, F. Riggi, *Lett. Nuovo Cim.* **1981**, *30*, 304–310.

[98] R. P. Bonomo, F. Riggi, *Chem. Phys. Lett.* **1982**, *93*, 99–102.

[99] H. Haraguchi, *J. Anal. At. Spectrom.* **2004**, *19*, 5–14.

[100] J. J. R. Fraústo da Silva, R. J. P. Williams, *J. Chem. Educ.* **2004**, *81*, 738–749.

[101] D. La Mendola, C. Giacomelli, E. Rizzarelli, *Curr. Top. Med. Chem.* **2016**, *16*, 3103–3130.

[102] S. K. Chhetri, R. J. Mills, S. Shaunak, H. C. A. Emsley, *BMJ* **2014**, *348*, g3691.

[103] L. Kent Wood, D. J. Thiele, *J. Biol. Chem.* **2009**, *284*, 404–413.

[104] S. Soma, A. J. Latimer, H. Chun, A. C. Vicary, S. A. Timbalia, A. Boulet, J. J. Rahn, S. S. L. Chan, S. C. Leary, B.-E. Kim, et al., *Proc. Natl. Acad. Sci.* **2018**, *115*, 8161–8166.

[105] C. Manzl, J. Enrich, H. Ebner, R. Dallinger, G. Krumschnabel, *Toxicology* **2004**, *196*, 57–64.

[106] P. F. Predki, B. Sarkar, *J. Biol. Chem.* **1992**, *267*, 5842–5846.

[107] J. R. Prohaska, *Am. J. Clin. Nutr.* **2008**, *88*, 826S–829S.

[108] C. R. Ferreira, W. A. Gah, *Metab. Dis. Found. Clin. Manag. Genet. Pathol.* **2017**, *2*, 465–498.

[109] S. A. Zlatic, A. Vrailas-Mortimer, A. Gokhale, L. J. Carey, E. Scott, R. Burch, M. M. McCall, S. Rudin-Rush, J. B. Davis, C. Hartwig, et al., *Cell Syst.* **2018**, DOI 10.1016/j.cels.2018.01.008.

[110] M. T. Lorincz, in *Handb. Clin. Neurol.* (Eds.: D.H. Geschwind, H.L.

Paulson, C. Klein), Elsevier B.V., **2018**, pp. 279–292.

[111] I. F. Scheiber, J. F. B. Mercer, R. Dringen, *Prog. Neurobiol.* **2014**, *116*, 33–57.

[112] L. Wang, J. S. Becker, Q. Wu, M. F. Oliveira, F. A. Bozza, A. L. Schwager, M. Hoffman, K. A. Morton, *Metallomics* **2010**, *2*, 348–353.

[113] A. Cruces-Sande, A. I. Rodríguez-Pérez, P. Herbello-Hermelo, P. Bermejo-Barrera, E. Méndez-Álvarez, J. L. Labandeira-García, R. Soto-Otero, *Mol. Neurobiol.* **2018**, DOI 10.1007/s12035-018-1274-7.

[114] R. Sirabella, V. Valsecchi, S. Anzilotti, O. Cuomo, A. Vinciguerra, P. Cepparulo, P. Brancaccio, N. Guida, N. Blondeau, L. M. T. Canzoniero, et al., **2018**, *12*, 1–14.

[115] L. Rossi, M. Arciello, C. Capo, G. Rotilio, *Ital J Biochem* **2006**, *55*, 212–221.

[116] N. Vassallo, J. Herms, *J. Neurochem.* **2003**, *86*, 538–544.

[117] V. Desai, S. G. Kaler, **2018**, *88*, 855–858.

[118] S. R. Platt, *Vet. J.* **2007**, *173*, 278–286.

[119] P. Liu, M. S. Fleete, Y. Jing, N. D. Collie, M. A. Curtis, H. J. Waldvogel, R. L. M. Faull, W. C. Abraham, H. Zhang, *Neurobiol. Aging* **2014**, *35*, 1992–2003.

[120] M. J. Kan, J. E. Lee, J. G. Wilson, A. L. Everhart, C. M. Brown, A. N. Hoofnagle, M. Jansen, M. P. Vitek, M. D. Gunn, C. A. Colton, *J. Neurosci.* **2015**, *35*, 5969–5982.

[121] Y. Shimazaki, T. Yajima, O. Yamauchi, *J. Inorg. Biochem.* **2015**, *148*, 105–115.

[122] L. D. Pettit, R. J. W. Hefford, *Met. Ions. Biol. Syst.* **1979**, *9*, 173–212.

[123] O. Yamauchi, A. Odani, *J Am Chem Soc* **1985**, *107*, 5938–5945.

[124] O. Yamauchi, A. Odani, M. Takani, *Dalt. Trans.* **2002**, 3411–3421.

[125] S. Ramakrishnan, V. Rajendiran, M. Palaniandavar, V. S. Periasamy, B. S. Srinag, H. Krishnamurthy, M. A. Akbarsha, *Inorg. Chem.* **2009**, *48*, 1309–1322.

[126] S. Rajalakshmi, T. Weyhermüller, A. J. Freddy, H. R. Vasanthi, B. U. Nair, *Eur. J. Med. Chem.* **2011**, *46*, 608–617.

[127] A. Hordyjewska, Ł. Popiołek, J. Kocot, *BioMetals* **2014**, *27*, 611–621.

[128] M. Ahmad, S. Suhaimi, T. Chu, N. A. Aziz, K. M. Kornain, D. S. Samiulla, K. Lo, C. Ng, A. Soo-, *PLoS One* **2018**, *13*, e01912195.

[129] X. Le, S. Liao, X. Liu, X. Feng, *J. Coord. Chem.* **2006**, *59*, 985–995.

[130] B. Annaraj, C. Balakrishnan, M. A. Neelakantan, *J. Photochem. Photobiol. B Biol.* **2016**, *160*, 278–291.

[131] X. Le, X. Zhou, C. Huang, X. Feng, *J. Coord. Chem.* **2003**, *56*, 861–867.

[132] A. K. Patra, S. Dhar, M. Nethaji, A. R. Chakravarty, *Chem. Commun.* **2003**, 1562–1563.

[133] T. Pivetta, M. D. Cannas, F. Demartin, C. Castellano, S. Vascellari, G. Verani, F. Isaia, *J. Inorg. Biochem.* **2011**, *105*, 329–338.

[134] T. Pivetta, F. Trudu, E. Valletta, F. Isaia, C. Castellano, F. Demartin, R. Tuveri, S. Vascellari, A. Pani, *J. Inorg. Biochem.* **2014**, *141*, 103–113.

[135] M. Wehbe, A. W. Y. Leung, M. J. Abrams, C. Orvig, M. B. Bally, *Dalt. Trans.* **2017**, *46*, 10758–10773.

[136] J. Espinal-Enríquez, E. Hernández-Lemus, C. Mejía, L. Ruiz-Azuara, *Front. Physiol.* **2016**, *6*, 1–13.

[137] J. Serment-Guerrero, M. E. Bravo-Gomez, E. Lara-Rivera, L. Ruiz-Azuara, *J. Inorg. Biochem.* **2017**, *166*, 68–75.

[138] A. G. Gutiérrez, A. Vázquez-Aguirre, J. C. García-Ramos, M. Flores-Alamo, E. Hernández-Lemus, L. Ruiz-Azuara, C. Mejía, *J. Inorg. Biochem.* **2013**, *126*, 17–25.

[139] I. Correia, S. Roy, C. P. Matos, S. Borovic, N. Butenko, I. Cavaco, F. Marques, J. Lorenzo, A. Rodríguez, V. Moreno, *J. Inorg. Biochem.* **2015**, *147*, 134–146.

[140] S. Zhang, J. Zhou, *J. Coord. Chem.* **2008**, *61*, 2488–2498.

[141] S. R. Liao, X. Y. Le, X. L. Feng, *J. Coord. Chem.* **2008**, *61*, 847–856.

[142] T. Hirohama, Y. Kuranuki, E. Ebina, T. Sugizaki, H. Arii, M. Chikira, P. T. Selvi, M. Palaniandavar, *J. Inorg. Biochem.* **2005**, *99*, 1205–1219.

[143] P. Jaividhya, R. Dhivya, M. A. Akbarsha, M. Palaniandavar, *J. Inorg. Biochem.* **2012**, *114*, 94–105.

[144] G. Valora, G. Munzi, R. P. Bonomo, *J. Inorg. Biochem.* **2018**, DOI https://doi.org/10.1016/j.jinorgbio.2018.10.012.

[145] T. Lund, J. Vanngard, *Chem Phys* **1965**, *42*, 2979–2980.

[146] J. R. Pilbrow, M. E. Winfield, *Mol. Phys. An Int. J. Interface Between Chem. Phys.* **1973**, *25*, 1073–1092.

[147] A. E. Kaifer, A. J. Bard, *J. Phys. Chem.* **1985**, *80*, 4876–4880.

[148] N. Ohata, H. Masuda, O. Yamauchi, *Inorg. Chim. Acta* **2000**, *300–302*, 749–761.

[149] L. Borer, D. Gallagher, J. Ready, *ChemBio News* **2005**, *15*, 40.

[150] M. S. Bukharov, V. G. Shtyrlin, A. S. Mukhtarov, G. V. Mamin, S. Stapf, C. Mattea, A. A. Krutikov, A. N. Il'In, N. Y. Serov, *Phys. Chem. Chem. Phys.* **2014**, *16*, 9411–9421.

[151] R. P. Bonomo, F. Riggi, A. J. Di Bilio, *Inorg. Chem.* **1988**, *27*, 2510–2512.

[152] L. Alderighi, P. Gans, A. Ienco, D. Peters, A. Sabatini, A. Vacca, *Coord. Chem. Rev.* **1999**, *184*, 311–318.

[153] T. Sakurai, O. Yamauchi, A. Nakahara, *Bull. Chem. Soc. Japan* **1978**, *51*, 3203–3208.

[154] B. A. Goodman, D. B. McPhail, H. K. J. Powell, *Dalt. Trans.* **1981**, 822–827.

[155] B. J. Hathaway, D. E. Billing, *Coord. Chem. Rev.* **1970**, *5*, 143–207.

[156] P. Pary, L. N. Bengoa, W. A. Egli, *J. Electrochem. Soc.* **2015**, *162*, D275–D282.

[157] G. Tabbì, A. Giuffrida, R. P. Bonomo, *J. Inorg. Biochem.* **2013**, *128*, 137–145.

[158] V. K. Patel, P. K. Bhattacharya, *Inorg. Chim. Acta* **1984**, *92*, 199–201.

[159] N. Türkel, C. Sahin, *Chem. Pharm. Bull. (Tokyo).* **2009**, *57*, 694–699.

[160] D. İnci, R. Aydin, *J. Solution Chem.* **2014**, *43*, 711–726.

[161] L. H. Abdel-Rahman, L. P. Battaglia, *Polyhedron* **1996**, *15*, 327–334.

[162] S. Bandyopadhyay, G. N. MukherjeeM., G. B. Drew, *Inorg. Chim. Acta* **2006**, *359*, 3243–3251.

[163] A. A. Shoukry, *J. Solution Chem.* **2011**, *40*, 1796–1818.

[164] L. Gala, M. Lawson, K. Jomova, L. Zelenicky, A. Congradyova, M. Mazur, M. Valko, *Molecules* **2014**, *19*, 980–991.

[165] H. Masuda, T. Sugimori, A. Odani, O. Yamauchi, *Inorg. Chim. Acta* **1991**, *180*, 73–79.

[166] M. Chikira, Y. Tomizawa, D. Fukita, T. Sugizaki, N. Sugawara, T. Yamazaki, A. Sasano, H. Shindo, M. Palaniandavar, W. E. Antholine, *J. Inorg. Biochem.* **2002**, *89*, 163–173.

[167] M. A. Zoroddu, S. Zanetti, R. Pogni, R. Basosi, *J. Inorg. Biochem.* **1996**, *63*, 291–300.

[168] P. Manikandan, B. Epel, D. Goldfarb, *Inorg. Chem.* **2001**, *40*, 781–787.

[169] R. Grommen, P. Manikandan, Y. Gao, T. Shane, J. J. Shane, R. A. Schoonheydt, B. M. Weckhuysen, D. Goldfarb, *J. Am. Chem. Soc.* **2000**, *122*, 11488–11496.

[170] D. Baute, D. Arieli, F. Neese, H. Zimmermann, B. M. Weckhuysen, D. Goldfarb, *J. Am. Chem. Soc.* **2004**, *126*, 11733–11745.

[171] L. H. Abdel-Rahman, P. L. Battaglia, P. Sgarabotto, M. R. Mahmoud, *J. Chem. Crystallogr.* **1994**, *24*, 567–571.

[172] T. Weiser, M. Wienrich, *Brain Res* **1996**, *742*, 211–218.

[173] E. D. Gaier, R. E. Mains, *J. Neurosci. Res* **2013**, *91*, 2–19.

[174] C. Sgarlata, G. Arena, R. P. Bonomo, A. Giuffrida, G. Tabbì, *J. Inorg. Biochem.* **2018**, *180*, 89–100.

[175] I. Moraes, G. Evans, J. Sanchez-Weatherby, S. Newstead, P. D. S. Stewart, *Biochim. Biophys. Acta* **2014**, *1838*, 78–87.

[176] J. Birch, D. Axford, J. Foadi, A. Meyer, A. Eckhardt, Y. Thielmann, I. Moraes, *Methods* **2018**, DOI 10.1016/j.ymeth.2018.05.014.

[177] S. J. Opella, F. M. Marassi, *Arch. Biochem. Biophys.* **2017**, *628*, 92–101.

[178] E. Bordignon, S. Bleicken, *Biochim. Biophys. Acta - Biomembr.* **2018**, *1860*, 841–853.

[179] N. Thonghin, V. Kargas, J. Clews, R. C. Ford, *Methods* **2018**, DOI 10.1016/j.ymeth.2018.04.018.

[180] I. D. Sahu, G. A. Lorigan, *Biomed Res. Int.* **2018**, *2018*, DOI 10.1155/2018/3248289.

[181] E. Bordignon, H.-J. Steinhoff, in *ESR Spectrosc. Membr. Biophys.*, Springer US, Boston, MA, **2007**, pp. 129–164.

[182] V. Corradi, E. Mendez-Villuendas, H. I. Ingólfsson, R. X. Gu, I. Siuda, M. N. Melo, A. Moussatova, L. J. Degagné, B. I. Sejdiu, G. Singh, *ACS Cent. Sci.* **2018**, *4*, 709–717.

[183] A. Holt, J. A. Killian, *Eur. Biophys. J.* **2010**, *39*, 609–621.

[184] J. A. Killian, T. K. Nyholm, *Curr. Opin. Struct. Biol.* **2006**, *16*, 473–479.

[185] R. P. Cheng, S. H. Gellman, W. F. DeGrado, *Chem. Rev.* **2001**, *101*, 3219–3232.

[186] U. Koert, *Angew Chem Int Ed. Engl* **1997**, *36*, 1836–1837.

[187] D. Seebach, J. L. Matthews, *Chem. Commun.* **1997**, *1*, 2015–2022.

[188] D. J. Hill, M. J. Mio, R. B. Prince, T. S. Hughes, J. S. Moore, *Chem. Rev.* **2001**, *101*, 3893–4011.

[189] E. Juaristi, V. A. Soloshonok, *Enantioselective Synthesis of β-Amino Acids*, John Wiley And Sons Inc., Hoboken, New Jersey, **2005**.

[190] D. Seebach, A. K. Beck, D. J. Bierbaum, *Chem. Biodivers.* **2004**, *1*, 1111–1239.

[191] D. F. Hook, P. Bindschädler, Y. R. Mahajan, R. Šebesta, P. Kast, D. Seebach, *Chem. Biodivers.* **2005**, *2*, 591–632.

[192] M. P. Del Borgo, K. Kulkarni, M. A. Tonta, J. L. Ratcliffe, R. Seoudi, A. I. Mechler, H. C. Parkington, M. Aguilar, M. P. Del Borgo, K. Kulkarni, et al., *APL Bioeng.* **2018**, *2*, DOI 10.1063/1.5020105.

[193] E. A. Porter, B. Weisblum, S. H. Gellman, *J. Am. Chem. Soc.* **2002**, *124*, 7324–7330.

[194] M. Werder, H. Hauser, S. Abele, D. Seebach, *Helv. Chim. Acta* **1999**, *82*, 1559–1571.

[195] P. I. Arvidsson, M. Rueping, D. Seebach, *Chem. Commun.* **2001**, *5*, 649–650.

[196] D. H. Appella, L. A. Christianson, I. L. Karle, D. R. Powell, S. H. Gellman, *J. Am. Chem. Soc.* **1999**, *121*, 6206–6212.

[197] D. Seebach, P. E. Ciceri, M. Overhand, J. Bernhard, D. Rigo, *Helv. Chim. Acta* **1996**, *79*, 2043–2066.

[198] J. Wegner, PhD thesis: "Synthesis of Rigid Spin Labels for the Investigation of Transmembrane Peptides by EPR Spectroscopy", University of Göttingen, **2018**.

[199] D. Seebach, R. I. Mathad, T. Kimmerlin, Y. R. Mahajan, P. Bindschädler, M. Rueping, B. Jaun, C. Hilty, T. Etezady-Esfarjani, *Helv. Chim. Acta* **2005**, *88*, 1969–1982.

[200] U. Rost, Y. Xu, T. Salditt, U. Diederichsen, *ChemPhysChem* **2016**, *17*, 1–11.

[201] J. A. Kritzer, J. Tirado-Rives, S. A. Hart, J. D. Lear, W. L. Jorgensen, A. Schepartz, *J. Am. Chem. Soc.* **2005**, *127*, 167–178.

[202] U. Rost, C. Steinem, U. Diederichsen, *Chem. Sci.* **2016**, *7*, 5900–5907.

[203] K. A. Bode, J. Applequist, *Macromolecules* **1997**, *30*, 2144–2150.

[204] D. S. Douglas, J. E. Petersson, J. X. Qiu, A. Schepartz, *J. Am. Chem. Soc.* **2007**, *129*, 1532–1537.

[205] S. J. Shandler, M. V. Shapovalov, R. L. Dunbrack, W. F. Degrado, *J. Am. Chem. Soc.* **2010**, *132*, 7312–7320.

[206] J. A. Killian, *Biochim. Biophys. Acta - Rev. Biomembr.* **1998**, *1376*, 401–416.

[207] F. Dumas, M. C. Lebrun, J. F. Tocanne, *FEBS Lett.* **1999**, *458*, 271–277.

[208] F. A. Nezil, M. Bloom, *Biophys. J.* **1992**, *61*, 1176–1183.

[209] N. Kučerka, M. P. Nieh, J. Katsaras, *Biochim. Biophys. Acta - Biomembr.* **2011**, *1808*, 2761–2771.

[210] N. Kučerka, S. Tristram-Nagle, J. F. Nagle, *J. Membr. Biol.* **2005**, *208*, 193–202.

[211] S. Stoll, A. Schweiger, *J. Magn. Reson.* **2006**, *178*, 42–55.

[212] S. C. Desensi, D. P. Rangel, A. H. Beth, T. P. Lybrand, E. J. Hustedt, *Biophys. J.* **2008**, *94*, 3798–3809.

[213] M. D. Hanwell, D. E. Curtis, D. C. Lonie, T. Vandermeerschd, E. Zurek, G. R. Hutchison, *J. Cheminform.* **2012**, *4*, 1–17.

[214] T. A. Halgren, *J. Comput. Chem.* **1996**, *17*, 490–497.